Characterisation and fabrication of zirconia and thoria based ceramics for nuclear applications

Von der Fakultät für Georessourcen und Materialtechnik der Rheinisch -Westfälischen Technischen Hochschule Aachen

zur Erlangung des akademischen Grades eines
Doktors der Ingenieurwissenschaften

genehmigte Dissertation

vorgelegt von **Master of science and chemical engineering (Ingénieur E.N.S.C.P.)**

Diane, Catherine BARRIER

aus *Poissy, Frankreich*

Characterisation and fabrication of zirconia and thoria based ceramics for nuclear applications

Diane Catherine Barrier

Index

Inhaltverzeichnis

Sommaire

1. Abstract

The reduction of the long term radiotoxicity of nuclear waste during disposal is the aim of the research called "Partitioning & Transmutation of minor actinides (MAs)", which also requires the development of inert ceramic support materials. Moreover, after separation, if the transmutation is not available, the actinides can be conditioned into stable dedicated solid matrices (Partitioning & Conditioning strategy). Yttrium-stabilized zirconia and thoria are discussed in the international nuclear community as candidates for the fixation of long-lived actinides as target material for transmutation and as stable materials for long-term final disposal.

The aims of the following work are twofold: determine the impact of the addition of actinides, simulated by cerium on the properties of the matrices and study the possibility of synthesising homogeneous ceramics using simple fabrication routes.

Within this framework, $(Zr,Y)O_{2-x}$ - CeO_2 and ThO_2 - CeO_2 powders with variable ceria contents (from 0 to 100 %) were synthesised by a co-precipitation method of nitrate solution. The influence of ceria concentration on the powder' properties, such as thermal behaviour and the evolution of material crystallisation during annealing, was investigated in detail by thermogravimetry (TG) coupled with differential scanning calorimetry (DSC) and X-ray diffraction (XRD). Both systems crystallise at high temperature in a stable solid solution, fcc, fluorite type structure and follow the Vegard's law for the complete range of ceria. For both systems a critical concentration of 20 mol % has been established. For ceria concentrations lower than 20 %, the properties of the system are mainly controlled by the matrix.

Pellets with different ceria concentrations were compacted from these powders by using different technological cycles. In order to obtain materials with reliable properties, the technological parameters of each chosen fabrication route, have been optimised. By employing mild wet methods (calcination at 600°C, wet-grinding in acetone and fractionation in acetone), $(Zr,Y,Ce)O_{2-x}$ pellets with densities of up to 0.97 TD can be obtained. In the case of the $(Th,Ce)O_2$ system, pressing by repressing from non-milled powder was selected as the fabrication route, allowing the fabrication of pellets with densities of up to 0.98 TD. In both cases, materials with homogeneous repartition of pores, well formed grains and boundaries and good mechanical properties were obtained.

Zusammenfassende Darstellung

Durch gezielte Abtrennung der langlebigen Aktiniden wie Plutonium und die sogenannten minoren Aktiniden (Americium, Curium, Neptunium) und anschließende Vernichtung durch Transmutation (P&T partitioning and transmutation strategy) ließe sich die Langzeitradiotoxizität des nuklearen Abfalls deutlich reduzieren. Die Konditionierung der langlebigen Aktiniden (P&C partitioning and conditioning strategy) wird auch als Alternative zur Transmutation in Betracht gezogen. Vor diesem Hintergrund war die Motivation dieser Arbeit nach einer dichten stabilen Wirtsmatrix zu suchen, die eine beträchtliche Menge an Aktiniden inkorporieren kann. Das Literaturstudium zeigt, das voll Yttrium-stabilisiertes Zirkonoxid und Thoriumoxid sehr vielversprechende Matrixes für beide Optionen (P&T und P&C) sind.

In der vorliegenden Dissertation wurden zwei Ziele verfolgt: erstens die Auswirkung der Ceriumzugabe (als Aktinidensimulat) auf die Eigenschaften der Matrizes zu studieren und zweitens Keramiken auf Zirkonoxid- und Thoriumoxidbasis mit stabilen und zuverlässigen Eigenschaften mit Hilfe einfacher Fabrikationsverfahren herzustellen.

In diesem Rahmen wurden $(Zr,Y)O_{2-x}$-CeO_2- und ThO_2-CeO_2-Pulver mit variablem Ceroxidgehalt unter Anwendung einer Mitfällungsmethode von Nitratlösungen durch NH3 synthetisiert. Die Auswirkung der Ceriumzugabe auf die Eigenschaften der Pulver wurde bewertet. Die Systeme wurden zunächst charakterisiert, indem man das thermische- und das Kristallisationsverhalten der Pulver in Abhängigkeit vom Ceroxidgehalt untersuchte. Beide Systeme kristallisieren bei hohen Temperaturen (T > 1300°C) in einer stabilen Mischkristall-kfz-Fluorit-Struktur ohne offensichtliche Entmischung von Ceroxid. Ihre Gitterparameter wurden bestimmt und folgen dem Vegard-Gesetz. Für beide Systeme wurde eine kritische Konzentration von 20 mol% Ceroxid definiert. Bei Konzentrationen unter 20 % werden die Eigenschaften des Materials von der Wirtsmatrix bestimmt.

$(Zr,Y,Ce)O_{2-x}$- und $(Th,Ce)O_2$-Pellets mit unterschiedlichem Ceroxidgehalten wurden mit verschiedenen Fabrikationsmethoden hergestellt. Für jeden Fabrikationsschritt wurden basierend auf der Untersuchung der Pulver- und Pellet-Eigenschaften die optimalen technologischen Parameter ermittelt. Mit Hilfe einfacher Herstellungsverfahren (Kalzinierung bei 600°C, Reibmahlen und Fractionierung in Azeton) werden $(Zr,Y,Ce)O_{2-x}$-Pellets mit Dichten bis zu 97 % der theoretichen Dichte (TD) erziehlt. $(Th,Ce)O_2$-Pellets mit Dichten bis zu 98 % der TD werden durch Nachpressen von ungemahlten Pulver erhalten. Für beide Systeme, besitzen die Materialien eine homogene Porenverteilung, ein gut ausgebildetes Gefüge sowie gute mechanischen Eigenschaften.

Résumé

La réduction de la radiotoxicité à long terme des déchets nucléaires est envisagée par la séparation sélective du Plutonium et des actinides dits mineurs (Américium (Am), Curium (Cm), Neptunium (Np)) suivie de leur transmutation (P&T partitioning and transmutation strategy). Leur conditionnement (P&C partitioning and conditioning strategy) est considéré comme une alternative à la transmutation, au cas où la transmutation ne serait pas viable. Ces deux options (transmutation et conditionnement) nécessitent l'immobilisation de ces actinides dans des matrices denses et stables. L'oxyde de zirconium, stabilisé en phase cubique par de l'yttrium ainsi que l'oxyde de thorium, sont des matrices aux propriétés particulièrement attractives.

Le travail suivant présente deux objectifs : déterminer l'impact de l'addition des actinides, simulé par du cérium, sur les propriétés de la matrice et étudier la possibilité de synthétiser des céramiques homogènes en utilisant des méthodes simples de fabrication.

Dans ce cadre, des poudres de $(Zr,Y)O_{2-x}$-CeO_2 et de ThO_2-CeO_2 de concentrations variables en oxyde de cérium ont été synthétisées par co-précipitation de solution nitreuses par de l'ammoniac. L'impact de l'addition de cérium sur le comportement thermique des poudres et leur cristallisation a été étudié en détails par thermogravimétrie couplée à de l'analyse calorimétrique différentielle (TG-DSC) et par diffraction aux rayons-X (XRD). Les deux systèmes cristallisent à haute température dans une solution solide stable, cubique faces centrées, de type fluorite, sans ségrégation d'oxyde de cérium apparente. Le calcul de leurs paramètres de maille a permis d'établir que ces systèmes suivent la loi de Vegard. Pour les deux systèmes étudiés, une concentration critique C_{Cr} de cérium a été évaluée à 20 % molaire. Pour des concentrations de cérium inférieures à C_{Cr}, les propriétés du matériau sont déterminées par la matrice.

Des céramiques à base de zirconium et de thorium ($(Zr,Y,Ce)O_{2-x}$ et $(Th,Ce)O_2$) de concentrations variables en cérium ont été fabriquées. Les voies de synthèses furent établies. Afin d'obtenir des matériaux aux propriétés stables et fiables, des paramètres technologiques de synthèse ont été optimisés en se basant sur l'étude des propriétés physiques des poudres et des céramiques. Ainsi, des céramiques de $(Zr,Y,Ce)O_{2-x}$ ont été fabriquées en utilisant des méthodes de synthèse simples et par voie humide (calcination à 600°C, granulation-fractionnement dans l'acétone). Leurs densités atteignent 97 % de la densité théorique (DT). Dans le cas de l'oxyde de thorium, des céramiques de densités de 98 % DT ont été obtenues par triple compactage de poudres non granulées. Pour les deux systèmes, les céramiques ont une distribution homogène de la porosité, des grains bien formés et de bonnes propriétés mécaniques.

2.   General introduction

During the burning of uranium oxide in nuclear reactors, long-lived actinides such as plutonium (Pu) and the so-called minor actinides (americium (Am), curium (Cm), neptunium (Np), which are responsible for long-term radiotoxicity, are produced. Selective partitioning followed by transmutation (P&T partitioning and transmutation strategy) is in development for the reduction of long-term radiotoxicity. Currently, Pu is already recovered by reprocessing and burned in the reactors in the form of (U,Pu)Ox mixed-oxide fuel. However, because of the presence of uranium, the additional transuranium elements are produced. This implies that although Pu is partly burnt after the irradiation of the fuel there is more Pu generated than burnt e.g.. In recent years, various fuel types or targets have been proposed, among them the fabrication of dedicated fuels with a high content of actinides. In order to reduce the formation of new transuranium elements, inert ceramic support materials which are free of ^{238}U should be developed.

If the burning of actinides is no longer considered, they have to be disposed off. The conditioning of long-lived actinides (P&C partitioning and conditioning strategy) is therefore taken into consideration as an alternative to transmutation. In this case, it is necessary to look for dense matrices that are capable of incorporating a significant amount of minor actinides without considerable deterioration of the matrix properties.

Yttrium fully stabilized zirconium oxide and thorium oxide are very attractive matrices. They have the ability to form solid solutions with actinide oxides. These complex solid solutions are characterised by their high resistibility to temperature, mechanical and radiation impacts, chemical stability in different media including water and highly concentrated salt brines.

However, concerning the immobilisation of actinides in these host phases, two main questions remain:

1- From a chemical and physical point of view, which concentration of actinides can be immobilised in ceramic without degradation of its properties ?

2- Is it possible to fabricate ceramics, with stable and reliable properties by using simple technologies ?

For these reasons, the $(Zr,Y)O_{2-x}$ - CeO_2 (Ce-YSZ) and ThO_2 - CeO_2 powders with variable ceria contents were synthesised, employing a co-precipitation method of nitrate solutions by NH_3. The systems were first characterised by studying the thermal and crystallisation behaviour of the powders as a function of ceria concentration. Then the possibility of using simple technologies and "mild" methods for powder preparation adapted to radioactive material was examined. Thus, pellets with different ceria contents were fabricated and the influence of the ceria addition was studied. For each technological step, the optimum technological parameters (such as calcination temperature, grinding conditions, compacting pressure etc…) were determined based on the investigation of the powder and pellet properties.

3. The nuclear fuel cycle

Until the last ten or twenty years sustainable energy was thought of simply in terms of availability relative to the rate of use. Today, in the context of the ethical framework of sustainable development, other aspects, like the environment, the safety and the question of wastes, are equally important [1].

Different energy resources are available : the renewable, the fossil and the nuclear energies.

The renewable energies such as wind, hydraulic and solar are an appropriate first consideration in sustainable development, because there is no depletion of mineral resources and no direct air or water pollution. But harnessing these "free" sources cannot be the only option. Renewable sources are diffuse, intermittent, and unreliable by nature of their occurrence.

Coal and natural gas are also reasonably abundant in many parts of the world. However, burning fossil fuels produces primarily carbon dioxide as waste, which is inevitably dumped into the atmosphere. And as yet, there is no satisfactory way to avoid or dispose of the greenhouse gases which result from fossil fuel combustion.

Fuel for nuclear power is abundant, and the safety of nuclear energy has been well demonstrated and is being continuously improved. However, nuclear energy produces both operational and decommissioning wastes, which have to be managed. The experience with both storage and transport over half a century clearly shows that there is no technical problem in managing any civil nuclear wastes. Ethical, environmental and health issues related to nuclear wastes are topical, and there is a clear need to address the question of their safe management. Currently different ways have been envisaged for the nuclear waste treatment and management, among them, the partitioning and transmutation strategy that may reduce the long-term radiotoxicity.

3.1. The nuclear energy production

With a production of 361 GWe, the nuclear energy supplies 16% of the electricity in the world., against 64% for the fossil fuels and 19% for the hydro and a very little part from other renewable [2]. As seen on the Figure 1, some countries like Lithuania or France are dependent on their nuclear energy production. In 2004, in Germany, 27.5 % of the electricity has a nuclear origin, produced by 18 reactors [3].
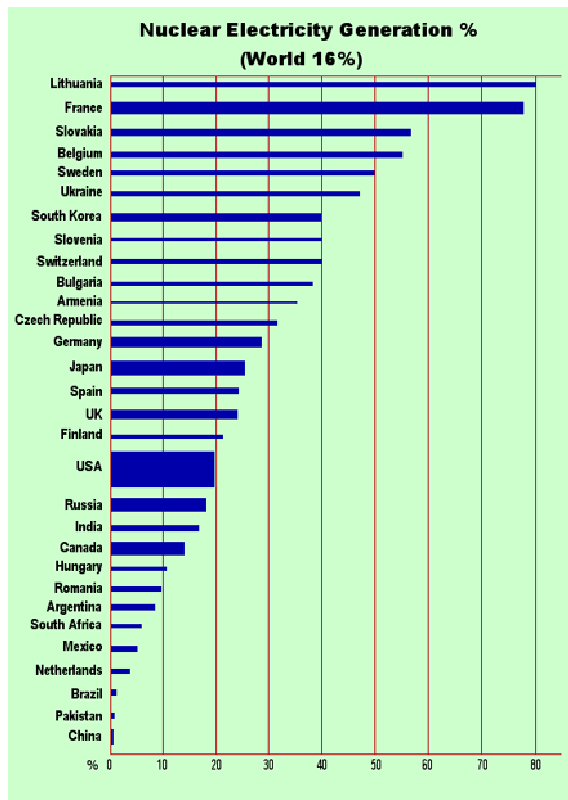
Figure 1. Utilisation (in %) of nuclear energy in different countries [2].

3.1.1. The nuclear energy of uranium

Natural Uranium is mainly composed of two isotopes: ^{238}U (99.3%) and about 0.7% of ^{235}U.

By capture of a neutron, the nucleus of the ^{235}U atom, splits in different parts (fissions reaction), releasing atoms possessing kinetic energy and two or three additional neutrons. These expelled neutrons react with other nucleus, producing other fissions reactions and so creating a chain reaction. This process, in effect "burning" uranium, occurs in a nuclear reactor. Whereas the ^{235}U atom is 'fissile', the ^{238}U atom is said to be 'fertile'. By neutronic capture ^{238}U becomes ^{239}Pu, which is also fissile. Because there is ^{238}U in a reactor core in excess, these reactions occur frequently, and in fact about one third of the energy yield comes from "burning" ^{239}Pu [4].

The principles for using nuclear power to produce electricity are the same as for most types of conventional incineration facilities. As described in Figure 2, the kinetic energy of the released atoms after continuous fission of the fuel is transferred as heat in either a gas or water, and is used to produce steam. The steam is used to drive the turbines which produce electricity [5].

The chain reaction that takes place in the core of a nuclear reactor is controlled by rods which absorb neutrons and which can be inserted or withdrawn to set the reactor at the required power level. These rods are made from material such as cadmium, hafnium or boron. The fuel elements are surrounded by a substance called moderator to slow the speed of the emitted neutrons and thus enable the chain reaction to continue. Water, graphite and heavy water are used as moderators in different types of reactors [4, 5].

22
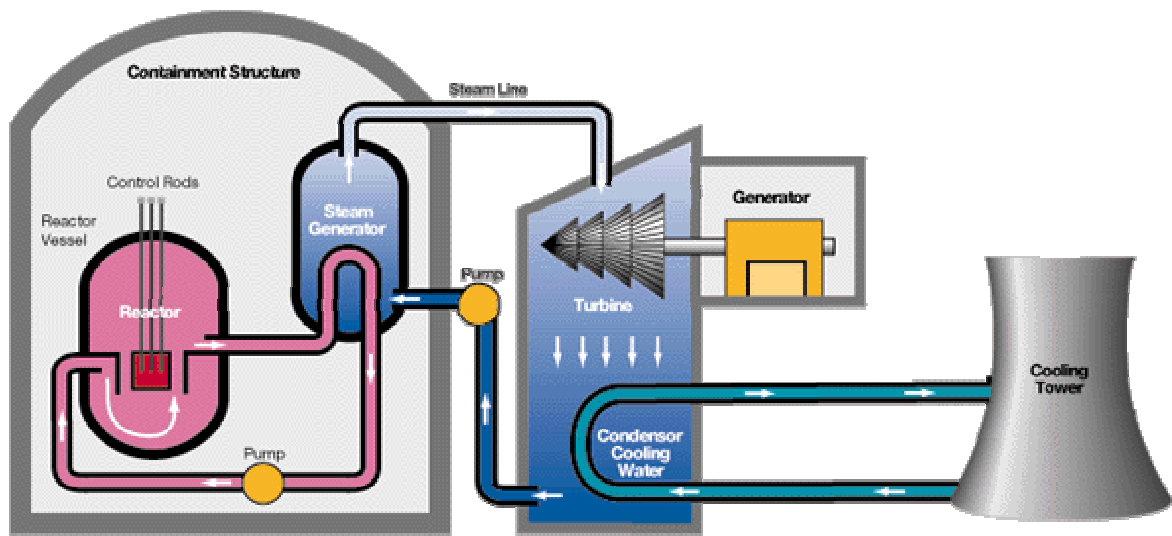
Figure 2. Representation of a pressurised water reactor (PWR) [6].

3.1.2. The different types of reactor

Different type of reactor exists (Table 1). All are characterised by three essentials components: the fuel, the moderator and the coolant. Sometimes moderator and coolant are the same medium. The coolant has to transfer the heat decay coming from the core and reactor to the steam generator, responsible of turbine rotation.

If graphite or heavy water is used as moderator, it is possible to run a power reactor on natural instead of enriched uranium. In enriched uranium the fissile isotope (^{235}U) concentration is increased up to the level of 3.5 - 5.0%, by a preliminary enrichment process. In this case the moderator can be ordinary water, and such reactors are collectively called light water reactors. Because water absorbs neutrons as well as slowing them, it is less efficient as a moderator than heavy water or graphite.

Practically all fuel is ceramic uranium oxide (UO$_2$ with a melting point of 2800°C) and most is enriched. The fuel pellets (usually about 1 cm diameter and 1.5 cm long) are typically arranged in a long zirconium alloy (zircaloy) tube to form a fuel rod, the zirconium being hard, corrosion-resistant and permeable to neutrons [5, 7].

88 % of the nuclear electricity is generated using just PWR and BWR, reactors which were developed in the 1950s and improved to better designs (2nd generation). Newest design is European Pressurised water Reactor (EPR -3rd generation). The first generation comes to the end of their operating lives.

Table 1. Nuclear power plants in commercial operation [5].

Reactor type	Main Countries	Number	GWe	Fuel	Coolant	Moderator
Pressurised Water Reactor (PWR)	US, France, Japan, Russia	263	237	enriched UO_2	water	water
Boiling Water Reactor (BWR)	US, Japan, Sweden	92	81	enriched UO_2	water	water
Gas-cooled Reactor	UK	26	11	natural U, enriched UO_2	CO_2	graphite
Pressurised Heavy Water Reactor 'CANDU'	Canada	38	19	natural UO_2	heavy water	heavy water
Light Water Graphite Reactor	Russia	17	13	enriched UO_2	water	graphite
Fast Neutron Reactor (FBR)	Japan, France, Russia	3	1	PuO_2 and UO_2	liquid sodium	none
TOTAL		439	361			

GWe = Gigawatt electric

3.2. The nuclear fuel cycle

The part is mainly based on the work of Uranium Information Center (UIC) [4] and Morvan [7].

Uranium is an energy resource which must be processed through a series of steps to produce an efficient fuel for use in generating electricity. To prepare uranium for use in a nuclear reactor, the ore undergoes the steps of mining and milling, conversion, enrichment and fuel fabrication (Figure 3). These steps make up the 'front end' of the nuclear fuel cycle. After uranium has been used in a reactor to produce electricity it is known as 'spent fuel' and may undergo a further series of steps including temporary storage, reprocessing, and recycling before eventual disposal as waste (Figure 3). Collectively these steps are known as the 'back end' of the fuel cycle. These various steps together make up the entire nuclear fuel cycle.

3.2.1. The "front end"

Uranium ore is usually mined, milled and converted into U_3O_8 named "Yellow cake". The yellow cake is then converted into the gas uranium hexafluoride (UF_6), before being enriched in ^{235}U. Enriched UF_6 is transported to a fuel fabrication plant where it is reconverted to uranium dioxide (UO_2) powder, pressed into small pellets and sintered at 1700°C. The final pellets are inserted into thin tubes, usually of a zirconium alloy (zircalloy) or stainless steel, to form fuel rods. The rods are then sealed and assembled in clusters to form fuel assemblies for use in the core of the nuclear reactor.
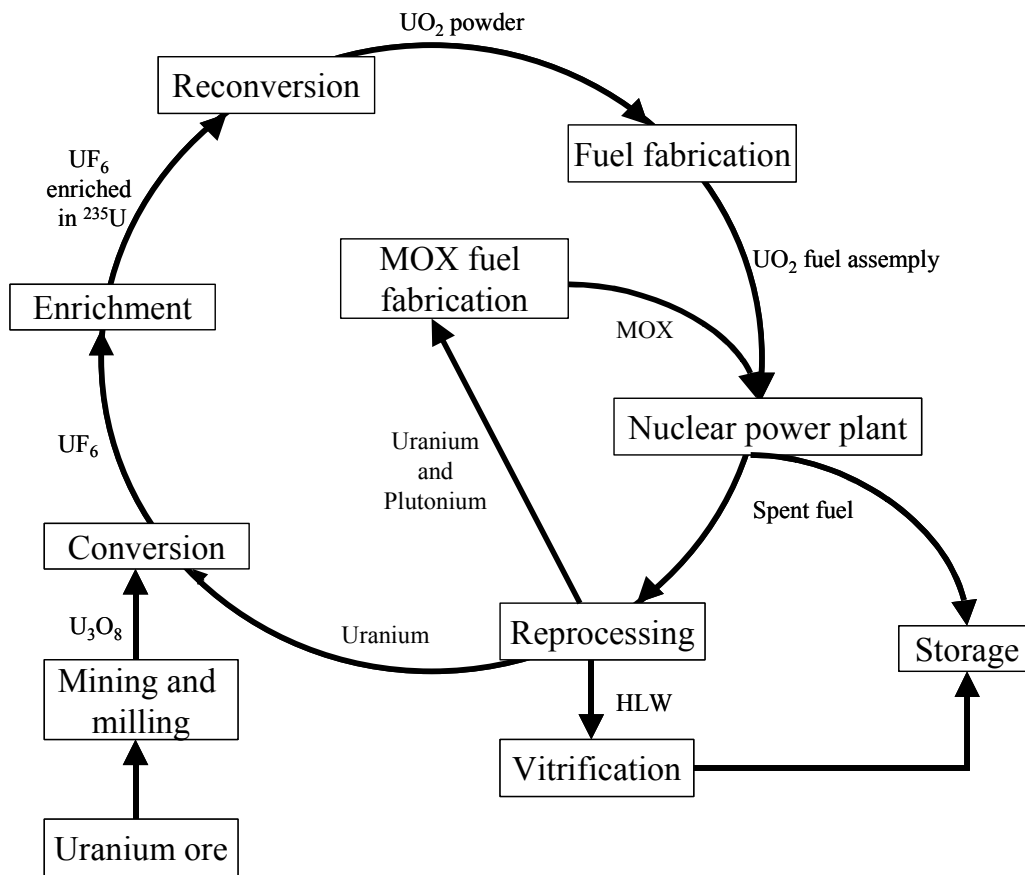
Figure 3. Schematic representation of the Nuclear Fuel Cycle.

Several hundred fuel assemblies make up the core of a reactor. For a reactor with an output of 1000 megawatts electric (MWe), the core would contain about 75 tonnes of low-enriched uranium. To maintain efficient reactor performance, about one-third of the spent fuel is removed every year or 18 months, to be replaced with fresh fuel.

3.2.2. The spent fuel

During the burning of Uranium in a reactor, about 40 elements are produced either by fission or by neutronic capture. So, after irradiation in a reactor for 3 to 4 years, the spent fuel consists of 94.3% of ^{238}U, 0.8% of ^{235}U and 1% of Pu (Figure 4). The other 4 % of elements in the fuel consists mainly of

- fission products (3.5%),
- ^{236}U (0.4%),
- and the so called minor actinides (MA) : ^{237}Np (0.05%), ^{243}Am (0.01%) and ^{244}Cm (0.004%).
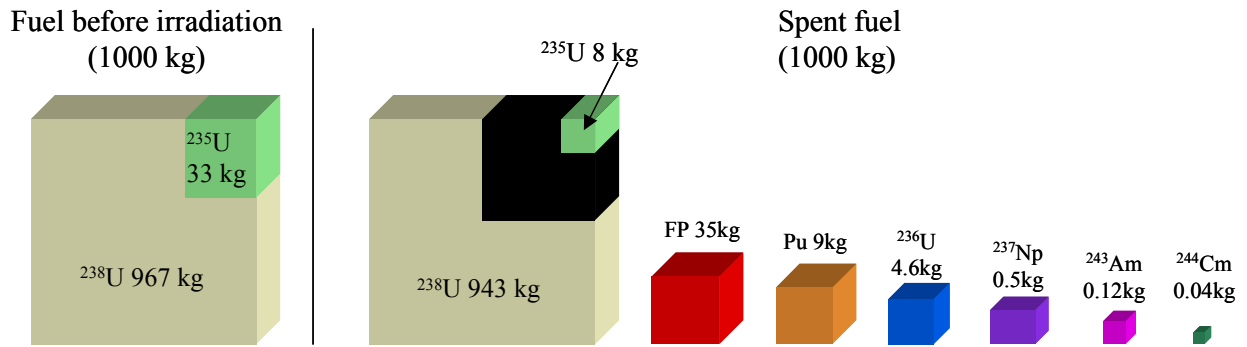
Figure 4. Element composing UO₂ fuel before and after irradiation for 3 years at 33 GWd/t in PWR [8].

The fission products result from the fission of ^{235}U and ^{239}Pu. The transuranics (Np, Pu residual, Am and Cm), result from the successive neutronic capture of Uranium (Figure 5). The fission products emit β and γ radiation, while the transuranics emits α, β and γ radiations. These elements are responsible of 99% of the radioactivity of the spent fuel [9].
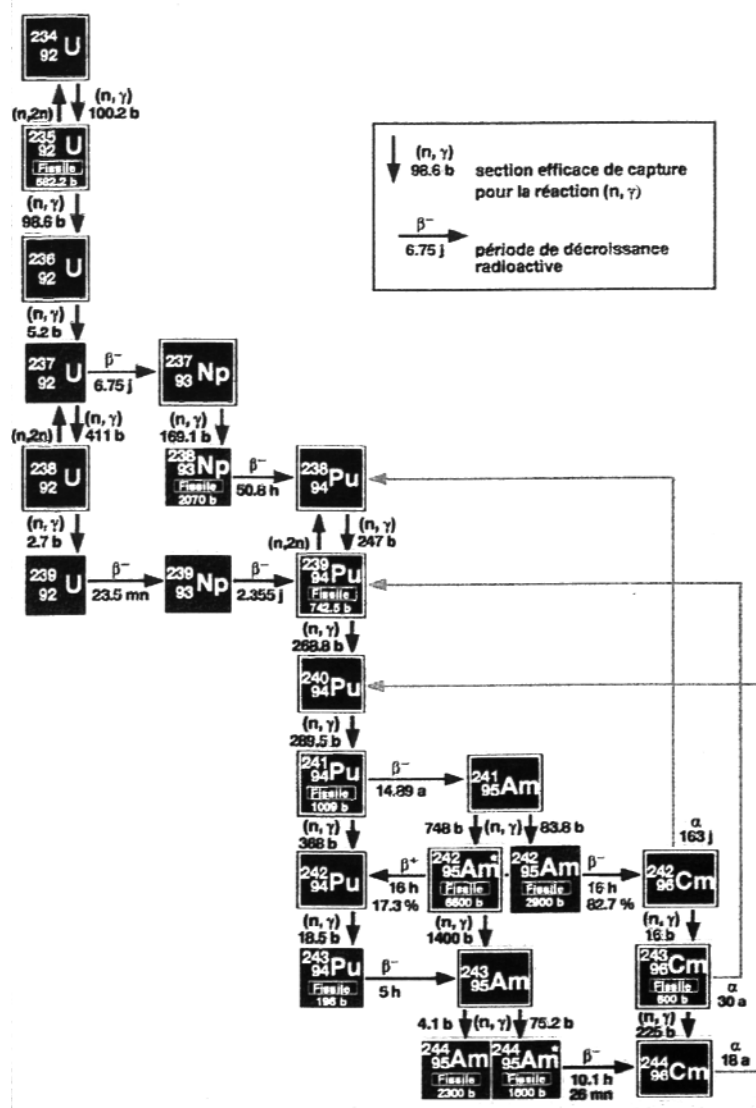
Figure 5. The production of Pu and the MA.

3.2.3. The "back end"

Spent fuel assemblies taken from the reactor core are highly radioactive and release a lot of heat. They are therefore stored in special pools for 1 to 2 years to allow both their heat and radioactivity to decrease. The spent fuel can also be dry stored in engineered facilities, and cooled by air. After a long cooling time of about 50 years, the spent fuel can be then sent to a repository. In this case, the nuclear fuel cycle is named "opened fuel cycle".

However, the uranium and the plutonium have a large energetic potential. This energy source should be exploited, by recovery of the uranium and the plutonium. During reprocessing of the fuel, uranium and plutonium are separated from the other elements and transformed in UO_2-PuO_2 mixed oxide (MOX) fuel to be used in the reactor. The other elements, are directed to the High Level Waste (HLW), currently conditioned in a glass matrix and stored in an intermediate storage.

3.2.3.1.Reprocessing

For reprocessing the fuel rods are chopped and the fuel is dissolved in concentrated nitric acid. U and Pu are selectively extracted from the nitric solution by an organic solution containing tributylphosphate diluted in n-dodecane. This liquid-liquid extraction process is named PUREX (Plutonium Uranium Refined by EXtraction) and separates U and Pu from the fission products and minor actinides. This process is industrially exploited in France and in United Kingdom. The zircaloy hulls remain in the acid solution undissolved and will be treated as waste by cementation or hypercompaction.

3.2.3.2.MOX fabrication [10, 11]

After separation, recovered uranium is returned to the conversion plant for conversion to uranium hexafluoride and subsequent re-enrichment. The Pu after recycling is used to fabricate MOX fuel. It can be fabricated in two ways. First PuO_2 can be mixed with natural uranium oxide or by mixing with depleted uranium issued from the enrichment step, with a Pu concentration of 3 to 12.5%.

The MOX is industrially prepared employing the following route (Figure 6).

After separation of U and Pu by the PUREX process, the nitrate solutions are first thermally treated to obtained UO_2 and PuO_2. The powders are then mixed in two steps. First, UO_2, PuO_2 and defected MOX pellets are mixed and milled until a fine and good blended mixture is obtained. The concentration of Pu in this primary mixture reachs a value of 30%. Then UO_2 is added to the primary mixture to obtain a concentration of 3 to 12.5 % of Pu depending of the needs of reactors. The final mixture is then pressed, sintered, polished and controlled. The pellets with acceptable properties will consist the MOX fuel assembly and the non suitable pellets as well as the polishing powder waste are recycled in the primary mixture.
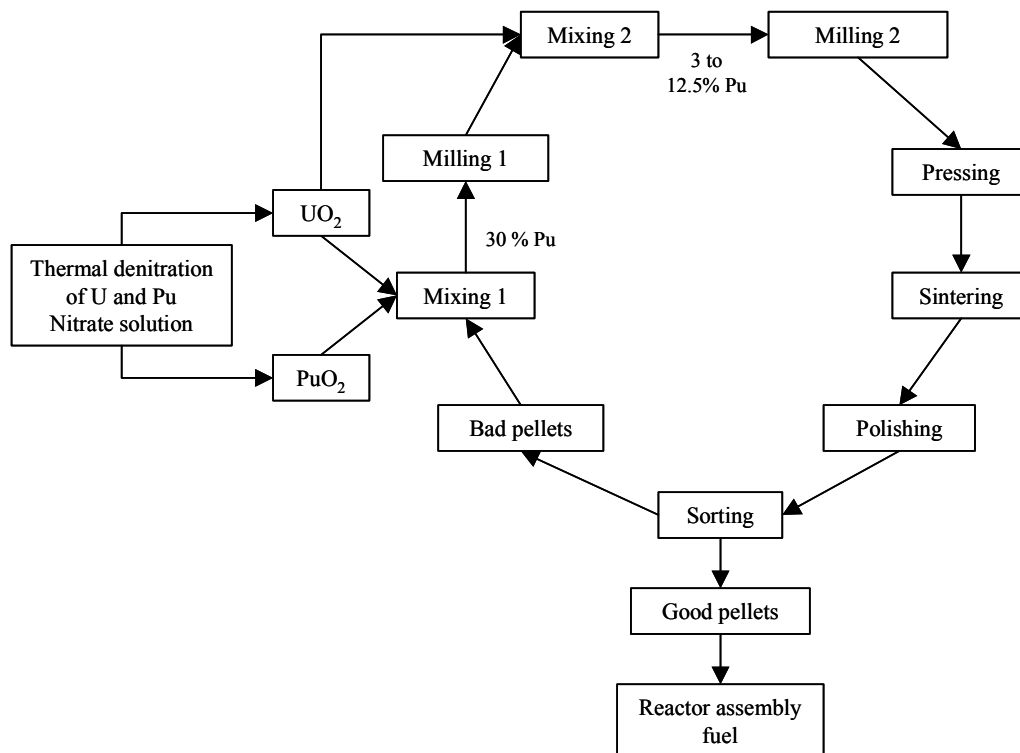
Figure 6. Fabrication route of (U,Pu)-mixed oxide fuel [10].

MOX fuel fabrication occurs at facilities in Belgium, France, UK, Russia and Japan, with more under construction. Across Europe about 30 reactors are licensed to load 20-50% of their cores with MOX fuel and Japan plans to have one third of its 54 reactors using MOX by 2010.

3.2.3.3. Vitrification

After reprocessing, the remaining 4% of high-level radioactive wastes (approx. 750 kg per year from a 1000 MWe reactor) are calcined to produce a dry powder. This powder is incorporated into borosilicate (Pyrex) glass, in order to immobilise the waste [12]. In fact, the glass has the capacity to immobilise atoms of different radius and properties, giving an homogeneous mixture, stable in time. The current vitrification is industrially exploited and the vitrified high-level wastes are sealed into stainless steel canisters.

3.2.3.4. Final disposal

The waste forms envisaged for disposal are vitrified high-level wastes or spent fuel rods encapsulated in corrosion-resistant metals such as copper or stainless steel. The most widely accepted plans are for these to be buried in stable geologic structures deep underground. Many geological formations such as granite, volcanic tuff, salt or shale are under investigation for suitability.

3.3. The management of plutonium and HLW

3.3.1. The radiotoxicity balance

The HLW is composed from mainly 40 elements with variable concentrations and large variation in half-life time. The fission products like ^{137}Cs and ^{90}Sr have a relative short half life of 30 years but dominate at the beginning the intense radioactivity and heat decay of the HLW. However, they will gradualy disintegrate in 1000 years: a storage with an historical scale is possible.

On contrary, same long lived fission products like [135]Cs, [129]I and ^{99}Tc as well as the residual Pu and Minor actinides (Am, Cm and Np) represent a small volume, but have a longer decay time. However, these nuclides dominate the long-term radiotoxicity inventory, which remains as hazard over 10^5 years, far beyond human perception [13, 7].

According to the Figure 7, it is evident, that the radiotoxicity potential is dominated by plutonium ([239]Pu, [240]Pu, [242]Pu) and americium ([241]Am, [243]Am). After about 1000 years the primary Am-isotopes are mostly decayed and the Pu-isotopes are dominating. These will be substituted after 200.000 years by neptunium. The relatively long-lived fission products ^{99}Tc and [129]I have a radiotoxicity potential of one order of magnitude below [237]Np [14].
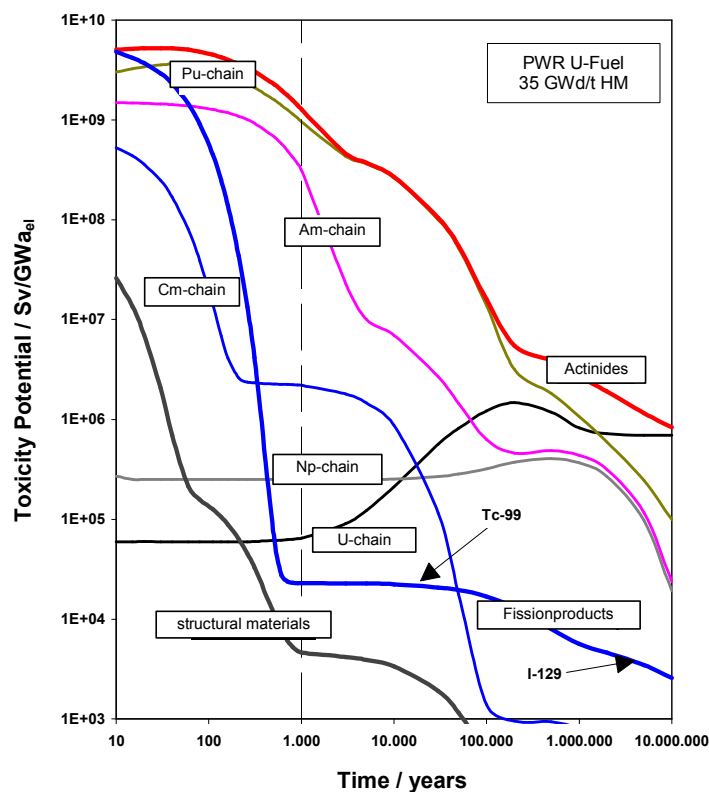
Figure 7. Time dependent toxicity potential (ingestion) of decay chains by elements of PWR spent fuel [15].

3.3.2. The management of long-lived elements

To improve the long-term safety, different strategies have been foreseen for the treatment of the Pu, MA, responsible of the long-term radiotoxicity. The idea consists in a selective partitioning of all of these elements followed by a selective treatment.

First, the transmutation, which consists in the transformation of the long-life radionuclide to short-life or stable radionuclide, induced by neutron is considered. It is defined as the Partitioning and Transmutation (P&T) strategy. The application of a P&T strategy would, if fully implemented result in a significant decrease in the transuranic inventory to be disposed of in geological repositories. Currently, it is believed that the inventory and radiotoxicity can be reduced by a factor of 10^4 and that the timescale requires for the radiotoxicity to reach reference level (natural uranium) will be reduced from over 1 million of years to between 1000-5000 years [16]. In fact, as described in Figure 8, the current reprocessing technique of U and Pu, can reduce long-term radiotoxicity level by about one order of magnitude. However, if U and Pu are separated to a higher level and if additionally Np, Cm and Am are partitioned to a high extent and transmuted, the radiotoxicity potential level of HLW will decrease after approximately 1000 years to the level of fresh nuclear fuel [14].
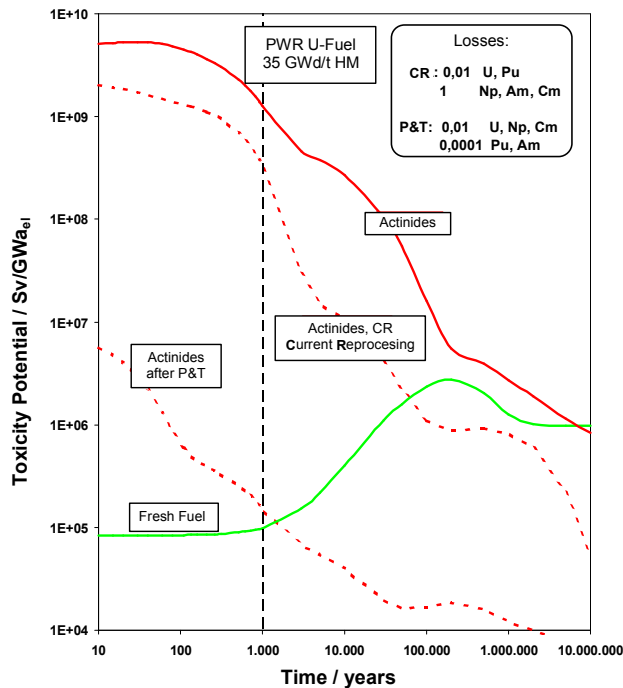
Figure 8. Influence of direct disposal, reprocessing and P&T on the time dependent toxicity potential and the comparison with introduced fresh fuel [15].

Alternatively to the transmutation, the conditioning, through the Partitioning &Conditioning (P&C) strategy is considered as another strategy. It consists in the immobilisation of the long lifed elements in a stable inert matrix either in a product for final disposal or in product for

intermediate storage for future irradiation target or inert-matrix fuel until transmutation facilities become available [16].

3.3.3. The partitioning strategies

A high selective partitioning of the U, Pu and MA, followed by a transmutation may reduce the long-term radiotoxicity. As described in Figure 9, U and Pu are currently separated from the spent fuel by using the PUREX process. Extendly, an improved PUREX process would allow already today a selective partitioning of Np, Tc and I.

A lot of laboratory scale processes have been studied and can be used for more selective partitioning. The trivalent actinides can be separated from the fission products. This is foreseen to be done using liquid-liquid extraction e.g. using a diamide as organic solvent (DIAMEX process developed in Europe). However, the lanthanide and actinides having very similar properties, they are co-extracted (Figure 9) and separated together from the fission products.

A selective partitioning of the trivalent actinides in regards to the trivalent lanthanide must be then performed. This is proposed to be done by the SANEX-process [17] (Figure 9). Thus, as example, in Germany, ALINA process has been developed to fullfil this difficult task. A synergistic mixture of a bis(chlorophenyl)dithiophosphinic acid ($(ClPh)_2SSH$) and tri-n-octylphosphine oxide (TOPO) was proposed to perform this separation.

Am and Cm can finally be separated by using a SESAME process (Figure 9). The fission products as well as the lanthanides can be either vitrified or immobilised in other matrices like ceramics for a disposal [16].
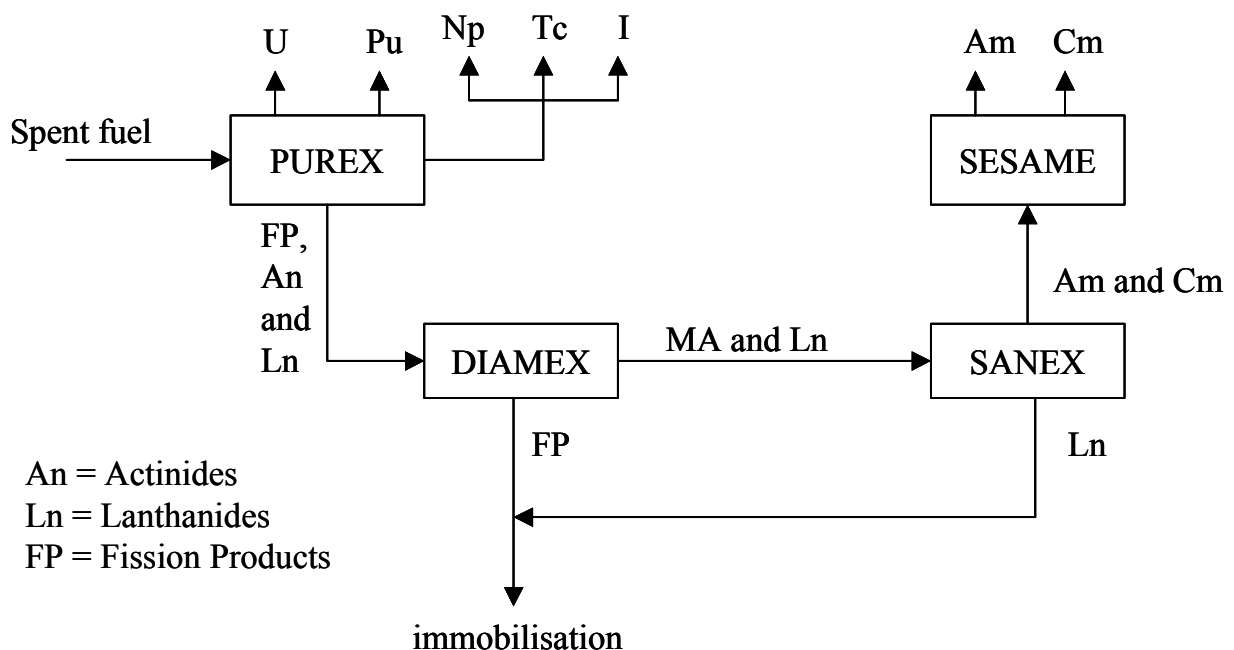
Figure 9. European partitioning strategy [16, 7].

3.3.4. The transmutation strategies

This part is mainly based on the report of Vergnes [9] and NEA-OECD reports [18 - 20]

The transmutation differs only by the energy of the neutrons used for the nuclear reaction, thermal (employed in PWR) or fast neutrons (employed in FR) and the type of fuel used in reactor (homogeneous or heterogeneous). Thermal neutron reactor allow to transmute Pu and MA, however, the best transmutation rate are obtained in FR [18].

Other type of systems, hybrids system, specific for the incineration of the MA are under investigation. In an Accelerator Driven System (ADS) a high-power proton accelerator is used to produce neutrons by spallation in a heavy-metal target (W or Pb). The neurtons are used to "transmute" transuranium elements and long-lived fission products in a subcritical reactor core. The transuranium elements are "transmuted" by fission reactions, thus producing additional neutrons and energy. Some long-lived fission products are "transmuted" by neutron capture converting them into short-lived or stable radionuclides. A schematic representation of the ADS system is given in Figure 10.
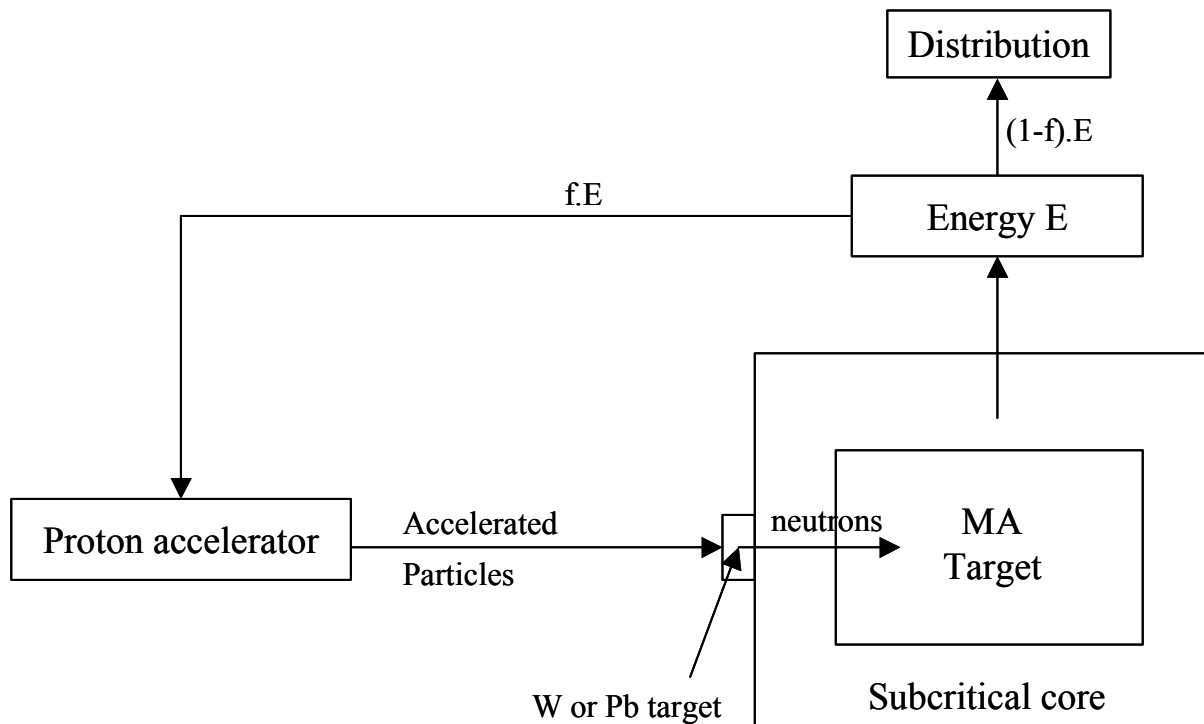
Figure 10. Principle of an ADS system [19, 20].

Thus, different strategies are proposed to transmute the Pu, MA and some long life fission products (LLFP).

During the recycling of Pu as MOX in a reactor, only one quarter of the Pu initially charged in the reactor is burned and one fifth has been transformed in MA. Moreover, the U of the MOX has produced important quantities of new Pu. So, to obtain a complete elimination of Pu and MA it seems necessary to recycle them in a multi-recycle strategy or to remplace the UO_2 by ThO_2.

3.3.4.1. Multi-recycling of Pu

The multi-recycling of Pu on an U support in a PWR as described in Figure 11, is for feasibility question impossible. In fact, the isotopic composition of Pu varies with the number of recyclings: the ^{239}Pu (fissile) concentration is decreasing. However, the ^{238}Pu and ^{242}Pu isotopes (neutrons absorbers) are generated and so are responsible for a strong increase of the total Pu concentration. Thus, after 2 or 3 recycling the safety criteria of reactor are not assured anymore and moreover, the multi-recycling would be responsible of a strong production for MA.
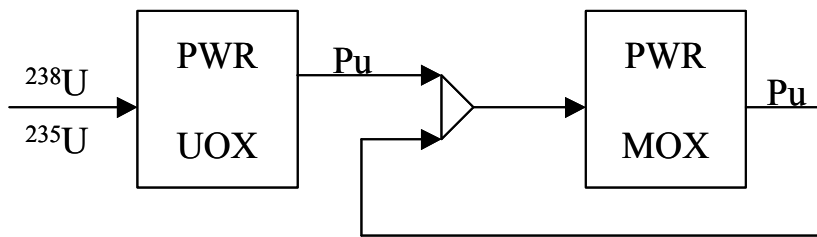
Figure 11. Multirecycling of Pu in PWR.

The utilisation of an inert or quasi-inert support, non or less producer of MA can be employed to improve the consumptions rates of Pu [21 - 25]. Thus the Thorium oxide matrix is promising in this frame. The burn up of (Th,Pu)oxide gives much higher Plutonium consumption rates than (U,Pu)oxide and its actinide production being very low. Moreover, reactor physics calculations show that a full Th/Pu core seems feasible [26 - 33].

Thus, as calculated in the work of Kugeler et al. [34], if Pu is burned in a reactor under the form of (U,Pu)oxide at the level of 50 GWd/t$_{SM}$, then 120 % of Pu and 10 % of MA are formed during irradiation and 38 % of this plutonium is not fissile. On contrary, if all uranium is remplaced by thorium, then for an incineration of 60 GWd/t$_{SM}$, only 54 % of the plutonium remains, 48% being non fissile.

Contrary to the multi-recycling of Pu in PWR, the recycling of Pu first in PWR followed by a multi-recycling in fast reactor (FR) does not present any feasibility problem (Figure 12). The concentration of ^{239}Pu decreases during the transmutation and the ^{238}Pu and ^{242}Pu remains fissile in FR. However, the total concentration of Pu slightly varies during the multi-recycling.
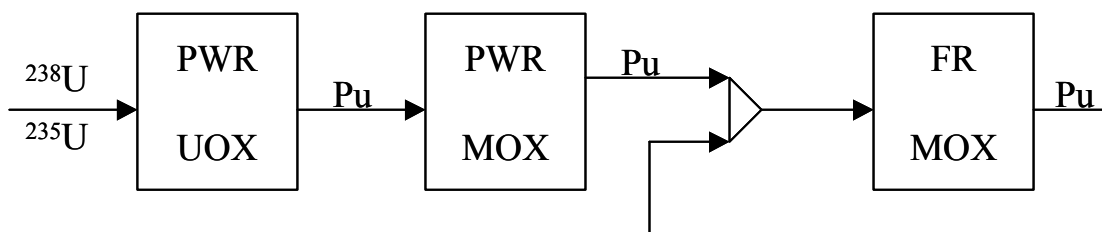
Figure 12. Multirecycling of Pu in PWR and FR.

3.3.4.2. Simultaneous recycling of Pu and MA.

To recycle Pu and MA simultaneously, two types of recycling have been foreseen.

The first possibility consists in mixing Pu and MA to the uranium fuel: this method is called homogeneous recycling. To recycle the MA with U in a PWR, it is necessary to increase the concentration of ^{235}U to 1.5% per percent of MA, because the MA are neutrons absorber in PWR. Moreover, their recycling in MOX on U support is responsible for an increase of the Pu concentration. Thus, the recycling of MA in PWR is so impossible.

In a fast reactor, MA are slightly fissile. Their homogeneous recycling does not require an excess of neutrons and the Pu concentration does not increase. The SUPERFACT experiment has already demonstrated that the addition of some MA in a standard fuel like MOX does not change its properties [18]. However, the presence of MA reduce the safety margins of the reactor. So their transmutation is so possible in FR but the admissible quantities are very limited.

The second possibility consists in immobilising the MA in an inert target (free of U). Pu and MA are separated. The recycling is heterogeneous. These targets containing minor actinides can be placed in the core of reactor or at the periphery. In the core, they are subjected to high neutronic fluxes and the incineration ratio is quite high. However, for safety reasons, their quantity must be limited. In the periphery of the core, the targets are subjected to weaker neutronic fluxes and have lower incineration ratio. Thus they do not create strong perturbation of the reactor. However, the transmutation efficiency remains weak and a multi-recycling strategy is required. It is also necessary to consider the reprocessing-ability of the target after irradiation.

An unique recycling of Pu and MA immobilised in a complete inert support can be also foreseen. In this case a very long time (several tens of years) of irradiation in order to fission the maximum of nucleus is required as well as an inert support extremely resistant to irradiation.

Thus, the recycling of MA requires the development of fuel or target, being able to contain large quantity of ^{241}Am and ^{244}Cm, responsible of strong gamma and neutron emission, and so requiring adapted radioprotection [35].

The efficiency of the multirecycling of Pu and MA using PWR and FR has been evaluated. A multi recycling of Pu would reduce the radiotoxicity of a factor 5, while the multirecycling of Pu, Np and Am of a factor 30 and a multirecycling of Pu and all MA of a factor 100.

3.3.4.3. The Long-life fission products (LLFP) transmutation

The transmutation of LLFP is a very difficult task because the capture cross-sections to transmute the radioactive nuclides are very small. In this way, very long irradiation periods are necessary to obtain a significant depletion. This can only be realized in dedicated reactors with large thermal fluxes and/or ADS.

From a technological point of view, the transmutation of ^{99}Tc is the easiest approach since it is transmuted into stable metallic ^{100}Ru isotope. However, the time necessary to deplete the target with 50 % is about 30 years.

From a neutronic point of view, the transmutation of ^{129}I is very similar to that of ^{99}Tc, but the target product is chemically unstable and the neutron capture reaction produce ^{130}Xe which has to be vented from the irradiation capsule during its stay in the reactor.

The radionucleides ^{93}Zr and ^{135}Cs cannot be considered for reactor transmutation unless they can not be separated from the other Zr and Cs isotopes before being submitted to irradiation.

3.3.4.4.Accelerator Driven Systems (ADS) or hybrids reactors

Until 1990, the transmutation of Pu and MA in critical reactors was considered. Today, it appears interesting to consider another type of nuclear reactor, subcritical controlled by an external neutronic source, the ADS system. The main interest of these reactors is the possibility to consider fuel mainly composed from MA, which is impossible in critical reactor for safety reasons. Moreover, these reactors may dispose from an excess of neutrons, that can be utilized to transmute fission products [20]

3.3.4.5.Dual strata strategies

The principle of a dual strata strategy (Figure 13) is to restrict the impact of the MA and their treatment (partitioning, fabrication of specific fuels, specifics reactors and recycling) in a dedicated cycle "Waste transmutation cycle". This is separated from a cycle dedicated to the energy production, "Energy production stratum", in which Pu can be recycled using PWR and FR [36]. The ADS takes all its interest in a dual-strata strategy.
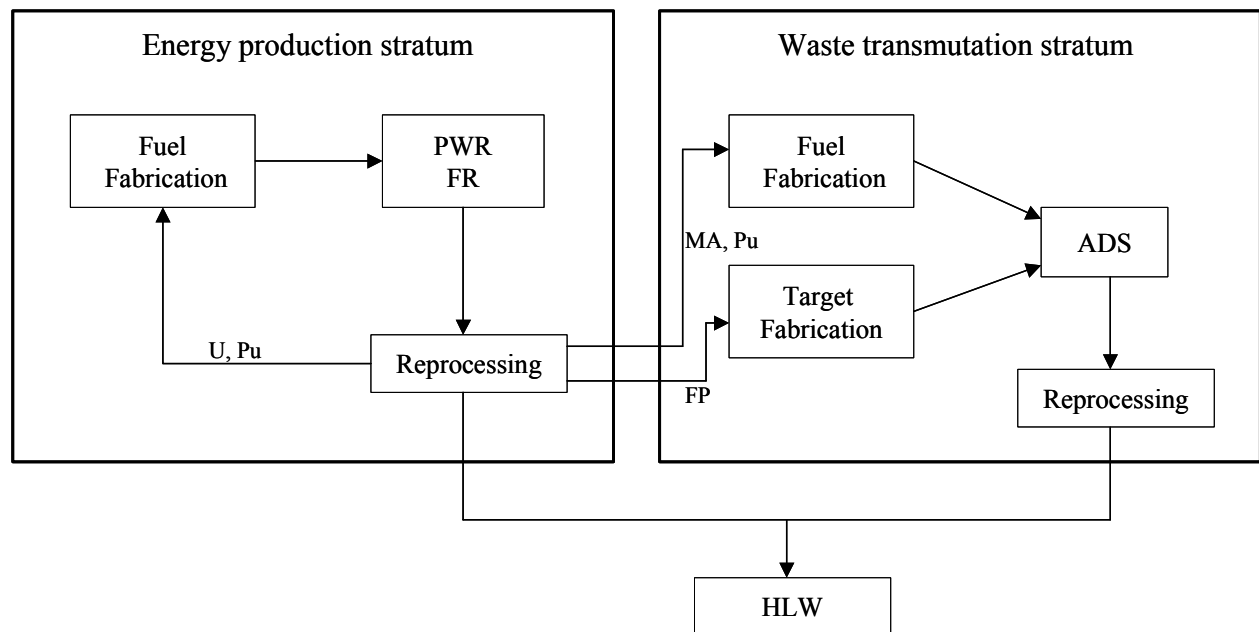
Figure 13. The dual –strata strategy [36].

An application of this concept can be foreseen with the following fraction of reactors (Figure 14).
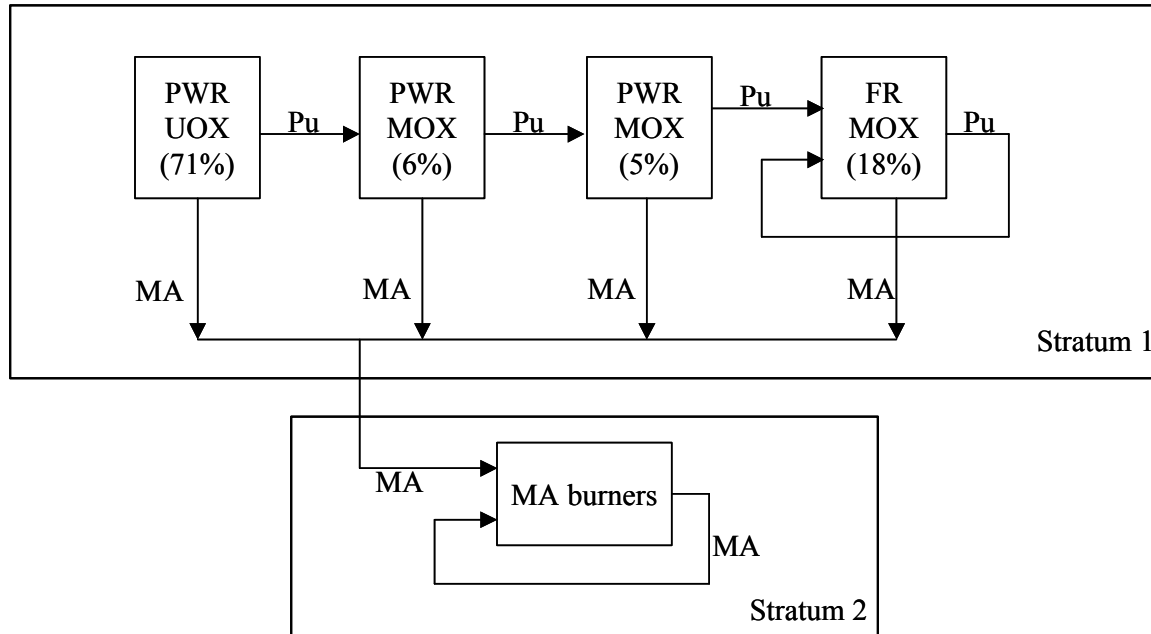
Figure 14. Schematic representation of a possible application of the dual strata strategy [19].

In a first strata, the U is first burned in normal PWR (71% of the nuclear park). The Pu is then recycled (MOX) a first time in PWR (6% of the nuclear park), then recycled a second time (MOX) in PWR (5% of the nuclear park) of and finally in FR (18% of the nuclear park). After each irradiation in reactor the fuel is reprocessed and the MA are collected and converted into fuel. Their transmutation can be performed in a second dedicated strata, composed from critical (FR) or sub-critical reactors (ADS). To reach an equilibrium, 6% of the park should be equipped with ADS.

This reactor park allows a reduction of the potential radioactivity of a factor 100 comparing to an open cycle. This type of park produces an excess of neutrons that can be used to transmute the LLFP, which are strong neutron consumers.

Moreover, it can be possible to burn Pu in a thorium matrix in order to increase the burn up of Pu.

3.3.4.6.Summary of the transmutation strategy

To conclude, different transmutation strategy have been foreseen for the management of the Pu and the MA. They are summarized in the Figure 15.

```
┌─────────────────────────────────────┐
│     Partitioning and Transmutation   │
└─────────────────────────────────────┘
```

Homogeneous recycling in PWR and FR	Heterogeneous recycling -Pu and MA recycled in the same core -Pu used as standard fuel and MA as target at the periphery	Dedicated reactors Dual-strata strategy: -Pu in „Energy production stratum" -MA as fuel in burner (like ADS)
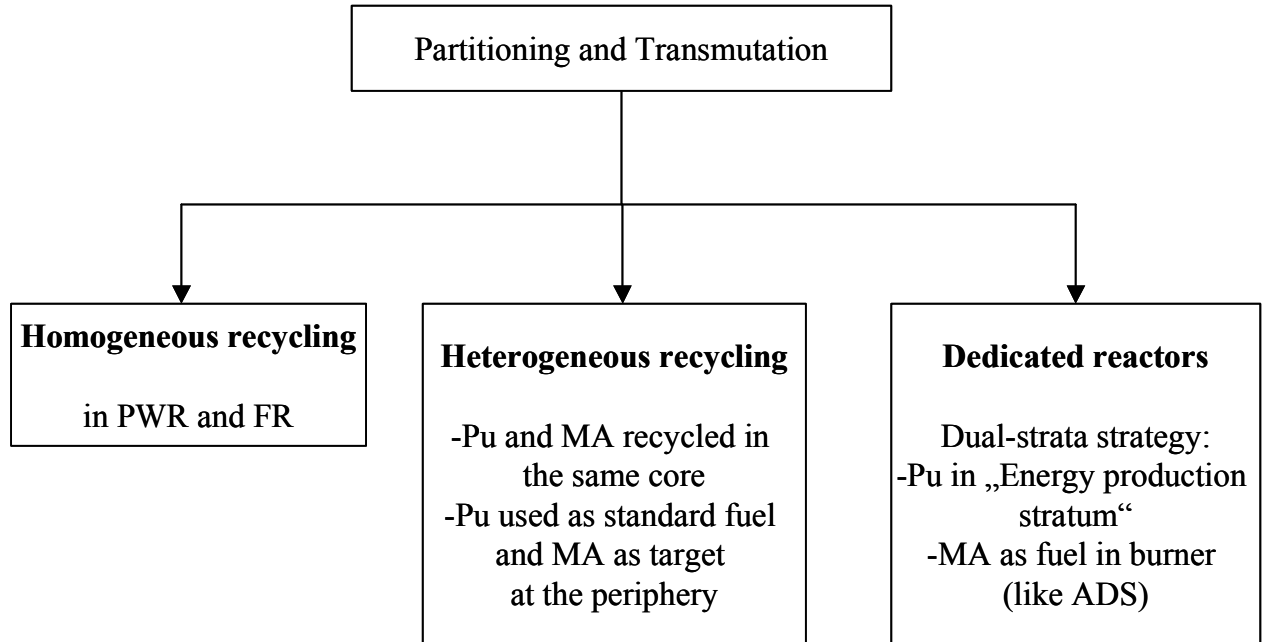
Figure 15. Partitioning and transmutation strategies.

3.3.5. The conditioning strategies

Currently the FP and MA are vitrified together in borosilicate glass (R7T7) [12], disposed in an interim storage before being sent to final disposal.

However, the fission products ^{137}Cs and ^{90}Sr dominate the radiotoxicity for the first 100 years and the LLFP, Pu and MA are responsible of the long-term radiotoxicity. Thus, the safety of a final storage can be improved if these elements are immobilised in dedicated matrices, adapted for each of those elements (LLFP, Pu and MA). The immobilisation of the radionuclide in ceramic matrices is under investigation all over the world. In fact, ceramics are very stable materials and resistant to the auto-irradiation [37]. They are thermodynamically more stable than glass and so more suitable for the immobilisation of actinides. However, contrary to the glass, the cations to be immobilised should substitute the cations in the crystalline net to form a solid solution; the coordination, size of site and charge are so defined by the matrix [38].

Moreover, the conditioning strategy can be also considered as a intermediate storage until transmutation facilities become available. In this respect, the development of ceramics that can be used either for a transmutation or a conditioning strategy is the best option.

3.4. Advanced ceramics for the immobilisation of Pu and MA

This part is mainly based on the work of Koning [36].

The heterogeneous recycling or transmutation of Pu and MA in dedicated reactors, as well as the conditioning strategy require the development of advanced ceramics, extendly fuels/targets, with a high content of plutonium and minor actinides. Ceramics that can be used for both purposes are suitable.

3.4.1. Required properties for the ceramics

The fuel/target should contain only plutonium and minor actinides as fissile/fertile material in a ratio that may vary between 1:5 to 5:1. Such material is considered as a fuel when the isotopic composition gives rise to a critical or a reasonably subcritical core, and a target when it does not contribute significantly to the criticality of the reactor core. To improve the transmutation efficiency, non-fissile (inert) matrix, free of ^{238}U, are considered either as support or diluent of the actinide phase. In a homogeneous fuel or target, the diluent forms one phase (a solid solution) with the actinides, in a heterogeneous fuel or target the actinide phase coexist with the diluent (a dispersion). Of course, combinations of the two concepts or non-diluted fuels or targets need to be considered as well. Furthermore, to achieve a reasonable transmutation efficiency, a high burn-up of the fuel/target is required. The fuel should also satisfy the criteria in view of the concomitant high fission-gas production, fuel swelling and fuel cladding chemical and mechanical interaction.

Moreover, for a safe final disposal, the developed ceramics should be able to immobilise a large quantity of the actinides, should be as stable as possible over long period of time and should have a strong resistance to leaching, oxidation and auto-irradiation. In addition, the volume of the final product should be less than the volume of the solution containing the elements [38].

Because of the high content of plutonium and minor actinides, the radioactivity of the virgin fuel material is much higher than in case of UO_2 or MOX fuel. Specific radioprotection, like remote handling are required during the fabrication step to shield gamma and neutron radiation. This needs to be considered as a criterion and therefore the fabrication process should be as simple as possible [38, 39].

3.4.2. The different type of advanced fuel

Different kind of fuel have been also foreseen: metal fuel, nitride fuel, carbid fuel, oxide fuels and composite fuel like CERCER, which is the dispersion of fissile material under CERamic form in an inert CERamic (solid solution or biphasic material) or CERMET which is the dispersion of fissile product under the form of CERamic in METal.

The metal fuel has interesting thermal and mechanical properties. However, a mixed transuranium metal fuel does not seem feasible because of the low melting temperature and the limited mutual solubility. Moreover, the fabrication process requires considerable technological measures due to the pyrophoric nature of some metals and the high volatility of Am and Pu. These type of fuel are discarded.

The Nitride fuels can have a high actinide density (interesting when breeding is the aim), are chemically compatible with water, air and stainless steel as cladding material. Moerover, they have a good thermal conductivity and the actinide nitrides show a mutual miscibility in a wide range of compositions However, the major drawback is the production of ^{14}C through (n,p) reactions on ^{14}N in nitride fuels, that can be prevented only by using nitrogen enriched in the isotope ^{15}N, which raises the cost of the fuel. Moreover, the high volatility of AnN make the fabrication process more difficult.

The Carbide fuel type are considered as the less appropriated. In fact, the highly pyrophoric nature of the carbide compounds requires an inert atmosphere for fabrication. In case of transuranium carbide fuel, a strict control of stoichiometry is required in order to obtain a monocarbide phase.

The oxide fuels are very interesting comparing to the nitrides, carbides or metal alloy, because they are easier to manufacture. The Inert-Matrix Mixed-OXide fuel (IMMOX), which is a solid solution between an inert matrix and the actinides, are particularly under interest [21 - 25].

3.4.3. The inert matrices

A limited number of compounds are considered as a host for the actinide oxides in so-called inert matrix mixed oxide fuel (IMMOX). In fact, the matrix should respect the following criteria: small neutron cross section, limited production of radioactive isotope during irradiation, high fabricability (i.e. ability to fabricate pellets of good quality and properties), good thermal properties (no phase transformation, high melting point, good thermal conductivity), good mechanical properties, compatibility with cladding metals and coolant, stability under irradiation (no amorphisation, no degradation of the thermal conductivity) and good fission probability.

3.4.3.1. The characteristics of the matrices

Different matrices, such as MgO, Y_2O_3, ZrO_2 and CeO_2 present an interest. Their properties are summarized in Table 2 [18].

Table 2. Properties of potential inert matrices [19, 40].

	Cross section (barn)		Melting Point (K)	Thermal conductivity at 1000K ($Wm^{-1}K^{-1}$)	Structure
	Thermal neutrons E=0.025eV	Fast neutrons			
MgO	0.063	< 0.03	3100	10	cubic
Y_2O_3	1.28	< 0.03	2430	/	cubic
ZrO_2	0.185	< 0.03	2980	2	Monoclinic, tetragonal, cubic*
CeO_2	0.63	< 0.03	2870	1.2	cubic

* is a function of the temperature

ZrO_2 material

A large development program is currently performed on stabilised zirconium oxide for plutonium burning in LWRs [41]. The attractive properties of this material are the small neutron capture cross sections of the components, the high melting point, the high radiation stability and the high chemical stability [41- 43].

In fact, ZrO_2 has a high stability of this refractory oxide against amorphization. For instance, no amorphization was observed after irradiation with 400 keV, Xe^+ ions to a dose of 110 displacement per atom at 90°C and after irradiation of ZrO_2 with 240 keV, Xe^+ ions at the room temperature up to about 200 dpa. [43]. Moreover, zirconium oxide is inert to neutron activation and present a good retention of Cs up to 1173 K [44] and an efficient retention of Xe [45]

However, this material change its crystal structure with the temperature from monoclinic to tetragonal at 1170 C to cubic at 2370 °C [46]. Nevertheless, as seen to be in Figure 16 in the case of Y, the addition of aliovalent cations such as Y^{3+} or Ca^{2+} or Mg^{2+}, leads to a partial or complete stabilization of the fluorite lattice in a tetragonal or cubic structure down to the room temperature. The stabilization is assured by the introduction of oxygen vacancies in the material.

Yttria-stabilised (YSZ) as well as calcia-stabilised zirconium oxide (CSZ) are considered because of their cubic structure (face-centered cubic, fluorite type structure). In fact, the structure of the yttria-stabilised zirconium oxide is similar to that of the actinide dioxides, and the solubility of PuO_2 and AmO_2 is therefore high [43].

However, the thermal conductivity of stabilised zirconium oxide is rather low. This will lead to a high central temperature of the fuel and limit the margin to melting. The temperature dependence of the thermal conductivity of zirconia-based inert-matrix fuel was studied by Pouchon [47] who suggested a conductivity value of $1.9\ Wm^{-1}K^{-1}$ for the simulated fuel $(Zr_{0.75}Y_{0.10}Ce_{0.10}Er_{0.05})O_{1.925}$, independent of the temperature, where Ce is used as simulant for Pu.
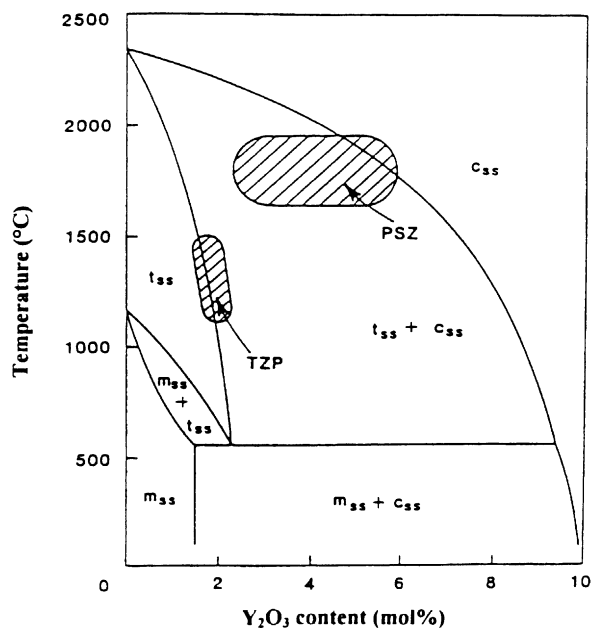
Figure 16. Phase diagram of ZrO₂-Y₂O₃ [46].

<u>ThO₂ material</u>

Although thorium oxide is fertile (it produces [233]U upon irradiation), the production of plutonium and minor actinides in thorium-based fuels or targets is limited. The properties of ThO₂ as a matrix phase are very promising: it has a cubic fcc structure like the other actinide dioxides, it has a high melting point and a thermal conductivity close to that of UO₂ (Table 3). Moreover, ThO₂ is very radiation resistant and allows reaching high burn-up [26].

Table 3. Physical properties of ThO₂ and UO₂.

		ThO₂	UO₂
Structure[a]		fcc	fcc
Melting point/K		3640	3113
Thermal conductivity[b] W m⁻¹ K⁻¹	1273 K	3.0	3.1
	2273 K	1.9	2.7

(a) fcc = face centered cubic – (b) corrected to 100% of the theoretical density

3.4.3.2. The fabrication routes

The current technology for actinide oxide handling is based on powder metallurgy. The actinide oxide powders are homogenised, compacted and sintered to form fuel pellets (Figure 17) [49 - 52]. This technology has been applied on Am-containing materials at laboratory scale. The main drawback of such a process is that some fabrication steps are not easily adaptable to remote handling in shielded cells as is required for Am- and Cm-containing fuels. Furthermore the handling of powders results in the production of

radioactive dust that accumulates in the glove boxes, leading to increasing dose rates of the operators.

Therefore fabrication of such compounds requires a significant simplification of the process and the tools, from the powder synthesis to the clad filling. For example, powder mixing can be avoided by the production of a mixed powder at the reprocessing stage, for example by sol-gel coprecipitation of Pu+MA from the nitrate solution (Figure 17). The sol-gel route has been found suitable for MA fuels in the SUPERFACT experiment [18].

Also the potential of non-pellet fuels, such as (low density) sphere-pac or crushed particles packed by vibration (e.g. the Russian VIPAC process) present an interest as a potential fabrication route for dedicated fuels because compaction and, in some processes, sintering can be avoided [48].

Conventional powder blending	Co-precipitation	Sol-Gel process
Components	Nitrate solution of the matrix and the actinides	Broth preparation
Mixing, Milling	Precipitation by NH_3	Droplets to particles conversion
Cold pressing	Washing, drying	Washing, drying
Sintering	Calcination	Calcination
	Granulation	Cold pressing
	Cold pressing	Sintering
	Sintering	

Figure 17. Different routes for fuel fabrication [49 - 52].

The wet-chemical routes

In order to avoid the milling of powders, which is an unwanted fabrication step because of the dust formation, IMMOX fuels can be prepared by wet chemical routes such as co-precipitation or sol-gel processes.

The principle of the aqueous processes is the conversion of the nitrate solutions containing the elements composing the final product, in good proportion, to oxides, based on the co-precipitation of metal hydroxides by the addition of ammonium hydroxide. In case of co-

precipitation, ammonia is added under strong stirring to obtain a precipitate (powder) that can be used for compaction into pellets (Figure 17). The main drawback of the co-precipitation method is that ultrafine particles undergo severe agglomeration during drying. These powders are very sensitive to the calcination temperature, which increase their crystallinity and lead to harder agglomerates that can strongly influence their sinterability [53, 54].

By sol-gel processes, spherical particles of a mixture of all the components are produced. After washing, drying, and calcination, they can be compacted and sintered, resulting in a dense oxide product (Figure 17).

The co-precipitation route and internal gelation have been shown to be successfully working for Pu-and non-Pu-containing YSZ-fuel [41, 49, 50].

An alternative method for the fabrication of YSZ-based actinide fuels, based on the external gelation method, is being developed at the Institute for Transuranium Elements [51, 55]. In this process the actinides are infiltrated into spherical particles produced by a sol-gel technique. The sphere production can be performed outside the nuclear environment and only the relatively simple infiltration step, which can be automated easily, needs to be performed in the glove box. A schematic representation of the process is given Figure 18. This process has been demonstrated on a laboratory scale with Ce and Pu [56 - 58]. However, the main drawback of this method is the limitation of the MA concentration that can be infiltrated into a porous medium [40].
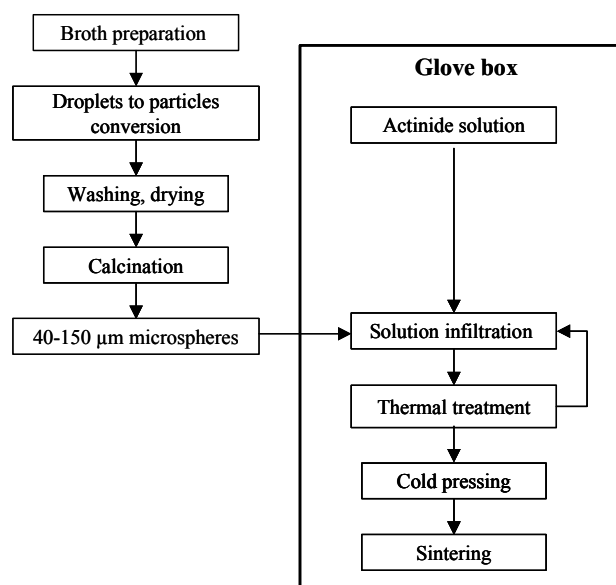
Figure 18. Representation of the infiltration process [51, 58].

The fabrication of thorium oxide pellets, spheres, or coated particles is well known. $(Th,Pu)O_2$ fuels have been produced in the past for the production of HTR fuel [59, 60]. Recently, $(Th,Pu)O_2$ pellet fuels were produced in Europe for irradiation experiments in the frame of the 5th European Framework Programme [26], employing a sol-gel technology. Other fabrication methods such as co-precipitation as oxalate, hydroxide, carbonate or by thermal denitration [61, 62] can be employed. Standard powder blending (comparable to MOX) [63, 64] is also regularly employed. However, it is likely to contain microscopic plutonia-rich domains within a nearly pure thoria matrix. The behaviour of plutonium and its

fission and activation products may then no longer be controlled by the thoria, since they would be concentrated in microscopic domains of very high local burn up [65]. Sol-gel and co-precipitation procedures yielding to a more homogeneous products than powder mixing, that is why, these methods are so more suitable [65].

3.4.3.3.Summary

Inert-matrix mixed oxide fuel has the advantage of relatively simple fabrication and handling. They are not too much different from the current MOX technology when dry processes are used. Like the mixed transuranium oxide fuel, the margin to melting is expected to be small and, in case of zirconium oxide based materials, particularly Yttrium-Stabilized Zirconium (YSZ), matrix being considered as one of the most promising and this in spite of its poor thermal conductivity.

Thorium-based oxide fuel has a good potential of the mixed oxide, although the thorium matrix is not inert. Its fabrication is relatively straightforward and irradiation behaviour is expected to be good from the point of view of thermal and mechanical behaviour.

In order to improve the thermal properties of IMMOX, these materials can be mixed with a matrix which improves the thermal properties. This is the principle of the composite material, such as CERCER and CERMET.

3.4.4. *The composite material*

Composite fuels/targets for actinide transmutation consist of a dispersion of a CERamic phase containing actinides either in an inert CERamic matrix (CERCER) or in a METallic phase (CERMET). A mixed actinide oxide phase is logically candidate as dispersed phase. But also the YSZ-based phase is considered, especially in case of Am-rich fuels.

Of course, in the case of a CERCER composite fuel, the ceramic matrix must fulfil many other criteria such as sufficiently high melting point, good radiation stability, good mechanical properties, compatibility with coolant, etc., and only few materials have been found to be attractive. Magnesium oxide (MgO) is the main candidate for fast reactor applications.

The most interesting metal matrices for CERMET fuel are steel, V, Mo, Cr, Zr or Zircaloy considering the neutronic aspects. To avoid the formation of long-lived technetium neutronic activation of Mo, only ^{92}Mo can be used.

Different fabrication studies have been performed to produce CERCER, mainly based on powder metallurgy, where the powder of the dispersed phase can consist of a fine-grained powder or of spherical particles of the actinide phase [66]. The fabrication of CERMET fuel is also generally done by powder metallurgy [67]. The metal powder is mixed with the ceramic phase, pressed into pellets, preferably by cold compaction, and sintered at high temperature. The problems that have been met in the these fabrication studies are the difficulties to achieve a homogeneous distribution of the dispersed phase. In the case of CERCER a good thermal interface between dispersed phase should be assured and the

protrusion of the dispersed phase avoided. Moreover, in the case of CERMET the risk of an eutectic reaction at temperature lower than 1500°C, between the metal and the fissile oxide component, particularly in the case of Cr and V has to be taken into account [67].

3.4.5. ADS fuel - a preselection during the FUTURE project

The following work was presented by S. Pillon [40], in the International Workshop on P&T and ADS development 2003 in Belgium.

The FUTURE programme (FUels for the transmutation of Trans-URanium Elements) had for objective to study the feasibility of U-free oxide based fuels to be irradiated in ADS.

3 fuel types of oxide fuel have be considered:

1) solid solution such as $(Pu,Am,Cm,Zr)O_{2-x}$ or $(Pu,Am,Cm,Th)O_{2-x}$,

2) CERMET: $(Pu,Am,Cm)O_{2-x}+Mo^{92}$ or W or Cr or V,

3) CERCER: $(Pu,Am,Cm)O_{2-x}+MgO$.

For the different oxide-type fuels a ranking has to be made according to fabricability, safety and performance criteria:

- 1. <u>Margin to melt</u>. High thermal conductivity of composite fuel combined with high melting temperature provides high power to melting and ensures that the fuel will be able to survive a transient overpower accident.

- 2. <u>Fabricability</u> (i.e. ability to fabricate pellets of good quality and properties). That means that the inert matrix volume fraction has to reach a value of at least 50%.

- 3. <u>Coolant void worth</u>. A small cross section for inelastic scatter combined with high thermal conductivity (in order to reduce the core size) ensures that fuel will be able to survive e.g. a loss of flow with coolant boiling or the ingress of gas into the core.

- 4. <u>Reactivity loss and achievable burn-up</u>. The first one should be minimized and the discharge burn-up should achieve a maximum to reduce the recycle number,

- 5. <u>Fission probability</u>. High probability for minor actinide fission minimizes the build-up of curium and maximizes the transmutation rate.

According to these criteria it was concluded that three main candidates deserve further investigation: CERCER with MgO and ZrO_2 and CERMET with ^{92}Mo. CERMET fuels with Cr and W, which show very good safety performance parameters are currently rated lower because of problems with fabrication feasibility (W with its large absorption cross section imposing a reduced upper limit on the inert matrix fraction and Cr and V with the possible eutectic reaction at low temperature [67]).

ZrO_2-fuels are known to exhibit poor thermodynamic and safety performance, mainly due to the low thermal conductivity and the cross sections for inelastic scatter. But ZrO_2 is currently considered to be the conventional preferred choice for which a significant amount of information is known what justify to keep such fuels as potential candidates.

In Table 4 a preliminary ranking of candidate fuels on basis of thermal-physical data, general feasibility and basic safety requirements is suggested. When inert matrices are discarded according to one of the criteria they are cancelled in the corresponding column. Recall of their elimination is then given in the other columns by putting them in brackets.

Table 4. Preliminary ranking of candidate fuels on basis of thermal-physical data, general feasibility and basic safety requirements.

Fabricability	Margin to melt	Coolant void worth	Reactivity loss and BU performance	Fission probability
ZrO$_2$	(W)	(Cr)	(Cr)	(W)
MgO	^{92}Mo	^{92}Mo	^{92}Mo	(Cr)
^{92}**Mo**	(Cr)	(W)	**ZrO$_2$**	^{92}**Mo**
(ThO$_2$)	**MgO**	(V)	(W)	**ZrO$_2$**
~~Cr~~	(V)	**MgO**	**MgO**	**MgO**
~~V~~	(ThO$_2$)	**ZrO$_2$**		
~~W~~	**ZrO$_2$**	~~ThO$_2$~~		

Fuel development studies confirm that TRU-oxide fuels are relatively easy to manufacture, compared to nitride or metal alloys. That is one of their major attractions. Furthermore significant process simplification of oxide manufacturing is still possible. That is a second major advantage when curium will have to be handled [35].

It is important to note that Th matrix do not satisfy the coolant void worth criteria and so can't be used for ADS system. However, it has been demonstrated that this matrix is interesting in the case of Pu burning, particularly in PWR [26].

3.4.6. Advanced ceramics for the conditioning of Pu and MA

Different matrices have been proposed for the immobilisation of Pu and MA in a frame of a conditioning strategy. However, considering a conditioning strategy as an intermediate stage before transmutation facilities become available, the matrices should be able to used as fuel or targets.

Yttrium-Stabilized Zirconium (YSZ), matrix is considered as one of the most promising matrix for the transmutation of the actinides, in spite of its poor thermal conductivity. Moreover, Thorium-based oxide fuel has a good potential of the mixed oxide, and particularly interesting for Pu-burning.

The chemical durability of those matrices were also roughly considered. Thermodynamic calculations showed that zirconia has a very low solubility, inferior than 10^{-10} mol/L with little temperature or flow rate dependence [43]. Leaching studies were performed to estimate the chemical durability of cubic zirconia (9.4 % Y$_2$O$_3$) in a nuclear waste disposal site in granitic rock. The leaching rate in saline ground water at the temperature of 85 °C was 5.8 10^{-4} gm^{-2}d^{-1} [43]. Kuramoto performed leaching experiments on YSZ doped with 10% of

Ce and/or Nd in deionised water at 150 °C for 114 days. The chemical durability was found to be ~10^{-7} - 10^{-8} gm^{-2}d^{-1} [68].

Well-crystallised thorium dioxide is known to be very insoluble in aqueous media [69]. S. Hubert et al. [62] studied the dissolution of crystallised ThO$_2$ and established a normalised dissolution rate of 10^{-6} gm^{-2}d^{-1} at pH = 1.1.

Thus, both matrices, YSZ and ThO$_2$ present a good chemical durability for disposal and they are interesting candidates for the transmutation strategy. Therefore they can also be considered as good potential candidates for the immobilization of Pu and Minor actinides.

4.   Scope of the work

As shown in chapter 3, the advanced treatment of nuclear wastes requires the development of advanced ceramics which can immobilise Pu and MA. Two inert (quasi-inert) oxide matrices, yttrium fully stabilised zirconium oxide (YSZ) and ThO_2, have been foreseen as promising candidates for nuclear applications.

The following work consists in the immobilisation of actinides in $(Zr,Y)O_{2-x}$ and ThO_2 ceramics for nuclear applications using cerium as a simulate from tetravalent actinides. The objective is twofold:

- Evaluate the impact of the addition of cerium on the physical and mechanical properties of the matrices.

- Study of the possibility to fabricate zirconia- and thoria- based ceramics by using simple fabrication processes, adapted to nuclear material.

Whithin this framework, the $(Zr,Y)O_{2-x}$ - CeO_2 and ThO_2 - CeO_2 powders with different ceria contents were synthesised, employing a co-precipitation method of nitrate solutions by NH_3. The powders abbreviated in the following as Ce-YSZ and ThO_2 - CeO_2 of the systems were first characterised by studying the thermal and crystallisation behaviour of the powders as a function of ceria concentration. Then pellets with different ceria contents were fabricated. For each fabrication step, the optimum technological parameters were determined based on the investigation of the powders and pellets properties. The influence of ceria addition on the physical and mechanical properties of the pellets was also studied.

5.   Experimental procedures

5.1. Materials and Apparatus

5.1.1. Applied materials

$ZrOCl_2 \cdot 8H_2O$, $Y(NO_3)_3 \cdot 6H_2O$ and $Ce(NO_3)_3 \cdot 6H_2O$ with a purity of 99.9% were supplied by Alfa Aesar and $Th(NO_3)_4 \cdot 5H_2O$ with an analytical purity by Merck. These salts were used as initial materials for co-precipitation experiment.

Ammonia gas "3.8 wasser frei" from Air Liquide Deutschland GmbH was used as reactant gas for the co-precipitation experiments. Ammonium hydroxide 25% from Fluka chemical was also used for precipitation experiments.

Acetone p.A., concentrated nitric acid 65% extra pure and Oxalic acid were provided from by Merck.

5.1.2. Apparatus-facilities

For performing the experiments and analysis, different apparatus were used.

- Inductive Coupled Plasma Mass spectrometry (ICP-MS), Elan 6100 DRC for the analysis of inactive elements (ng/L until mg/L) in aqueous samples.

- pH meter-691 from Metrohm, 3M KCl, with a pH measurement capacity between 0 and 14, and between 0 and 80 °C.

- Centrifuge Hettich EBA 8S.

- Netzsch STA 449C Jupiter apparatus for thermogravimetry (TG) and differential scanning calorimetry (DSC) investigations. The powder sample is placed in a platinum plate and is heated with a chosen heating rate in a chosen atmosphere until 1400°C. The mass and the calorimetry of the system is measured continuously.

- Stoe Transmissions-Diffraktometer-System STADI, (CoK_α, $\lambda=0.178897$ nm for Zr-based materials or Cu, $\lambda=0.154060$ nm for Th-based materials) for X-Ray Diffraction analysis.

- Dilatometer furnace Netzsch DIL 402C measures the shrinkage of the pellet until 1600°C in different atmospheres and heating rate up to 5K/min.

- Optical microscope coupled with a particle size determination program based on photography analysis (ZEISS KS300). Reliability of measurement until 2 µm.

- Anton Paar MHT 10 Vickers indenter, which can apply a load up to 4 N, connected to the optical microscope

- Scanning electron Microscope (SEM) (JEOL JSM-840) coupled with a energy dispersive X-Ray analyser (EDX).

- Laser Granulometer Quantachrom- Cilas 920. With a resolution located between 0.3 and 100 μm

- Mortar grinder KM100 from Retzsch, for a dried or wet grinding by attrition of powder up to 1 μm.

- Drying oven T12 Heraeus Instrument with heating capacity from room temperature up to 250°C.

- Calcination Oven M110 from Heraeus Service, with a maximum temperature of 1100°C.

- High temperature furnace Linn HT 1800, with M. Molybden heating elements and a maximum temperature of 1750°C.

- X-Ray photoelectron spectroscopy (XPS) Spektrometer Physical Electronics 5600, was used to determine the oxidation state of elements in the final material

5.2. Fabrication of powders and pellets

Different synthesis routes were used for the pellets fabrication, (Figure 19). The route 1 and 2 were employed for zirconia and thoria based ceramics respectively. The parameters of the steps marked by an asterix were optimised.

Route 1	Route 2
Co-precipitation of nitrate solution in NH_3	Co-precipitation of nitrate solution in NH_3
Washing in water	Washing in water
Drying in air at 110°C	Drying in air at 110°C
Calcination in air at T_C*	Calcination in air at 400°C
Grinding by attrition in acetone*	Pressing by repressing $P = 640 - 900$ MPa*
Fractionation in acetone*	Sintering in air at 1600°C for 5 hours
Uniaxial cold pressing $P = 100\text{-}1200$ MPa*	
Sintering in air at 1600°C for 5 hours	

Figure 19. Two investigated routes for fabrication of zirconia and thoria based ceramics.

5.2.1. Synthesis of the powders

$(Zr,Y)O_{2-x}$ - CeO_2 powders (Ce-YSZ) with ceria contents of 0, 5, 10, 15, 20, 25, 30, 35, 40, 50, 60 and 80°wt.% were synthesised by the co-precipitation method. In all cases, the concentration of $YO_{1.5}$ in the YSZ system remains constant at 16 mol %. The exact composition of the Ce-YSZ powders are summarized in

Table 5.

Table 5. Compositions of Ce-YSZ powders

Name	Wt.% of CeO_2	Mol% of ZrO_2	Mol% of $YO_{1.5}$	Mol% of CeO_2	Composition of O*	Theoretical extended formula
YSZ	0	84.00	16.00	0.00	1.92	$(Zr_{0.84}Y_{0.16})O_{1.92}$
5-Ce-YSZ	5	80.84	15.40	3.76	1.92	$(Zr_{0.81}Y_{0.15}Ce_{0.04})O_{1.92}$
10-Ce-YSZ	10	77.60	14.78	7.62	1.93	$(Zr_{0.77}Y_{0.15}Ce_{0.08})O_{1.93}$
15-Ce-YSZ	15	74.27	14.15	11.59	1.93	$(Zr_{0.74}Y_{0.14}Ce_{0.12})O_{1.93}$
20-Ce-YSZ	20	70.85	13.49	15.66	1.93	$(Zr_{0.71}Y_{0.13}Ce_{0.16})O_{1.93}$
25-Ce-YSZ	25	67.33	12.83	19.84	1.94	$(Zr_{0.67}Y_{0.13}Ce_{0.20})O_{1.94}$
30-Ce-YSZ	30	64.48	12.28	23.23	1.94	$(Zr_{0.65}Y_{0.12}Ce_{0.23})O_{1.94}$
35-Ce-YSZ	35	60.86	11.59	27.55	1.94	$(Zr_{0.61}Y_{0.11}Ce_{0.28})O_{1.94}$
40-Ce-YSZ	40	56.23	10.71	33.06	1.95	$(Zr_{0.56}Y_{0.11}Ce_{0.33})O_{1.95}$
50-Ce-YSZ	50	49.23	9.38	41.39	1.95	$(Zr_{0.49}Y_{0.09}Ce_{0.42})O_{1.95}$
60-Ce-YSZ	60	40.79	7.77	51.44	1.96	$(Zr_{0.41}Y_{0.08}Ce_{0.51})O_{1.96}$
80-Ce-YSZ	80	21.96	4.18	73.86	1.98	$(Zr_{0.22}Y_{0.04}Ce_{0.74})O_{1.98}$
CeO_2	100	0.00	0.00	100.00	2.00	CeO_2

* theoretical composition calculated, considering that only Ce(IV) is present in the material.

ThO_2 - CeO_2 powders containing 0, 5, 10, 15, 20, 25, 50 and 75 mol% of ceria were also synthesised by the co-precipitation method.

In both cases, the required quantity of the salts was dissolved in deionised water at room temperature, reaching concentration of ~10^{-2}molL^{-1}. For the co-precipitation ammonia gas was added on stirring, for 30 min, to the surface of the solution, in order to ensure an homogeneous reaction.

5.2.2. Washing of the powders

Precipitates were separated and carefully washed by deionised water until ammonium, nitrate and chloride were eliminated. The precipitates were first filtrated and washed on Büchner system with 2- 3 litres of water, and then further stirred in distilled water for at least 12 hours. The water of the system was changed regularly, until the pH of the solution become neutral. At the end of the precipitation the powder should have a yellow colour, which is characteristic for Ce^{+4}. The prolonged aging during stirring is essential for the full oxidation of Ce^{+3} ion [70].

The washing step should be done carefully. In fact in the solution remains some ammonium nitrate and chlorides. These rests of ammonium chloride can be decomposed by sublimation at 335°C releasing NH_3, HCl, Cl_2 gases [71].

Ammonium nitrate is an oxidising compound and will decompose under NH_3 and NOx gases. The decomposition,based on oxidation of the elements which is usually rapid and irreversible, is complex and takes place at different temperatures. That's why ammonium nitrate is usually used as explosive product. A first type of decomposition takes place at 170-180°C releasing ammonium and nitric acid. A second type of decomposition can appear between 210-260°C involving the formation of N_2O and water. Finally, at 300°C a rapid and violent decomposition occurs forming N_2, O_2, H_2O, often responsible for explosion. Moreover, if there are some chloride in the solution, ammonium nitrate can decompose even at less than 100°C to form N_2O and H_2O. Some products like NO, Cl_2, $NOCl_2$ can also be formed [72, 73].

Thus, the impurities in the powder can violently react either by oxidation, by decomposition, by interaction with the other elements or by a strong heating. Theses reactions can be explosive and are responsible of the releasing of gases, which have to escape from the matrix. So, to avoid the formation of cracks in the sintered body due to the decomposition of elements, this impurities should be eliminated and a strong heating rate should be avoided in the range of temperatures from 25 to 350°C.

5.2.3. Drying and calcination of the powders

After washing, the powders were dried in an oven at 110 °C for 24 hours. Afterwards the powders were eventually calcined in air at different temperatures. Zirconia based powders were calcined at 350, 500, 600, 800, 950, 1400 and 1600 °C for 2 hours. Thoria based powders were calcined at 400°C for 5 hours.

5.2.4. Grinding of the powders

After calcination, the powders were then ground by attrition for 2 hours in acetone to prevent dust formation. Previous studies had demonstrated that, acetone is the most adapted solvent, in comparison to water and propanol [74].

5.2.5. Fractionation of the powders

In the case of zirconia ceramics, the powder were then eventually fractionated in acetone, following the Stock's equation [75].

For particles of diameter d (m) and with a density ρ (kgm^{-3}), in a solvent of density ρ_s (kgm^{-3}) and viscosity μ (mPas), the time t (s) for these particles to fall down of a height H (m) can be determined by the following expression [75]:

$$t = 18\mu \cdot H / (d^2 \cdot g\,(\rho - \rho_s)) \qquad\qquad (1)$$

where g is the universal gravity constant (ms^{-2}).

According to this expression, by choosing an appropriate solvent, the height and the proper time t, particles with specific size can be separated. Acetone, which has a viscosity of 0.32 mPas at 32°C [76] and a density of 0.7908 gcm^{-3} [76] has been so chosen as grinding and fractionation solvent.

Thus, considering that agglomerates are dense material with a density equal to the theoretical density, and considering a height of decantation of 3 cm, after 3 min 30 s, agglomerates with an equivalent diameter less than 4 μm remains in suspension.

Thus, to fractionate the powders, the following procedure was applied. First, the powder, ground in the solvent, was poured in one recipe, which was filled with solvent until a height of about 4 cm is reached. After stirring of the mixture in an ultrasonic bath for 5 min, the decantation process can occurs during 3 min 30s. Then, 3 cm of solvent containing the particles are extracted from the recipe by a siphon principle. The powder, which stays at the bottom is ground again and the process is reproduced.

After recovery of the agglomerates in solvent, the mixture containing the solvent and the agglomerates less than 4 μm, is first dried in oven at 80°C for 12 hours and then at 110°C for 12 hours. Powders can then be used for pelletization.

5.2.6. Powders compaction

The powders (approximately 0.5g) were compacted into cylindrical pellets of 10 mm diameter either by cold uniaxial pressing or by repressing. Zinc-sterate dissolved in diethylether was used as lubricant. The range of pressures used in this work varied from 100 to 1200 MPa.

In the case of repressing, the powders were first compacted, then granulated and re-compacted.

5.2.7. Sintering of the pellets

The pellets were then sintered at 1600°C for 5 hours in air atmosphere in an electric resistive furnace. The pellets were first heated from room temperature to 400°C in 6 hours to avoid a thermal shock and violent elimination of impurities susceptible to create cracks in the pellets. After having been hold at 400°C for 3 hours, the temperature increases then up to 1600°C during 14 hours and remains constant for 5 hours. Then it decreases slowly to room temperature (6 h) to avoid thermal stresses.

5.3. Characterisation methods for the powders and pellets

The characteristics of powders and pellets were investigated for each step of the fabrication.

5.3.1. Thermal behaviour of the powders

The thermal behaviour of the powders during heating from room temperature to 1300 °C was investigated by thermogravimetry (TG) and differential scanning calorimetry (DSC) in air or in nitrogen with a heating rate of 10 K/min.

5.3.2. Crystal properties of the materials

The crystal structure of the powders and sintered pellets was investigated by X-ray diffraction. Lattice parameters, relative crystallinity degree, crystallite size and lattice distortions were determined.

5.3.2.1. Lattice parameter

The lattice parameter was determined using the Nelson-Riley method [77]. This method will be described in the specific case of a cubic structure, characterised by a lattice parameter a. The first step consists in the determination of the Miller Indices $(h_i k_i l_i)$ associated to each diffraction peak i characterized by a diffraction angle θ_i. For each peak, the value $\sin^2(\theta_i)$ is proportional to the addition of the square of each miller indice $m = h_i^2 + k_i^2 + l_i^2$.

Thus,

$$(h_1^2 + k_1^2 + l_1^2) \cdot \sin^2(\theta_i) / \sin^2(\theta_1) = (h_i^2 + k_i^2 + l_i^2) \qquad (2)$$

where θ_1 is the diffraction angle of the first peak indexed by the Miller indices $(h_1 k_1 l_1)$.

In the case of a fluorite structure, the first diffraction peak correspond to the plan (111) [78] such as the value $3 \sin^2(\theta_i)/\sin^2(\theta_1)$, where θ_1 is the diffraction angle of the first peak, equal to $m = h_i^2 + k_i^2 + l_i^2$. From this peak indexation, the lattice parameter a, of a cubic structure, can be determined stating that the distance between two plans of the family (hkl) d_{hkl}, is given by the relation:

$$d_{hkl} = \lambda / 2 \cdot \sin(\theta) = a / \sqrt{h^2 + k^2 + l^2} \qquad (3)$$

So, for each peak with miller indices of (hkl):

$$a = \lambda \cdot \sqrt{h^2 + k^2 + l^2} / 2 \cdot \sin(\theta) \qquad (3)$$

Thus, the lattice parameter was determined for each peak and the average value was calculated. The correction of the zero position was determined for each spectra.

5.3.2.2. Relative crystallinity degree

The relative crystallinity degree (G, %) was calculated for all powders by using the following formula [79].

56

$$G = 100 \cdot (I/I_o)/(I_s/I_{os}) \tag{5}$$

where I represents the intensity of the (111) XRD peak of the investigated powders and I_o its background signal. I_s and I_{os}, respectively, represent the intensity of the (111) XRD peak and the background signal of the same powder calcined at high temperature (1400 or 1600°C).

5.3.2.3. Crystallite size (L) and the lattice distortions

The values of the mean crystallite size (L) and the lattice distortions ($<\varepsilon^2>^{0.5}$) were determined from XRD measurements by using the Hall-Williamson method [80]:

$$B \cdot \cos(\theta) = \lambda/L + 4 \cdot <\varepsilon^2>^{0.5} \sin(\theta) \tag{6}$$

where θ is the Bragg angle of diffraction, λ is the wavelenght of incident X-Rays and B is the peak half-width corrected to instrumental widening.

For each diffraction peak, the angle θ and the half-width were determined and the values $B \cos(\theta)$ were plotted as a function of $\sin(\theta)$, following a linear dependence. From the value of the intercept point and the slope, L and $<\varepsilon^2>^{0.5}$ were calculated.

The apparent crystallite size of amorphous powders was determined by using the Scherrer formula applied on the diffraction plan <111> [81]:

$$L = K \cdot \lambda / B \cdot \cos(\theta) \tag{7}$$

In this formula K represents a shape factor and is equal to 0.9.

5.3.3. Morphological structure of the powders

The peculiarities of the morphological structure of particles were investigated by optical microscope and SEM. Particles size distribution was obtained by optical microscopy pictures analyser and by laser granulometry.

5.3.4. Green, sintered and theoretical densities

The green densities (ρ_G) of the pressed pellets were determined by the geometrical method. The mass m of the sample, its diameter D and its height h were measured and the density was calculated according to:

$$\rho_G = 4m/(\pi D^2 h) \tag{8}$$

The sintered densities (ρ_S) of the pellets were determined by hydrostatic weighing in water. After having measured the mass of pellet (m), it is coated by paraffin. The mass of the sample coated by paraffin m_p is determined. The sample is then sunk in water and its mass determined in water m_w. The density is calculated following the formula, where density of water d_w equal 0.9982 and the density of paraffin d_p=0.9

$$\rho_S = m \, d_p \, d_w / [d_p \, (m_p - m_w) - d_w \, (m_p - m)] \tag{9}$$

The theoretical densities of the materials (ρ_T) were calculated from the lattice type and parameter [82]. Thus, assuming that the elements form a solid solution the theoretical density of the material can be so calculated:

$$\rho_T = M_{system}N \, / \, (V \, N_a) \tag{10}$$

where M_{system} is the atomic weight of the system, N the number of atoms per unit cell, V the volume of the lattice and N_a the Avogadro constant. Thus, in the case of a $(Th_{1-x}Ce_x)O_2$ solid solution, crystallising in a face centred cubic, fluorite type structure, with a lattice parameter a, the theoretical density will be so estimated as :

$$\rho_T = 4[(1-x) \, M_{Th} + xM_{Ce} + 2M_O] \, / \, a^3 N_a \tag{11}$$

5.3.5. Densification behaviour of the pellets

The sintering behaviour of the pellets was studied by dilatometry. After compaction, the pellets were heated from room temperature to 1600°C, with a heating rate of 3K/min. The relative density (ρ/ρ_T) of pellets and the densification rate ($d((\rho/\rho_T)/dT)$) were computed from the experimental linear shrinkage (dl) [83] with an additional mass loss correction according to the following equations.

The initial and final height (l_0 and l_F) as well as the initial and diameter (D_0 and D_F) of the pellets are known. Stating that the pellet shrink isotropically it can be established that :

$$l = l_0 + dl \tag{12}$$

$$D = D_0 + dl \, (D_F-D_0)/(l_F-l_0) \tag{13}$$

The mass of the sample at the temperature T (m_T) can be determined as following:

$$m_T = m_0 - (TG_T/TG_F)\cdot(m_0 - m_F) \tag{14}$$

where m_0 is the mass initial mass and m_F the final mass of the body, TG_T and TG_F the mass loss (%) at the temperature T and at final, given from the TG experiments, performed on powder.

According to the fact that

$$\rho = 4m/(\pi \, D^2 l) \tag{15}$$

the relative density (ρ/ρ_T) of pellets and the densification rate ($d((\rho/\rho_T)/dT$) were computed.

5.3.6. Pellets microstructure and Ce distribution

Sintered pellets were carefully polished for further investigations of the microstructure. For SEM investigations the samples were thermally etched in air at 1500 °C for 1 hour and then their morphology was analysed. The chemical composition of the pellet was investigated by EDX.

5.3.7. Mechanical properties of the pellets

The microhardness (H_V) of sintered samples was measured by a diamond Vickers indenter (Anton Paar MHT 10) applying a load (F). The microhardness (H_V, GPa) was calculated by the following expression [84]:

$$H_V = 1852 \ F/d^2 \tag{16}$$

where F (N) represents the load and d (μm) the average length of the diagonals of the Vickers indents.

The fracture toughness K_{IC} (MPa·m$^{0.5}$) were estimated by the indentation crack length method, using the Niharas expression in the case of zirconia based ceramics [84]:

$$K_{IC} = 0.018 \ H_V \ (d/2)^{0.5} \ (E/H_V)^{0.4} \ (2c/d - 1)^{-0.5} \tag{17}$$

and the Antis expression in the case of thoria based ceramics [84]:

$$K_{IC} = 0.032 \ H_V \ (d/2)^{0.5} \ (E/H_V)^{0.5} \ (2c/d)^{-1.5} \tag{18}$$

where c (μm) represents the average length of cracks and E (GPa), the Young modulus.

The Young modulus (E) was estimated as a function of the ceria content C_{Ce} (%) and the relative porosity of ceramics P (%).

$$E = E^{\circ}_{Ce} \ (1 - 2.9 \ P) \tag{19}$$

where E°_{Ce} is the Young modulus of a dense ceramic with a concentration of cerium C_{Ce}. The factor 2.9 and the relation (19) were taken from the literature [85].

The value E°_{Ce} was estimated for each ceria content by a linear dependence between E°_{matrix} and E°_{CeO2} :

$$E^{\circ}_{Ce} = C_{Ce} \ (E^{\circ}_{CeO2} - E^{\circ}_{matrix})/100 + E^{\circ}_{matrix} \tag{20}$$

with E°_{ZrYOx} = 233 GPa [86], E°_{CeO2} = 165 GPa [87] and E°_{ThO2} = 249 GPa [88].

5.3.8. Oxidation degree of Ce in the pellets

The oxidation degree of Ce in the zirconia based ceramics was determined by XPS.

6. Kinetics of the precipitation of Ce-YSZ and ThO$_2$-CeO$_2$

The kinetic of the hydrolysis of the Zr, Y, Ce and Th was investigated. First the hydrolysis of Zr, Y and Ce with the aid of ammonium hydroxide was studied in order to determine the completeness of precipitation as a function of HNO$_3$ and initial element concentration.

Then, the co-precipitation of Zr, Y, Ce and Th, Ce using ammonia gas, was investigated, in order to define the mode of precipitation and to determine the possibility of synthesising powders for ceramics preparation. In this frame 15-Ce-YSZ and ThO$_2$-50 CeO$_2$ powders were chosen as representative system.

6.1. Hydrolysis of Zr, Y and Ce

ZrOCl$_2$·8H$_2$O, Y(NO$_3$)$_3$·6H$_2$O and Ce(NO$_3$)$_3$·6H$_2$O with variable concentration (10^{-3} to 1 molL^{-1}) were dissolved in 5 ml nitric acid (0.1 - 1molL^{-1}). The required quantity of NH$_4$OH necessary to precipitate the elements (Zr, Y or Ce) and neutralise the nitric acid was then added to the solution. Following this, the solution was allowed to stand for three hours and was centrifuged for five minutes with a speed of 5000U/min. A sample was then drawn from the supernatant solution through a 200 nm filter and analysed with the aid of ICP-MS.

The results in Figure 20 show that the precipitations are > 99.6 % under nearly all conditions. The nitric acid concentration has no influence. Major scatter in the measurement results is only observed at element concentrations of 10^{-3} molL^{-1}, where the precipitation ratio are between 99.6 and 99.9 %.
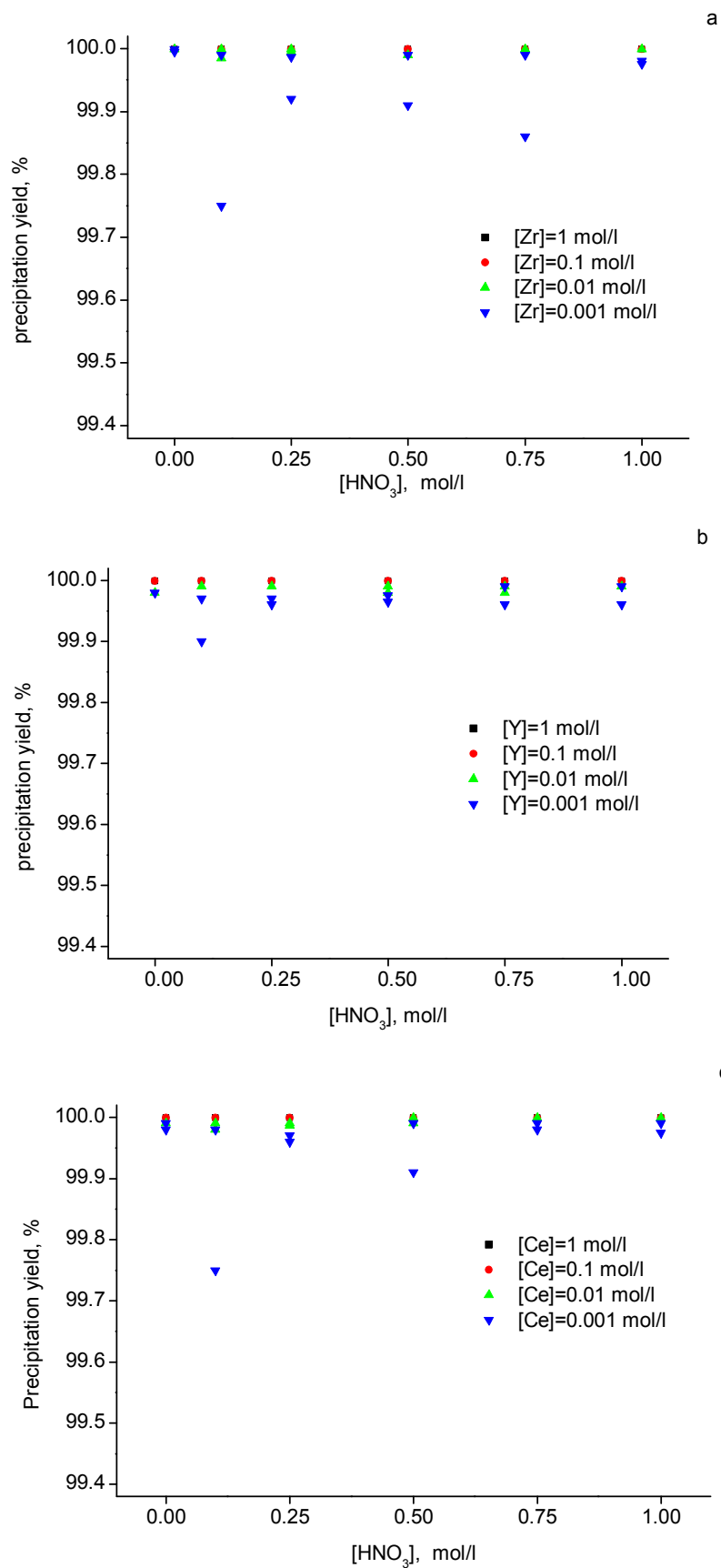
Figure 20. Precipitation yields of Zirconium (a), Yttrium (b) and Cerium (c) as a function of the initial HNO₃ concentration and as a function of the initial element concentration.

6.2. Co-precipitation of Ce-YSZ

The precipitation investigation was performed with the 15-Ce-YSZ powders. In both cases, the required quantity of salts were dissolved in 2.5 L of distilled water at room temperature. The initial concentration of elements is reported in Table 6.

Table 6. Initial concentration of elements in solution before precipitation.

	[Zr] (mmol/L)	[Y] (mmol/L)	[Ce] (mmol/L)	[Th] (mmol/L)
15-Ce-YSZ	25	5	4	/
ThO_2–50 CeO_2	/	/	15	15

NH_3 gas was added to the solution for 15 min while stirring. Each 30 seconds, 5 ml of the solution were extracted. The samples were then centrifuged to separate the solid and liquid phase and the pH of the solution was measured at room temperature. The liquid phase was then filtered through a 200 nm pores filter and samples were then analysed by ICP-MS in order to determine the elements present in the solution.

The pH, initially 1.7, increases with the addition of NH_3 up to 9, the value measured at the end of reaction (Figure 21a). After 6 minutes of reaction, the pH has reached a value of 3. Then, a first steep increase of pH up to 4.6 takes place. A second steep increase of pH from 6.8 up to 8, is measured after 10.5 min of reaction. In between, two small pH increase are observed between 7.5 and 8 min, and between 8.5 and 9 min.

Simultaneously, the concentration of non precipitated elements in the solution was determined. Until 6.5 min of reaction, the concentration of all elements Zr, Y and Ce remains constant. Starting from this point the concentration of all element decreases. After 7 min of reaction, no Zr is detected in the solution. The first steep increase of pH is so connected to the precipitation of Zr.

Y start to precipitate after 6.5 min at pH ~ 4, continuously until 11 min, time after which the concentration of Y is negligible. The derivative of the Y concentration with the time of reaction has a maximum at 8.4 min (Figure 21b).

The concentration of Ce decreases from 6.5 to 12.5 min. In fact, the derivative of the cerium concentration with he time of reaction was plotted as a function of the time (Figure 21b). The curve can be decomposed in two Gaussian, one centered 8.1 min with a half width of 0.7, and the second centered on 10.2 min with a half width of 0.8. Actually, the cerium is present in solution under the dominant oxidation degree (III). However, with the contact of O_2 it can be partially oxidised to Ce(IV) [89]. Both species are so present in the solution. The pK_S of Ce(IV) is higher than the pK_S of Ce(III). This indicates that the Ce(IV) should precipitate at lower pH [90]. The first Gaussian corresponds to the precipitation of Ce(IV) while the second to the precipitation of Ce(III). Thus, the small increase of pH observed between 7.5 and 8 min can be connected to the precipitation of Ce(IV) while the last increase of pH noticed between 10.5 and 11.5 min is connected to the precipitation of Ce(III).

According to its pKs [91], Y is supposed to precipitate between Ce(IV) and Ce(III). In reality, Y precipitates at the same time as Ce(IV). Thus, the co-precipitation of Zr and Ce would favour the precipitation of Y. The final precipitation yields are higher than 99.9%.
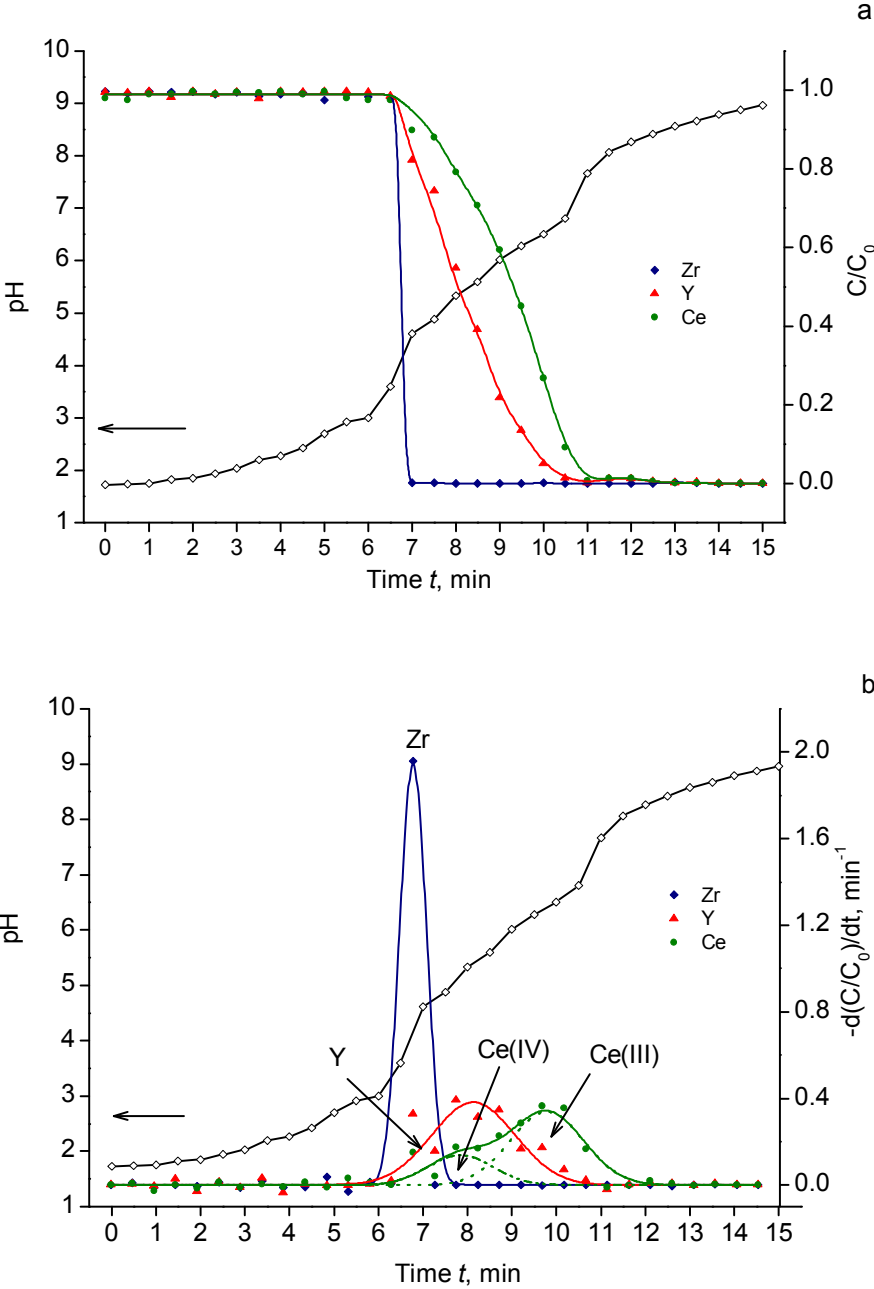
Figure 21. Kinetics of the co-precipitation of 15-Ce-YSZ powder.

6.3. Co-precipitation of ThO$_2$ - CeO$_2$

The kinetics of ThO$_2$ −50 CeO$_2$ precipitation was also studied in details following the same procedure described in chapter 6.2. The initial concentration of elements are reported in Table 6.

The pH, initially 3, first slowly increases with the addition of NH$_3$ (Figure 22a). After 6 minutes of reaction, the pH, which has reached a value of 4, steeply increases up to 5.3 and then remains constant for 1 minute. At the same moment, the concentration of Th, present under the stable oxidation state (IV) steeply decreases and after 7.5 minutes of reaction, no thorium is detected in solution (Figure 22a).

After 8 minutes of reaction, the pH increase up to 5.5 and then remains constant until 10 minutes of reaction. After 11.5 min, the pH has reached a value of 6.6, remains constant over an interval of 2 minutes and then increases continuously up to 9, the pH measured at the end of the reaction.

Simultaneously, during all this interval of time (from 8 to 14 min), the concentration of cerium in solution quite continuously decreases (Figure 22a). Cerium is present in solution under the oxidation degree (III) or (IV). Moreover, the derivative with time of the ceria concentration in solution, can also be divided in 2 Gaussians (Figure 22b): One related to the precipitation of Ce(IV) and one to the precipitation of Ce(III). Thus, the increase of pH from 5.3 to 5.5 followed by a plateau can so be correlated to the precipitation of Ce(IV), while the increase of pH from 5.5 to 6.6 followed also by a plateau, can be correlated with the precipitation of Ce(III).

It is important to notice that the interval of co-precipitation of both elements Th and Ce is quasi non-existent. The final precipitation yields are superior than 99.9%.
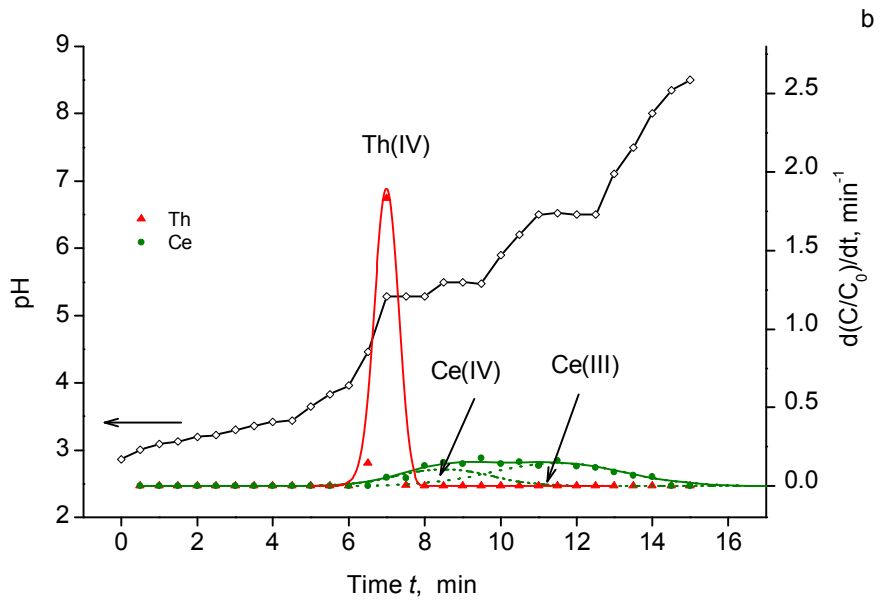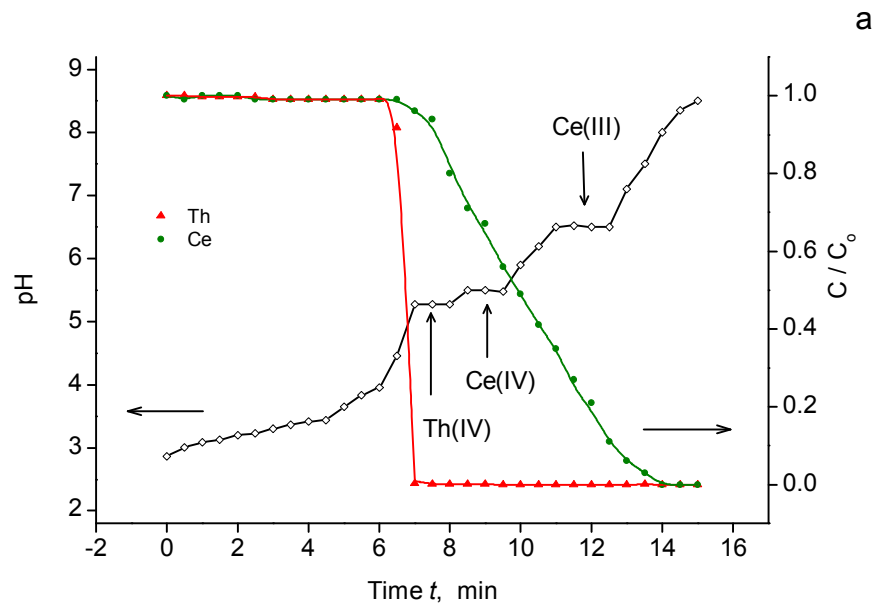
Figure 22. Kinetics of the co-precipitation of ThO$_2$ - 50 CeO$_2$.

7.   Yttria fully stabilised zirconia: inert matrix for the immobilisation of actinides

7.1. Introduction

YSZ was chosen as inert matrix in order to immobilise tetravalent actinides, simulated in the present study by CeO_2. In order to estimate the impact of the CeO_2 addition on the properties of the matrix and to test the possibility of pellets fabrication with simple fabrication processes, Ce-YSZ powders were synthesised by the co-precipitation method of nitrate solution by NH_3. Their thermal and crystallisation behaviour were first investigated. Then powders were compacted into pellets and sintered. Their compressibility and sinterability were studied in details.

7.2. Physical properties of Ce-YSZ powders

In order to characterise the system, the thermal and crystallisation behaviour of the $(Zr,Y)O_{2-x}$ - CeO_2 system, was first investigated as a function of the ceria concentration, using TG-DSC and XRD.

7.2.1.   The thermal behaviour of Ce-YSZ powders

After drying, all powders were investigated by thermal analysis (TG-DSC). Yttria stabilised zirconia (YSZ) and pure ceria powders were first investigated as reference samples.

As shown on Figure 23a, YSZ powder shows a significant mass loss (12.57 %) from 25 to 600 °C. From 25 to 380 °C, the mass loss is accompanied by a heat consumption, which corresponds to the elimination of adsorbed and crystal water and impurities. At 455 °C a sharp exothermic effect with a specific heat of 111.3 J/g was detected. This effect certainly corresponds to the material crystallisation [92]. At temperatures higher than 600 °C, no thermal effects were detected. During heating from 600 to 1235 °C the mass of the sample still decreases but the mass loss is negligible (0.86 %). This can be associated with the elimination of remained OH-groups from the material [93]. After annealing at temperatures higher than 1235 °C (T_S), the mass remains constant. In the following, this temperature (T_S) will be named as formation temperature of the final solid solution.
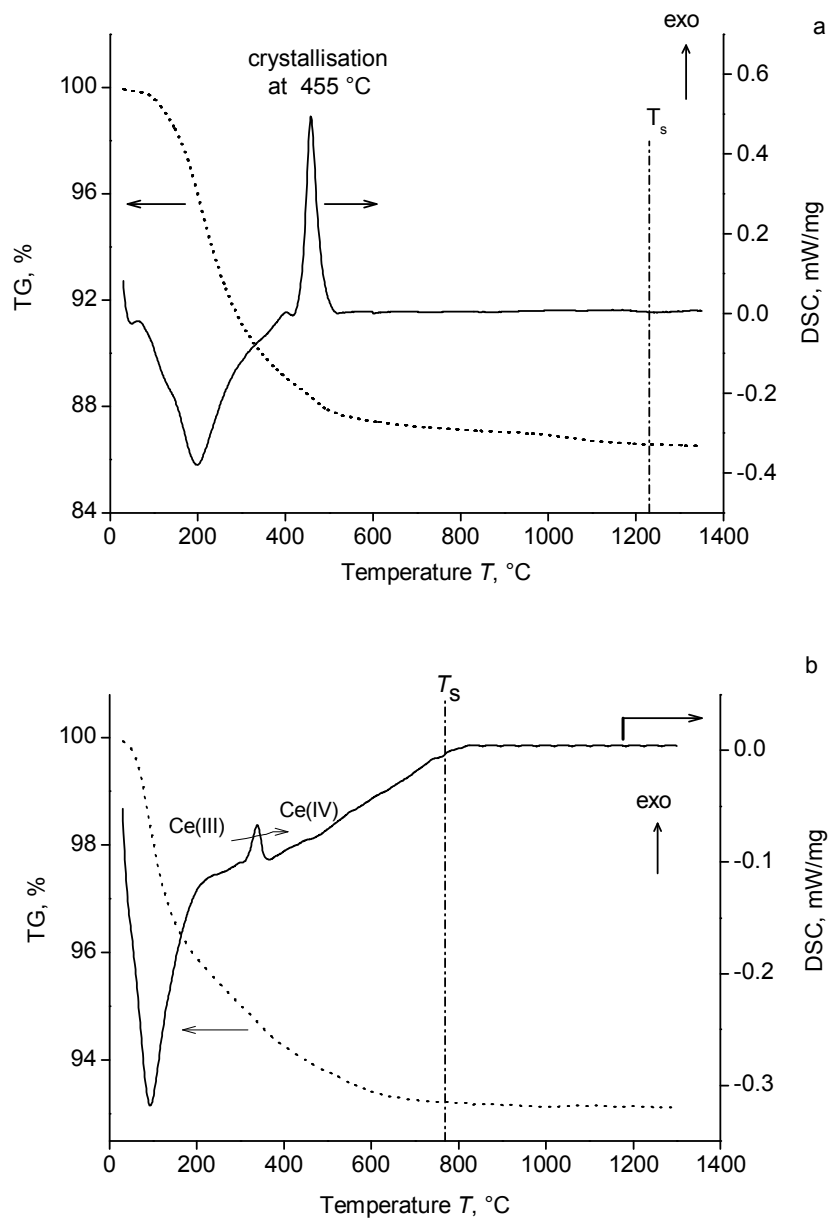
Figure 23. TG (dot) and DSC (full) curves of YSZ (a) and CeO₂ (b) powder in air atmosphere.

In the case of pure ceria powder (Figure 23b), a significant mass loss (5.05%) was also measured during heating from 25 to 300°C, accompanied by a heat consumption, which also corresponds to the elimination of adsorbed water and impurities. Between 310 and 360 °C, a small exothermic effect with a maximum at 340 °C and a specific heat of 4.6 J/g was observed. This effect disappears when ceria is heated in nitrogen atmosphere. So, the peak observed in air atmosphere is related to the oxidation of Ce(III) to Ce(IV) during annealing [94]. However, the mass loss in this temperature region is similar in both atmospheres (0.41 and 0.42% in air and nitrogen respectively), allowing to conclude that only a small amount of Ce(III) is present in the synthesised powder. In the temperature range from 360 to 772 °C, the DSC curve does not show clear thermal effect, but is accompanied by a mass loss of 1.68 %, which corresponds to the elimination of the OH-groups from the

68

material [93]. At temperatures higher than T_S equal to 772 °C, no additional thermal effects were detected (Figure 23 c,d) and the mass of sample remains constant.

For all ceria concentrations, the mass of powder decreases until T_S and then remains constant. However, the values of this characteristic temperature T_S strongly depend on the ceria concentration, as shown in Table 7. For ceria contents from 0 to 20 wt.%, T_S is constant and is approximately 1230 ± 10 °C. Between 25 to 30 wt.% of ceria, the value of T_S steeply decreases from 1180 to 820 °C then slightly decreases down to 775°C until 40 wt.% and then remains constant up to pure ceria.

Table 7. Influence of the ceria addition on the formation temperature of the solid solution T_S.

CeO$_2$, wt.%	0	5	10	15	20	25	30	35	40	50	60	80	100
T_S, °C	1235	1240	1240	1220	1225	1177	820	792	773	786	778	781	772

For all ceria contents, the DSC curves show a large endothermic peak between 25 and 350°C and no thermal effect after 700°C. Only in the temperature range from 310 to 700°C, powders have different thermal behaviours depending on the ceria concentration.

For ceria content from 5 to 20 wt.%, the DSC curves show two exothermic peaks (Figure 24), which remain when the powder is heated in nitrogen (control experiment). The total heat Q of these thermo-effects decreases drastically from 120.2 to 10.1 J/g with increasing of ceria from 0 to 20 wt. %, as listed in Table 9.

For concentrations of ceria higher than 25 wt.%., a small exothermic effect was observed between 310 and 350°C due to the residual presence of Ce(III) in the powder. For this range of concentration, no particular effect was seen on the DSC curves, even if the mass of the sample still decreases, like in the case of pure ceria (Figure 23b).

Table 8. Description of the characteristics temperatures of the TG-DSC spectra.

T_I^R	YSZ	Temperature at the beginning of the exothermic effect
T_M^R	YSZ	Temperature at the maximum of the exothermic effect
T_F^R	YSZ	Temperature at the end of the exothermic effect
T_I	10-Ce-YSZ	Temperature at the beginning of the exothermic effects
T_{M1}	10-Ce-YSZ	Temperature at the maximum of the first exothermic effect
T_{F1}	10-Ce-YSZ	Temperature at the end of the first exothermic effect
T_{I2}	10-Ce-YSZ	Temperature at the beginning of the second exothermic effect
T_{M2}	10-Ce-YSZ	Temperature at the maximum of the second exothermic effect
T_F	10-Ce-YSZ	Temperature at the end of the exothermic effects
T_S	YSZ / 10-Ce-YSZ	Formation temperature of the final solid solution
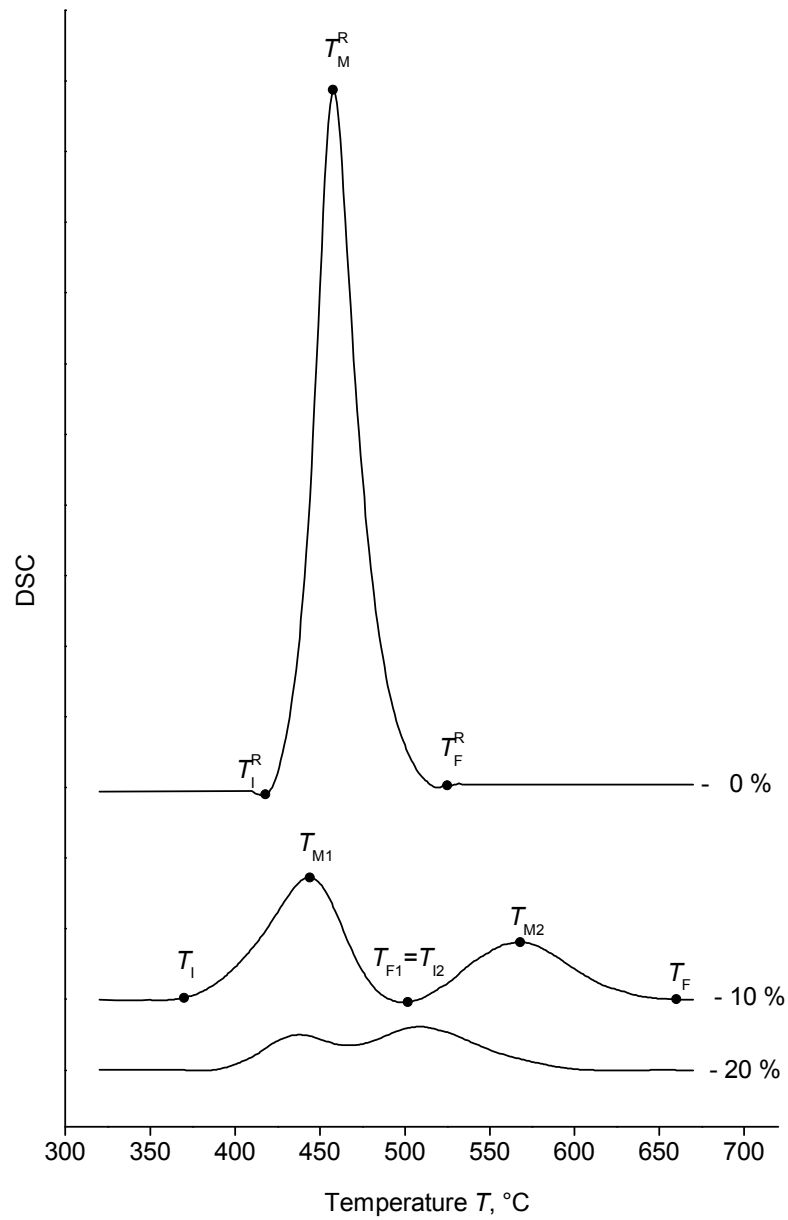
Figure 24. DSC curves of YSZ and Ce-YSZ powders with 10 and 20 wt. % ceria in temperature regions from 300 to 700 °C.

Table 9. Characteristics data of the exothermic effect observed on the DSC curves between 300 and 700 °C for Ce-YSZ powders with ceria concentration between 0 and 20 wt.%.

CeO$_2$, wt.%	T_{M1}, °C	T_{M2}, °C	Q$_1$/Q, %	Q$_2$/Q, %	Q, J/g
0	455	/	100.0	00.0	111.3
5	440	562	94.5	05.5	120.2
10	444	568	62.1	37.9	54.7
15	434	514	44.6	55.4	18.0
20	438	510	31.1	68.9	10.1

7.2.2. The crystallisation of Ce-YSZ powders

According to the thermal analysis, Ce-YSZ powders were heated in DSC furnace at 350, 600 and 1400°C before XRD analysis. The XRD spectra show that, for ceria content up to 25 wt.%, the powders are amorphous up to 350 °C (Figure 25a). The annealing at the temperatures of 600°C and higher transfers the material in the face-centred cubic (fcc), fluorite-type structure. So, the exothermic effects observed on DSC curves between 350 and 600 °C are representative for the material crystallisation.

For ceria concentration of 30 wt.% and higher, the material also has a fcc crystalline, fluorite type structure after directly drying (Figure 25b), without apparent segregation of ceria.

After calcination at 600°C, all Ce-YSZ powders are crystalline and no apparent ceria segregation as a separate phase in the material was observed. In all cases, powders have fcc fluorite-type structure. These results are in agreement with the results presented in the work of Andrievskaya et al. [95] and Hinatsu et al. [96] who studied the ternary ZrO_2-Y_2O_3-CeO_2 system. According to the ternary phase diagram presented in their work, the binary system $(Zr_{0.84}Y_{0.16})O_{1.92}$-$CeO_2$ has a fcc, fluorite type structure in the complete range of ceria.

From the XRD dates, the lattice parameter (a, Å) was determined for all powders calcined at 600 and 1400 °C. In both cases, the lattice parameter (a) linearly increases with the ceria content (C_{Ce}):

$$a, Å = 2.73 \ 10^{-3} \cdot C_{Ce} + 5.148 \qquad T_C = 1400 \ °C \qquad (21)$$

$$a, Å = 2.64 \cdot 10^{-3} \cdot C_{Ce} + 5.155 \qquad T_C = 600 \ °C \qquad (22)$$

The dependence (21) follows the Vegard's law and is similar to the literature data [56, 58, 68, 97] (Figure 26) and the values of YSZ and pure CeO_2 correlate with the catalogue dates (JCPDS) [98, 99].

According to the dependence (22), the system already follows the Vegard's law directly after crystallization ($T_C = 600$ °C).

After calcination at high temperature in air, the YSZ-PuO_2 system crystallises in a solid solution fcc fluorite type structure and for plutonium concentrations lower than 20 %, follows the Vegard's law [58, 100, 101].

On the XRD spectra of powders calcined at high temperatures, a small peak appears at 31.5° and corresponds to the diffraction peak of $ZrSiO_4$. In fact, SiO_2 is present as impurities in the powders, coming form a slight dissolution of glass during synthesis and washing, and react with ZrO_2 to form the stable component $ZrSiO_4$.
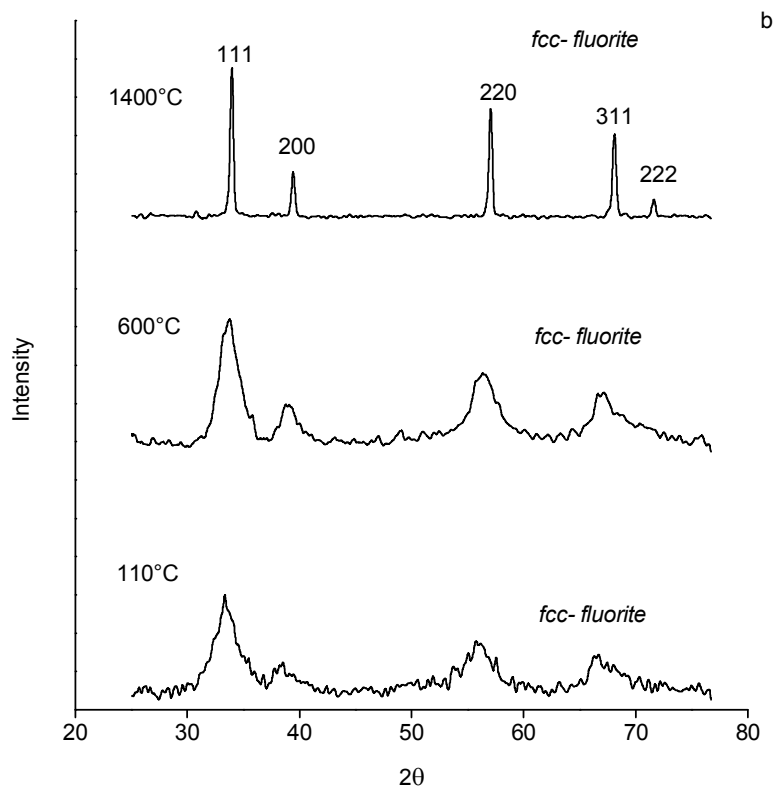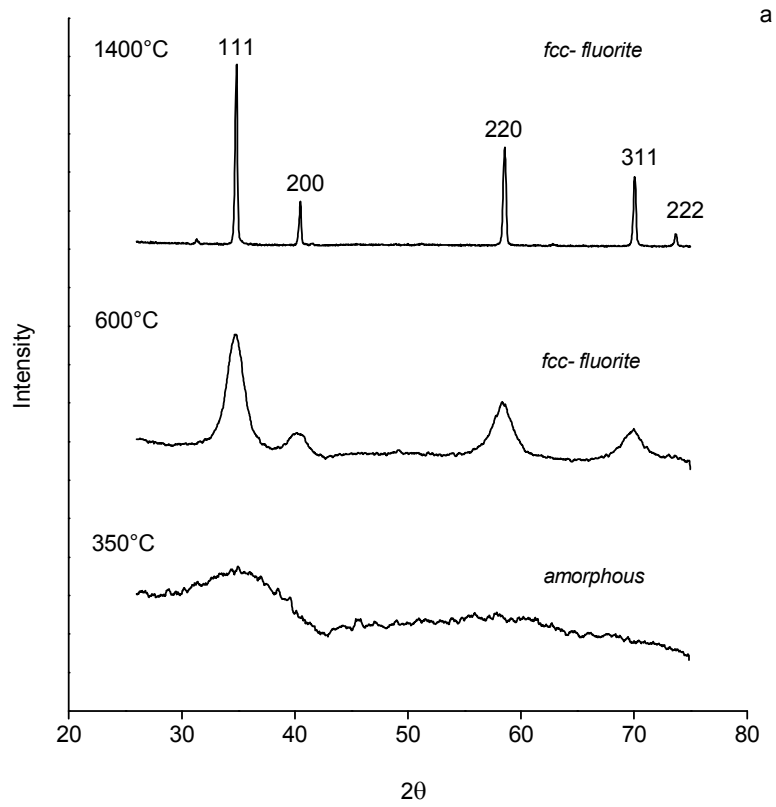
Figure 25. X-Ray diffraction patterns of 10-Ce-YSZ powders (a) and 60-Ce-YSZ powders (b) calcined at different temperatures.
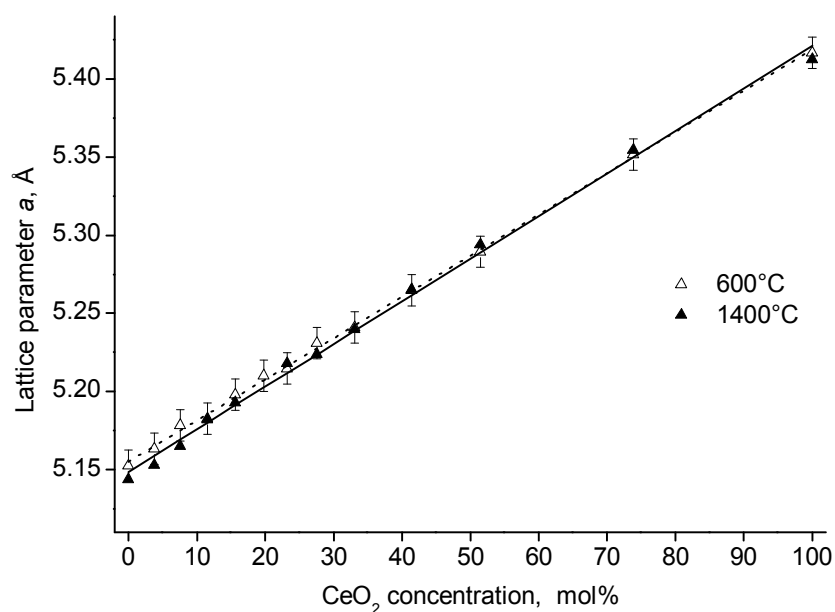
Figure 26. Lattice parameter of Ce-YSZ powders calcined at 600 and 1400 °C as a function of CeO₂ concentration (mol %).

According to these TG-DSC and XRD results, the Ce-YSZ system can be divided in two regions as a function of the ceria concentration : a first region (R1) from 0 to 25 wt.% of ceria and a second region (R2) from 40 to 100 wt.% of ceria.

In the first region, the properties of the investigated powders are substantially determined by the YSZ matrix. These powders are amorphous after drying and crystallise in a face centred cubic system (fluorite type) between 350 and 660°C. The crystallisation is accompanied on the DSC curves by a complex exothermic effect. The formation of the final Ce-YSZ stable solid solutions occurs at temperature around 1230°C.

In the second region, the properties of the investigated powders are substantially determined by ceria matrix properties. Theses powders also crystallise in a face centred cubic system (fluorite type) but already after drying and reach their stable solid solution at temperatures around 775°C (T_S).According to the T_S evolution, the range of CeO₂ concentration between 25 and 40 wt.%, is considered as a transition region.

7.2.3. The crystallisation behaviour of powders with 0 < [CeO$_2$] < 20 wt.%

The crystallisation behaviour of the Ce-YSZ powders was investigated into more details for each region defined previously

7.2.3.1. Signification of the double exothermic peaks

In the region R1, the Ce-YSZ system crystallises by a double exothermic effect in the temperature range from 350 to 600°C. These exothermic peaks are characterised by the temperatures T_{M1} and T_{M2} (Figure 24, Table 8) corresponding respectively to the temperature at the maximum of the first and second exo-effect (Table 9) and by their heat Q_1 and Q_2. The normalised heat of the first peak Q_1/Q, with $Q = Q_1 + Q_2$, decreases and the normalised heat of the second peak Q_2/Q increases with increasing of ceria (Table 9). Furthermore the temperature T_{M1} remains constant with the ceria content and correlates with the value of YSZ crystallisation (455°C-Figure 23a), while T_{M2} decreases (Table 9-Figure 24). So, it can be supposed that the first exo-effect is connected to the crystallisation of zirconia-yttria matrix and the second exo-effect is associated to ceria.

To confirm this hypothesis a detailed study was performed on the 10-Ce-YSZ powder and YSZ matrix, used as reference material. As described on Figure 24 and the Table 8, the DSC curve of the reference sample presents only one exo-effect between 420°C (T_I^R) and 525°C(T_F^R) with a maximum at 458°C (T_M^R). The 10-Ce-YSZ powder crystallises between 370°C (T_I) and 660°C (T_F), with two maximums at 445°C (T_{M1}) and 568°C (T_{M2}) for the first and the second peak respectively. The end of the first peak is located at the temperature (T_{F1}) 502 °C, which corresponds also to the temperature of the beginning of the second peak ($T_{I2} = T_{F1} = 502$ °C).

According to the TG and DSC results, the 10-Ce-YSZ powder was calcined at 370, 450, 500, 550, 600, 800, 950, 1400 and 1600°C before XRD analysis. For powders after drying and calcination at temperatures below 370 °C (T_I), no diffraction peaks are observed on the XRD spectra in Figure 27; the powders are amorphous. At temperatures higher than T_I, the diffraction peak of XRD spectra reveal that the material crystallises in a FCC fluorite-type structure. For powders calcined from 450 to 950°C, diffraction lines are wider and shifted to the smaller angels region compared to those for the powders calcined at 1400 and 1600°C. At temperatures higher than T_S, the material was transformed into a stable solid solution.
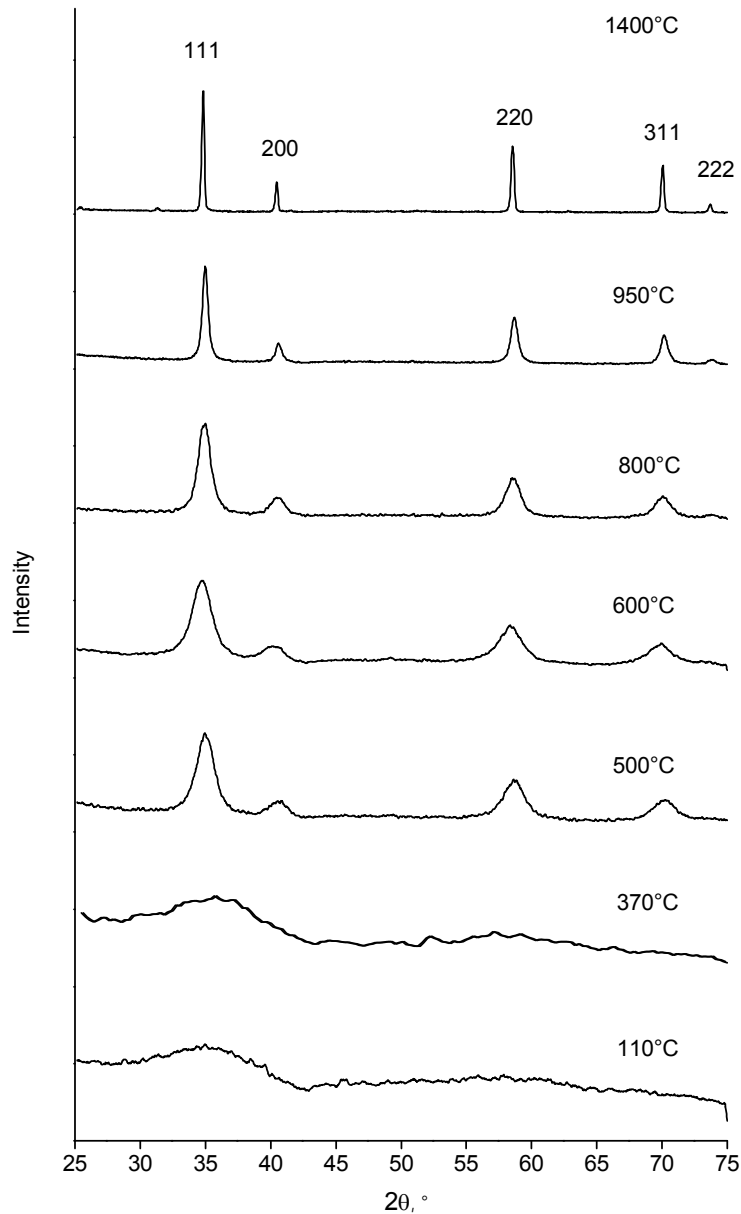
Figure 27. Powder X-Ray diffractograms for Ce-YSZ powders after drying at 110 °C and calcination at 370, 500, 600, 800, 950 and 1400 °C.

The dependence of the lattice parameter *a* of 10-Ce-YSZ and YSZ on the calcination temperature (Figure 28a) and on the mass loss (Figure 28b) was investigated in details. For both materials, the lattice parameter decreases with increasing calcination temperature (Figure 28a) and the mass loss (Figure 28b). At the temperature higher than $T_{I2} = 502°C$ and $T_I^R = 420°C$ for 10-Ce-YSZ and YSZ respectively, the lattice parameter has a linear correlation with the sample mass loss $(M_{Ti} - M_T)/M_{Ti}$ (Figure 28b). In this formula, M_T is the sample mass at the temperature T and M_{Ti} the sample mass at the beginning of the phase transition ($T_I = 370°C$ for 10-Ce-YSZ system or $T_I^R = 420°C$ for the reference sample). This linear correlation confirms that the lattice parameter is determined by the presence of OH-groups in the material [102].
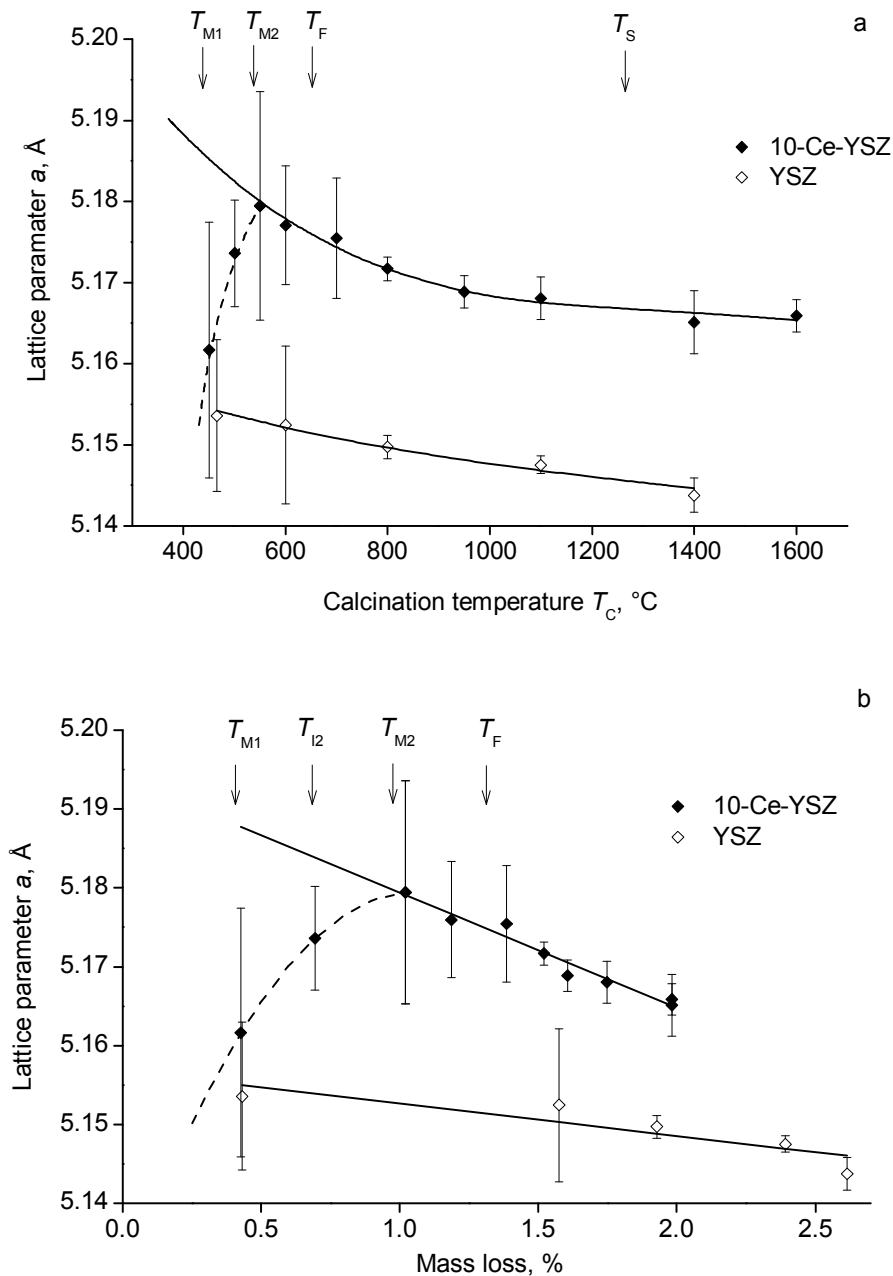
Figure 28. Dependence of the lattice parameter with the calcination temperature (a) and the mass loss (b).

In contrast, the 10-Ce-YSZ samples calcined at the lower temperatures $T_{M1} = 450\ °C$ and $T_{F1} = 502\ °C$ do not follow the above tendencies with the calcination temperature and the mass loss (Figure 28a,b). Their lattice parameters ($a_{TM1} = 5.162$ Å and $a_{TF1} = 5.174$ Å) are significantly lower than the values extrapolated from the higher temperatures ($a_{TM1}^{ext} = 5.185$ Å and $a_{TF1}^{ext} = 5.182$ Å). Moreover, after calcination at 450°C, the values of the lattice parameter of 10-Ce-YSZ and YSZ ($a = 5.162 \pm 0.016$ Å and $a^{R} = 5.154 \pm 0.009$ Å respectively) are very similar (Figure 28a,b).

It is known that ceria forms a homogeneous solid solution with yttrium fully stabilised Zirconia and that the lattice parameter of the $[(Zr_{0.84}Y_{0.16})_{1-y}Ce_y]O_{2-x}$ system increases linearly with the addition of ceria following the Vegard's law also after calcination at lower temperatures. So, it can be concluded that the low value of the lattice parameter at temperature lower than T_{F1} is connected with the deficiency of ceria in the crystallised material.

Hence, taking into account the TG-DSC (described above) and XRD results, the following sequence of material crystallisation can be assumed: predominant crystallisation of zirconia-yttria matrix with ceria deficiency in the temperature range from T_I to T_{F1} (first exo-effect) and incorporation of the rest of ceria in the crystal lattice in the temperature range from T_{I2} (T_{F1}) to T_F (second exo-effect) (Figure 24 - Table 8).

7.2.3.2. Evolution of the crystal structure parameters with the calcination temperature

The mean crystallite size and the lattice distortions of YSZ and 10-Ce-YSZ were determined as a function of the calcination temperature from the XRD results (Figure 29a and b).

The mean crystallite size L of YSZ powder increases from 2 to 47 nm while the lattice distortions $<\varepsilon^2>^{1/2}$ decrease from 0.4 to 0.01 % with increasing calcination temperature up to 1400°C (Figure 29a). After drying at 110°C and calcination at 350°C, the crystallite size is very small ($L \sim 2$nm) and represents the primary particle size produced by the co-precipitation method. During the drying step, the particles form large agglomerates due to their high adhesion activity after the evaporation of water. In fact, after drying, the powders consists of large agglomerates, of primary particle with different packing density (Figure 30). Heating at 450°C is responsible of the material crystallisation. The mean crystallite size L increases up to ~ 10 nm which remains constant up to 800°C. In this temperature region, the material is characterised by a high level of lattice distortion $<\varepsilon^2>^{1/2} \sim 0.18$ %, which is due to the presence of OH-groups in the matrix and the lattice rearrangement from amorphous to crystalline state. Heating the material above 800°C results in a recrystallisation of the material translated by a steep increase of the crystallite size up to 47 nm and further decrease of lattice distortion. Heating the material at temperature higher than T_S results in lattice stress relaxation and in crystallisation of the material to a stable phase. This reduces the lattice distortions to virtually zero.

10-Ce-YSZ powder presents a similar behaviour (Figure 29b). The crystallisation of material is responsible for a slight increase of the crystallite size from 2 to ~ 8 nm. Heating the material above 800°C results in a recrystallisation of material translated by a steep increase of the crystallite size and decrease of lattice distortion.
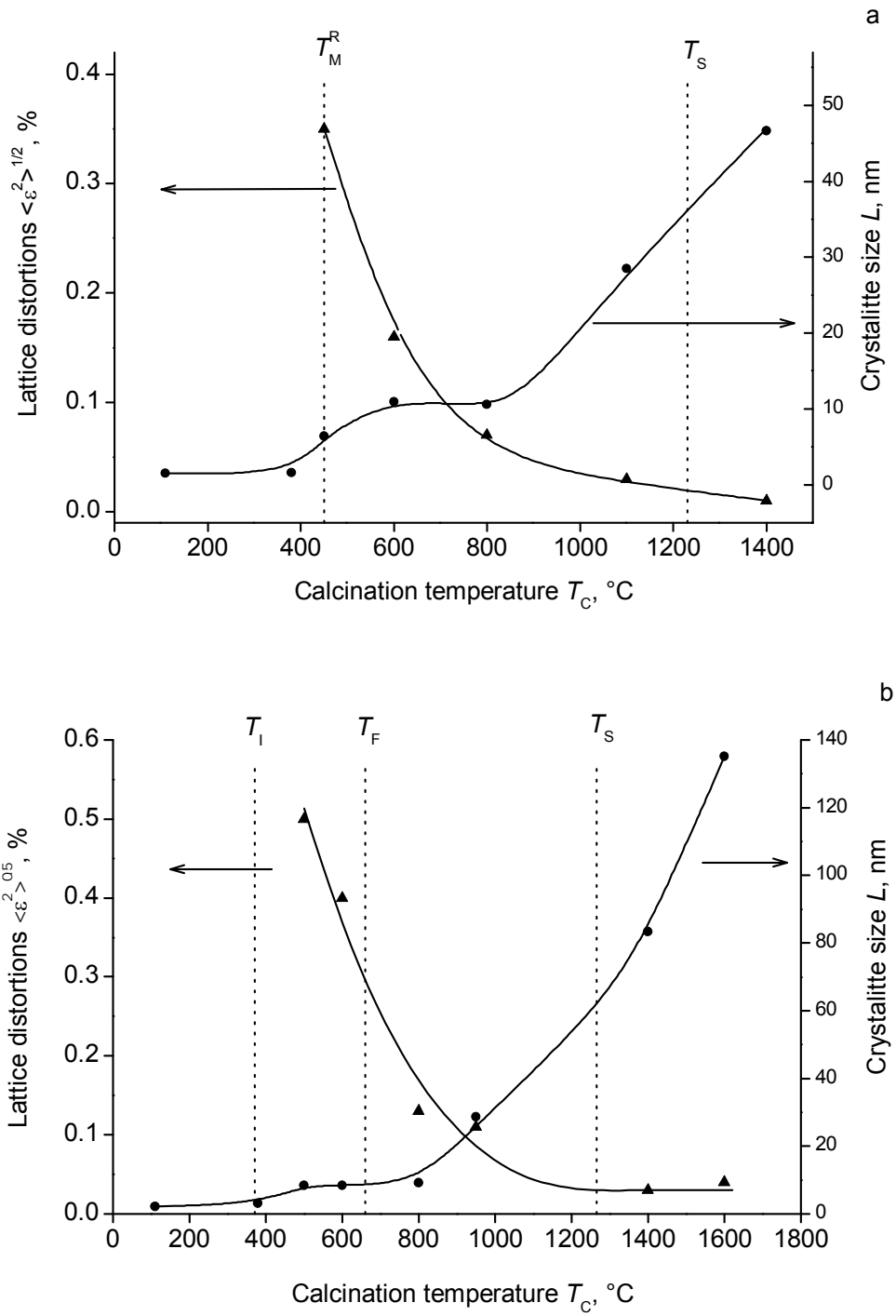
Figure 29. Evolution of the mean crystallite size (▲) and the lattice distortions (●) of the YSZ (a) and 10-Ce-YSZ (b) powders as a function of the calcination temperature.
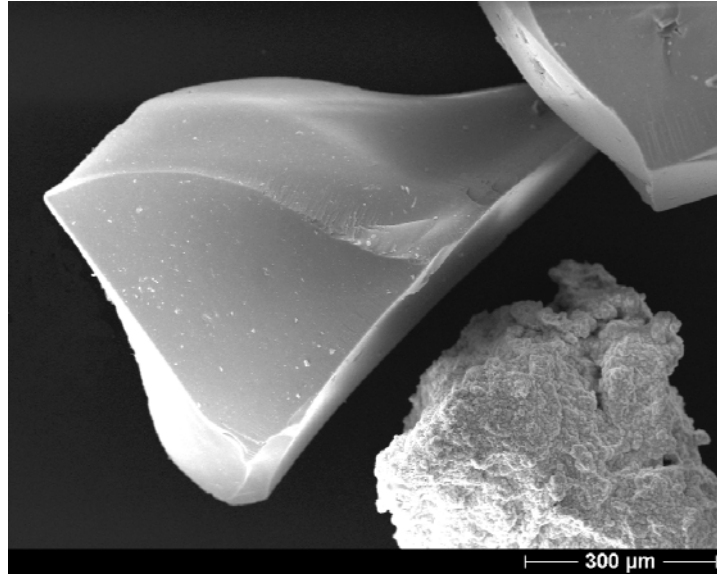
Figure 30. SEM photograph of YSZ powder after drying at 110°C.

For comparison, the relative crystallinity degree G of the YSZ and 10-Ce-YSZ powder were also determined as a function of the calcination temperature (Figure 31). After drying, 10-Ce-YSZ and YSZ powders are amorphous. Their relative crystallinity degree reachs a value of 1%, which remains constant up to 380°C. During the phase transition from amorphous to crystalline, G increases up to 27% or 10% for YSZ and 10-Ce-YSZ powders respectively and then remains constant up to 800°C. At temperatures higher than 800°C, the crystallinity strongly increases up to 100 % at 1400°C.
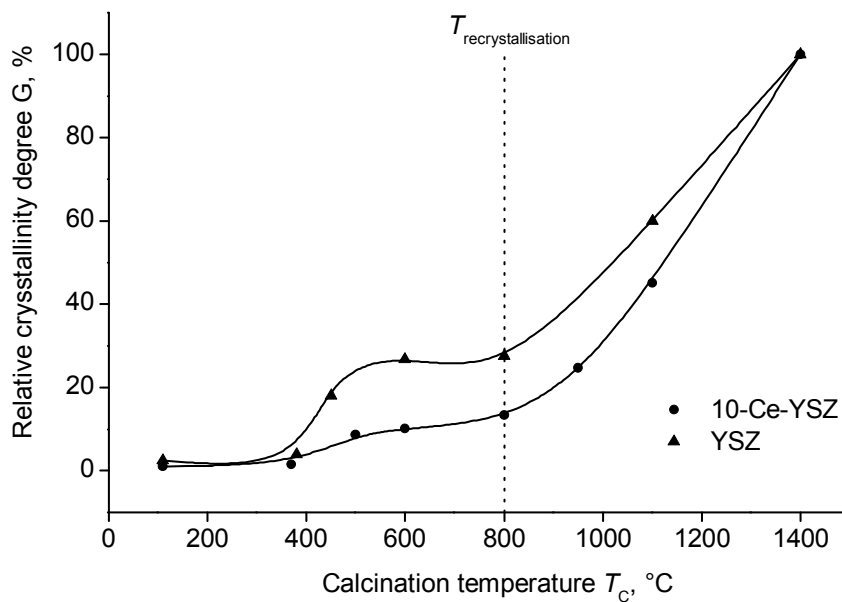
Figure 31. Evolution of the relative crystallinity degree G of YSZ and 10-Ce-YSZ powders as a function of the calcination temperature.

For both powders a recrystallisation process takes place starting from 800°C. A difference of 17% in crystallinity is observed between YSZ and 10-Ce-YSZ after crystallisation. In fact, the crystallisation of those material is exothermic and the intensity of the peak decreases with the addition of ceria. Thus, a correlation can be established between the crystallinity degree of the material and the total specific heat released during its crystallisation. The behaviour of the crystallite size with the calcination temperature is similar with the relative crystallinity degree.

7.2.4. The crystallisation behaviour of powders with 40 < [CeO₂] < 100 wt.%

In the second region with ceria concentration higher than 40%, the Ce-YSZ powders are crystalline at room temperature already. The crystallisation behaviour of 60-Ce-YSZ and pure CeO_2 powders, as reference, were studied in more details. Thus, after calcination at 350, 475, 600, 775, 1100, and 1400°C, the lattice parameter (a) and the relative crystallinity degree (G) of the powders were determined as a function of calcination temperature T_C.

In both cases, their lattice parameter decreases continuously with calcination temperature. A linear dependence was established between the lattice parameter and the mass loss (ML = $(M_{Ti} - M_T)/M_{Ti}$, defined in 7.2.3.1. p 73) from 350°C (Figure 32). The decrease of lattice parameter is so connected to the elimination of OH-groups from the lattice [102]
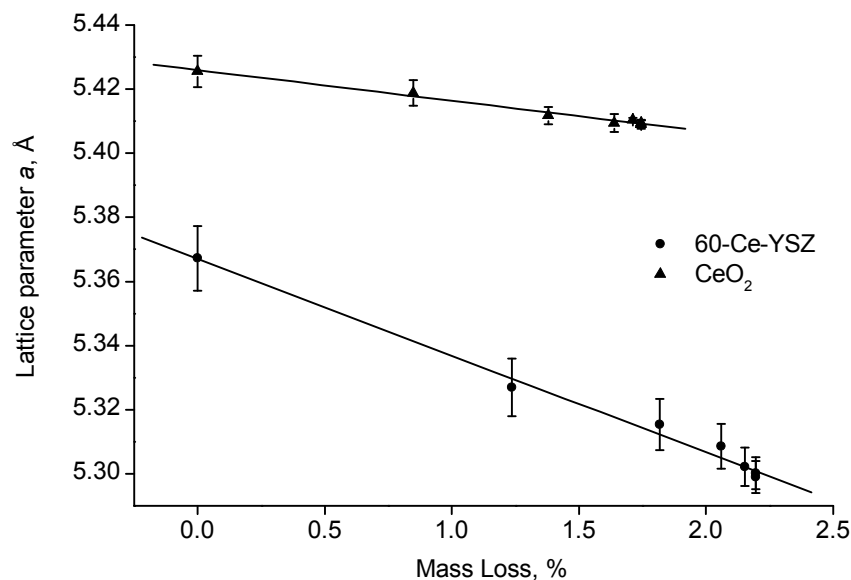
Figure 32. Lattice parameter as a function of mass loss for 60-Ce-YSZ (●) system and pure CeO₂ (▲).

The evolution of the relative crystallinity degree (G) with the calcination temperature was investigated in both cases (Figure 33). Pure CeO_2 has a crystallinity of 19% after drying, which remains constant up to 350°C. Increasing the temperature up to 475°C is responsible of an increase of crystallinity, which reaches a value of 27%. Then G remains stable until 775°C,

and then steeply increase up to 100% at 1100°C. The recrystallisation takes place at 775°C, which corresponds to the value of T_S, temperature of stable solid solution formation

60-Ce-YSZ powder has a similar general behaviour. Its crystallinity at 110°C was evaluated at 13%. A first increase of crystallinity is observed between 475 and 600°C, where G reachs a value of 20%. Then G remains stable until 775°C, and then steeply increases up to 100 at 1400°C. The recrystallisation also takes place at T_S.
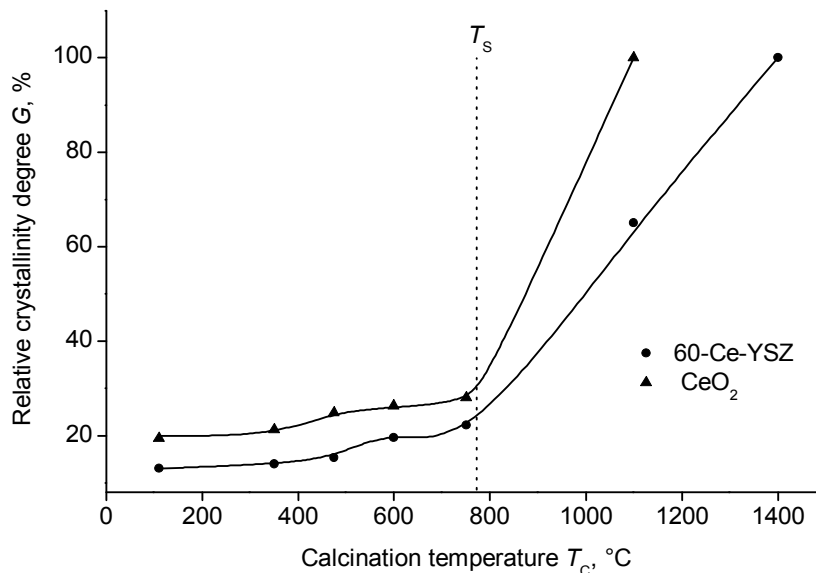
Figure 33. Evolution of the crystallisation degree 60-Ce-YSZ (●) system and pure CeO$_2$ (▲).

7.2.5. The effect of ceria concentration on the crystallinity of Ce-YSZ powders after calcination at low temperatures.

The dependencies of the crystallinity degree G with the ceria content were determined for all powders after drying at 110°C and after calcination at 600°C (Figure 34).

For dried powders, the value of G first remains constant at ~ 2 %, indicating the amorphous state of the material. By increasing the concentration up to 40 wt.%, the crystallinity degree steeply increases to 7 % and then continuously increases up to 19 %, value obtained for pure CeO$_2$. For ceria concentrations higher than 15 wt.%, the behaviour of calcined powders is similar to that of dried powders. However, the level of crystallinity is higher and reaches a value of 8 % at 15 wt.% ceria and a value of 27 % for pure ceria (Figure 34).

For powders calcined at 600°C, in the concentration range lower than 15 wt.%, the relative crystallinity degree drastically decreases from 27 % to 7 %. As shown above, the crystallisation of the material is exothermic for low ceria content and the total specific heat decreases abruptly with ceria addition. Thus, a correlation can be established between the crystallinity degree of the material and the total specific heat released during its crystallisation.
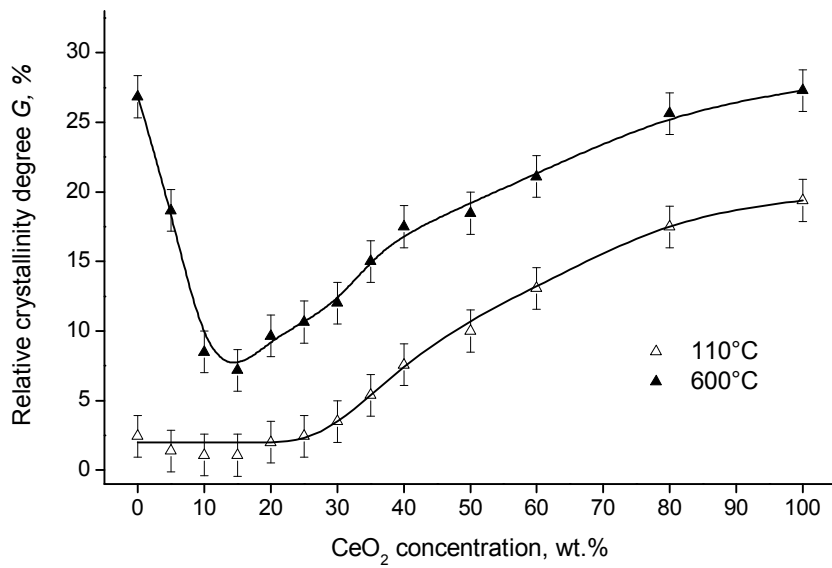
Figure 34. Dependence on ceria content of the relative crystallinity degree of Ce-YSZ powders dried at 110 °C and calcined at 600 °C.

The mean crystallite size (L, nm) and the lattice distortions ($<\varepsilon^2>^{1/2}$, %) of powders calcined at 600°C were also determined as a function of ceria content and the results are plotted in Figure 35. For ceria content from 0 to 15 wt.%, L uniformly decreased from 10.9 to 5.8 nm, then remains constant until 40 wt.% and increases again up to 9.0 nm for pure ceria. Simultaneously, the lattice distortion steeply increases from 0.16 to the maximum of 0.38 % at 15 wt% ceria, and then continuously decreases to 0.20 %, for pure CeO_2. The behaviours of L correlate with the data of G.

Figure 35. Effect of the ceria concentration on the mean crystallite size (●) and lattice distortion (▲) of Ce-YSZ powders calcined at 600 °C.

7.3. Fabrication of 10-Ce-YSZ ceramics

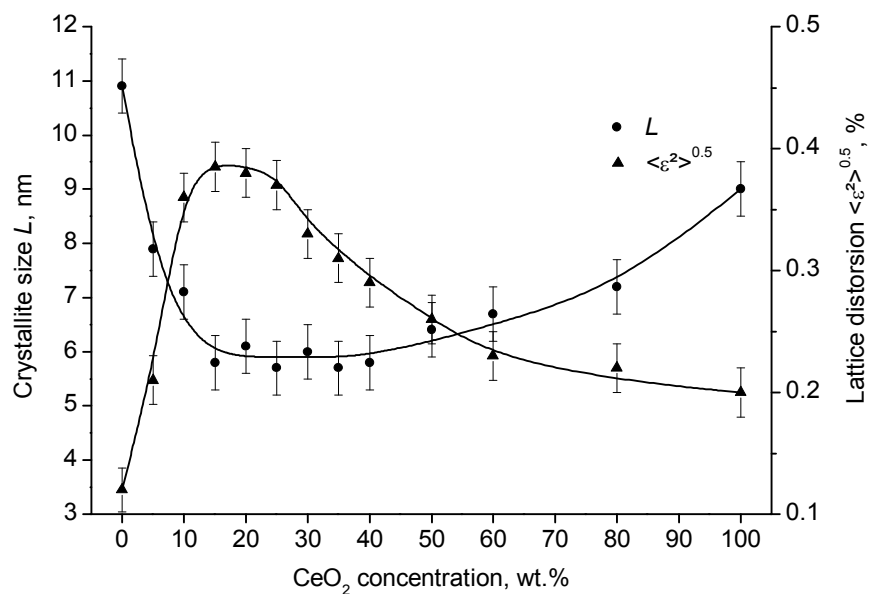The immobilisation of actinides in YSZ requires the development of advanced ceramics, with reliable and reproducible properties, as well as simple fabrication processes. In this frame the fabrication of $(Zr,Y,Ce)O_{2-x}$ pellets was studied in details. The technological parameters such as the calcination temperature, and compacting pressure were optimised, based on the study of the representative system 10-Ce-YSZ. Then, similar experiments were performed for the other ceria concentrations, in order to study the impact of ceria on the properties of pellets.

10-Ce-YSZ powders were first prepared by co-precipitation of nitrate solution by NH_3. After washing and drying at 110°C for 24 hours, the powders were calcined at different temperatures T_C: 110, 350, 600, 800, 950, 1100, 1400 and 1600°C. Their properties such as morphology, compressibility, sinterability, and densification behaviour were studied in details.

7.3.1. Powders morphology

The synthesised Ce-YSZ powders have different yellow colours depending on the ceria content and an estimated bulk density of about 1.2 g/cm^3. After a mild grinding by attrition, the powders contain agglomerates with irregular shapes, which differ in their primary particles packing density (Figure 36). According to the literature [54, 92], the agglomerates with high-packed density are the so-called "hard" agglomerates, while the low-packed agglomerates are called "soft" agglomerates.
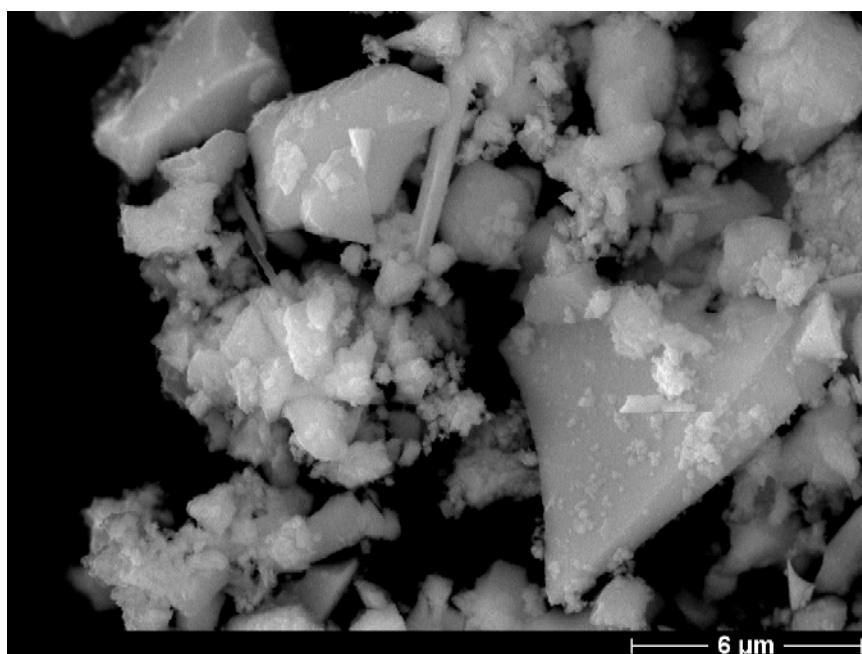

Figure 36. SEM photograph of 10-Ce-YSZ powder after grinding.

The agglomerate size distribution was determined using an optical microscope. The mass distribution of the representative case of 600°C calcined powder is reported in Figure 37. The distribution is ranged up to 60 μm and presents two maxima at 12 and 48 μm. However, the majority of the agglomerates has a size located between 2 and 30 μm. So, a mild grinding step provides an inhomogeneous powder, with small but also coarse agglomerates.
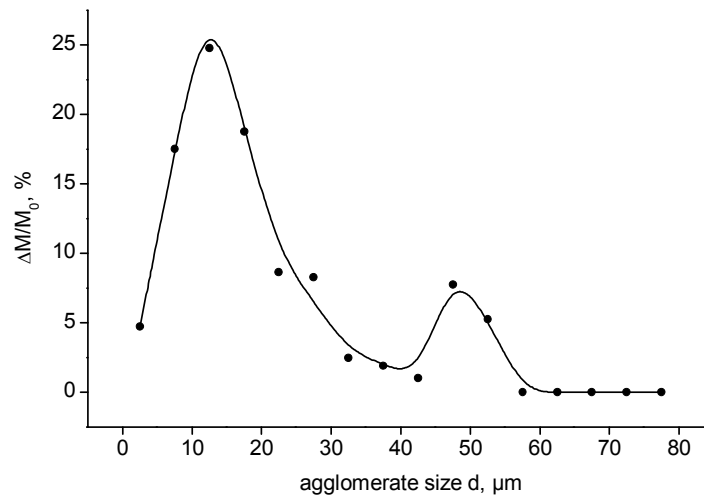

Figure 37. Mass distribution of the agglomerate size of 10-Ce-YSZ powder calcined at 600°C and ground by attrition.

7.3.2. Compressibility of the powder

Powder calcined at low calcination temperature, from 110 to 600°C, were compacted by cold uniaxial pressing, applying pressures between 130 and 1020 MPa. Their relative green densities were determined as a function of the pressure. As represented in Figure 38 in the case of a calcination at 600°C, the relative green densities are plotted as a function of the logarithm of the applied pressure, revealing two linear dependences with an intersection point at pressure of P_Y. Powders calcined at lower calcination temperature, present the same compressibility curves. However, the value of P_Y increases with the calcination temperature, from 400 MPa for powders dried at 110°C to 840 MPa for powders calcined at 600°C. The values are reported in the Table 10.

A similar behaviour of the compressibility was obtained in the work of Van de Graaf et al. [54, 106] and Groot Zevert et al.[93]. In this last cited work, ZrO_2 - 3 mol % Y_2O_3 powders, prepared by gel-precipitation technique and calcined at 547 °C, show one intersection point at 80 MPa, denoted as the strength of the biggest element. In that case, the biggest element was the agglomerate of particles. The authors demonstrate that at pressures below P_Y, these agglomerates are only rearranged and that at a pressure around P_Y, they are all gradually fragmented. In our case, the largest elements are coarse hard agglomerates. Thus, the measured P_Y, would correspond to the coarse hard agglomerates strength.
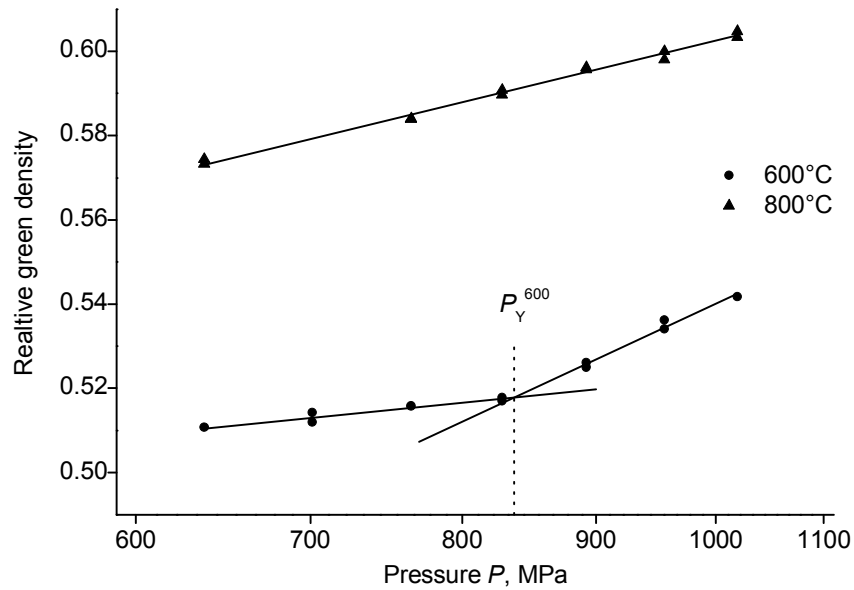
Figure 38. The relative green density of 10-Ce-YSZ pellets made from ground powder calcined at 600 °C and 800 °C in dependence of the compacting pressure P.

Table 10. The coarse hard agglomerates strength (P_Y) of powders calcined at T_C = 110, 350 and 600°C.

T_C [°C]	110	350	600	800
P_Y [MPa]	400	540	840	/

SEM investigations were performed on green bodies at pressure below P_Y and higher than P_Y. As seen on Figure 39, the green body consists of soft and hard agglomerates of different sizes. The green bodies contains also coarse hard agglomerates. At pressure below P_Y, these agglomerates are intact (Figure 39a) , while at pressure higher than P_Y they are fragmentised (Figure 39b).

Two regimes of packing depending on the applied pressure P, can therefore be distinguished:

- If $P < P_Y$, then the compaction occurs by rearrangement of all agglomerates.

- If $P > P_Y$, then coarse hard agglomerates are fragmentised during the compaction.

The measured P_Y can be named coarse hard agglomerates strength.

$T_C = 350\ °C$

$(P < P_Y)$ $P > P_Y$

$T_C = 800\ °C$

$P = 640$ MPa $P = 1020$ MPa
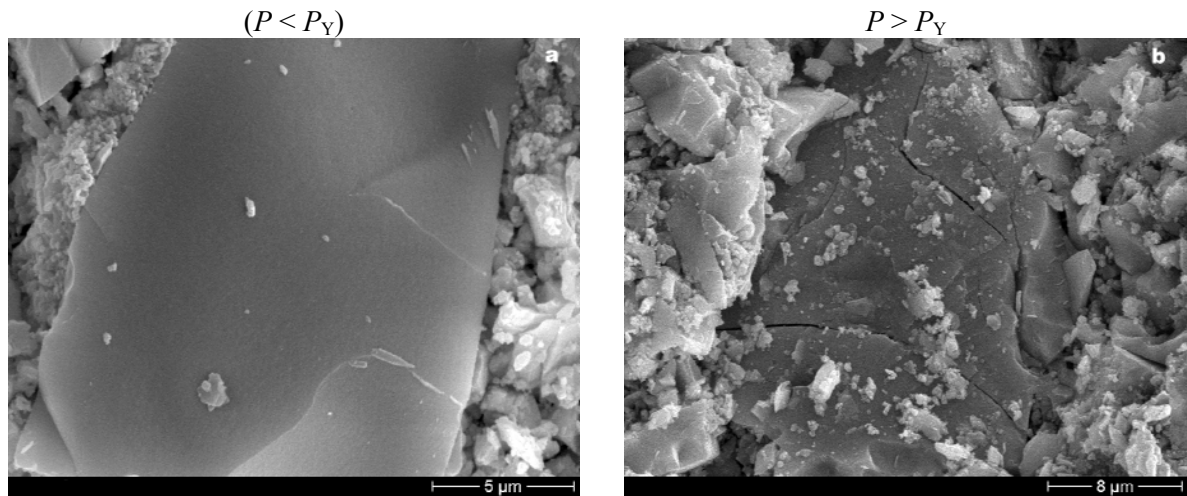
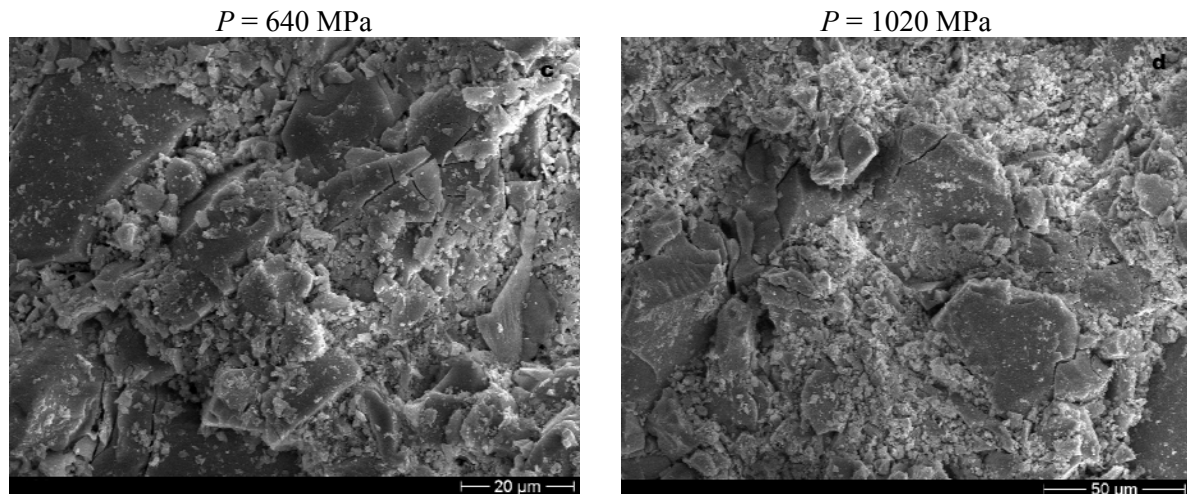**Figure 39. SEM photograph of the fractured green body made from 350°C calcined powder (a,b) and at 800°C (c,d) pressed at low pressure (a,c) and at high pressure (b,d).**

Powders calcined at high temperatures were also compacted by cold-uniaxial pressing applying pressures from 650 to 1000 MPa. As seen in Figure 38, for 800°C calcined powders, the relative green density of pellet linearly increases with the logarithm of the pressure, presenting no bend. The microstructure of the green body was investigated by SEM. As seen on the Figure 39, the green body mainly consists of coarse hard agglomerates. In fact at 800°C, the recrystallisation process has started, being responsible of an agglomerate hardening. These agglomerates are so in contact even when they are pressed at "low" pressure. The contact between these agglomerates is responsible for agglomerates crashing, at low (Figure 39c) and at high pressure (Figure 39d). Thus, only one regime of packing is distinguished in the case of powders calcined at high temperature.

At fixed pressure P = 1020 MPa, the density of the green bodies linearly increases from 0.45 to 0.69 of the theoretical density (TD) with increasing the powders calcination temperature from 110 to 1400°C (Figure 40). This effect can be associated to the evolution of particle morphology resulting from the elimination of OH-groups and the recrystallisation of material during calcination.
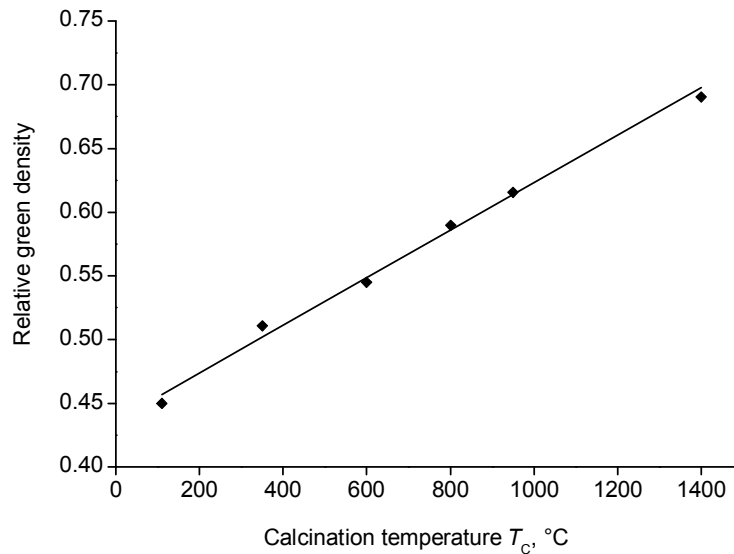
Figure 40. Evolution of the relative green density of the 10-Ce-YSZ pellets as a function of the calcination temperature.

7.3.3. Sinterability of the material

After compaction, the pellets were sintered at 1600°C for 5 hours in air atmosphere. The sinterability of powders after drying (110 °C) and after calcination at 350, 600 and 800°C was investigated as a function of compacting pressure.

The sinterability curves of powders only dried at 110 °C have a pronounced maximum in the region of small pressures, Figure 41. Considering that the optimal compacting pressure (P_{opt}) corresponds to the pressure at the maximal value of sintered density, P_{opt} is in this case located between 250 and 350 MPa. In this region, pellets reach densities up to 0.92 TD. The pellets prepared from dried powders are sensitive to under- and over-pressing. The low values of the green densities and the crystallisation of material accompanied by the elimination of a considerable quantity of water from the samples are responsible for these sensitivities, respectively.

The sinterability curves of powders calcined at 350 °C also have a maximum but in the region between 500 and 650 MPa, Figure 41. By increasing the calcination temperature, the optimal pressure zone is enlarged and shifted to the highest pressures. In the zone of the optimal compacting pressure, pellets also reach densities up to 0.92 - 0.93 TD.

The sinterability of powders calcined at 600°C or 800°C has no pressure dependence at high pressures (Figure 41). In the pressure range from 600 to 1000 MPa the densities of the sintered pellets are constant and the samples have similar physical properties. Pressures higher than 750 MPa can therefore be chosen as optimal compacting pressures. In the case of powder calcined at 600°C, pellets reach densities up to 0.93 TD while in the case of powder calcined at 800°C, the density is only 0.84 TD. Thus, by increasing the calcination temperature, the optimal pressure increases and the region of optimal pressure is enlarged.
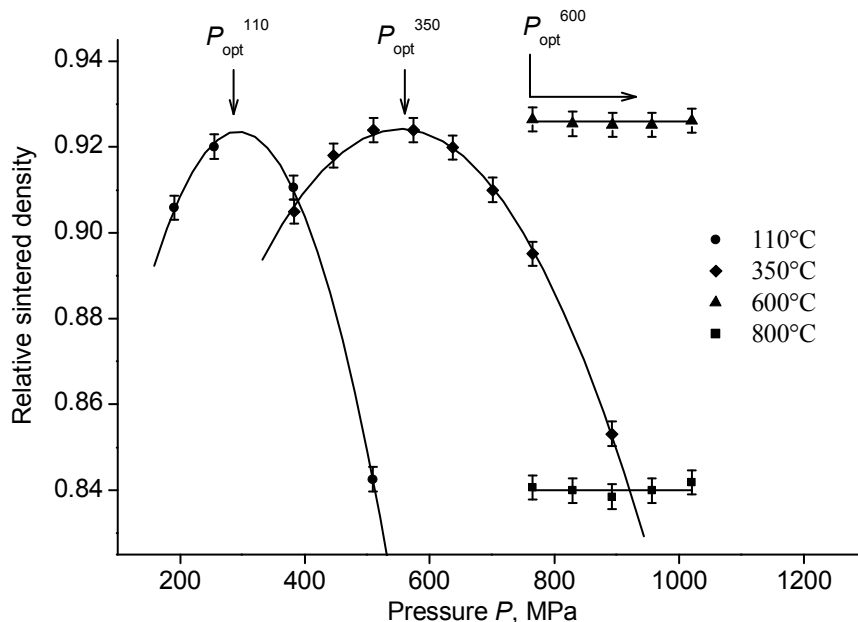
Figure 41. Evolution with the compacting pressure of the relative sintered density of 10-Ce-YSZ pellets, made from ground powder calcined at different temperatures.

This dependence of the sintered densities on the calcination temperature (Figure 42) clearly shows that the powder has a better sinterability when it was calcined at low calcination temperature (from 110 to 600°C). In this case the density of pellets reaches a value of 0.92 TD. On contrary, if the powder is calcined at 800°C and higher, the density of the sintered pellets decreases to 0.84 TD.
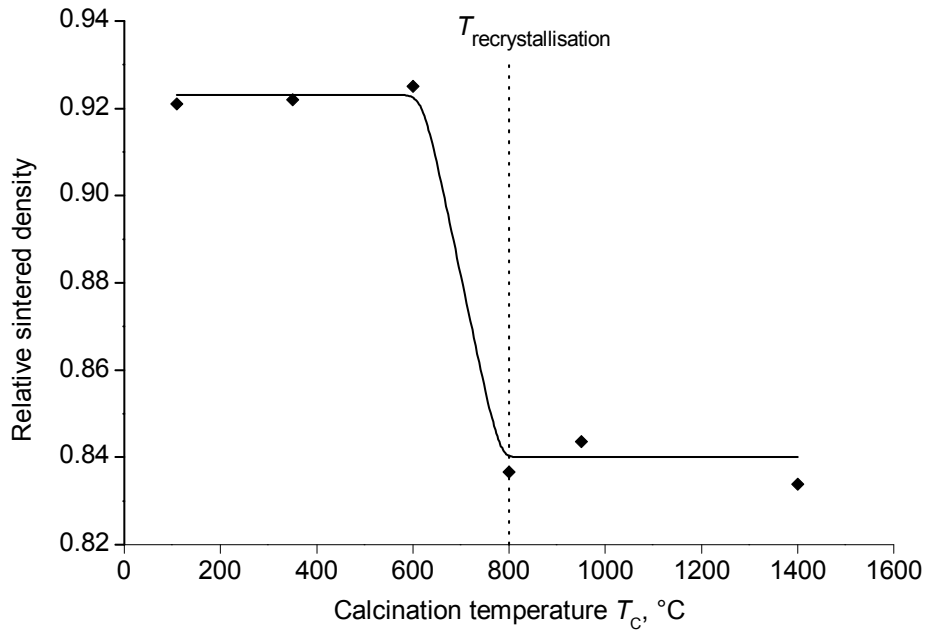
Figure 42. Evolution with the compacting pressure of the relative sintered density of 10-Ce-YSZ pellets, made from ground powder calcined at different temperatures.

The higher sinterability of powder calcined at temperature lower than 600°C is certainly determined by the high activity of the powder (low crystallite size and high lattice distortions, Figure 35) [108]. At higher temperature the recrystallisation effect changes the nature of powder and the microstructure of the green material and so the densification process.

7.3.4. Densification behaviour of the pellets

The density evolution, during sintering, of pellets made from ground powder was additionally studied by dilatometry for different calcination temperatures. The relative density of pellets and the densification rate were computed from the experimental linear relative shrinkage [83] with an additional mass loss correction (TG data). The representative case of powder calcined at 600°C is reported in Figure 43.

The sintering of powder starts at 800 °C, which corresponds to the beginning of recrystallisation process in material. Above 900°C the densification rate increases reaching a maximum at 1230°C. However, at temperature higher than 1230°C, the densification rate is decreasing abruptly (Figure 43). It can be seen that the relative density curve presents a bend at ~ 1320°C. All pellets, independently of their calcination temperature, show similar behaviour during sintering.
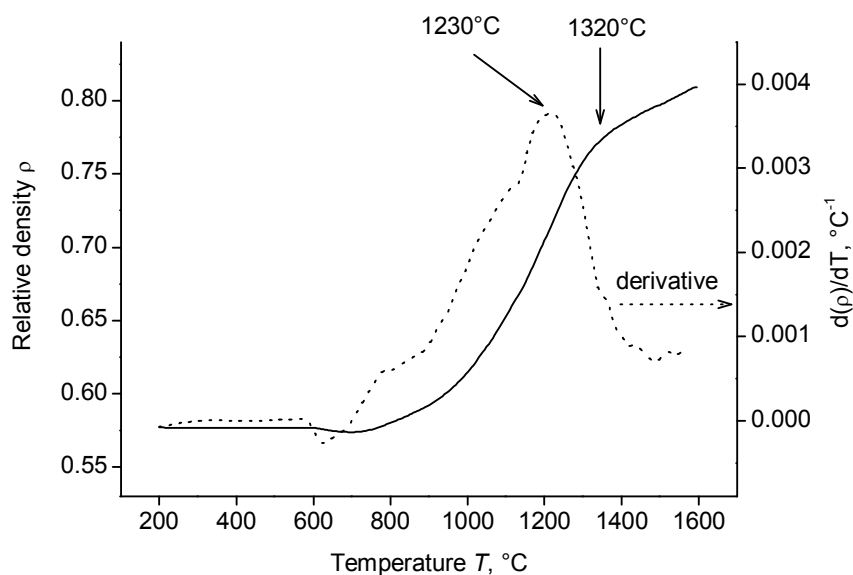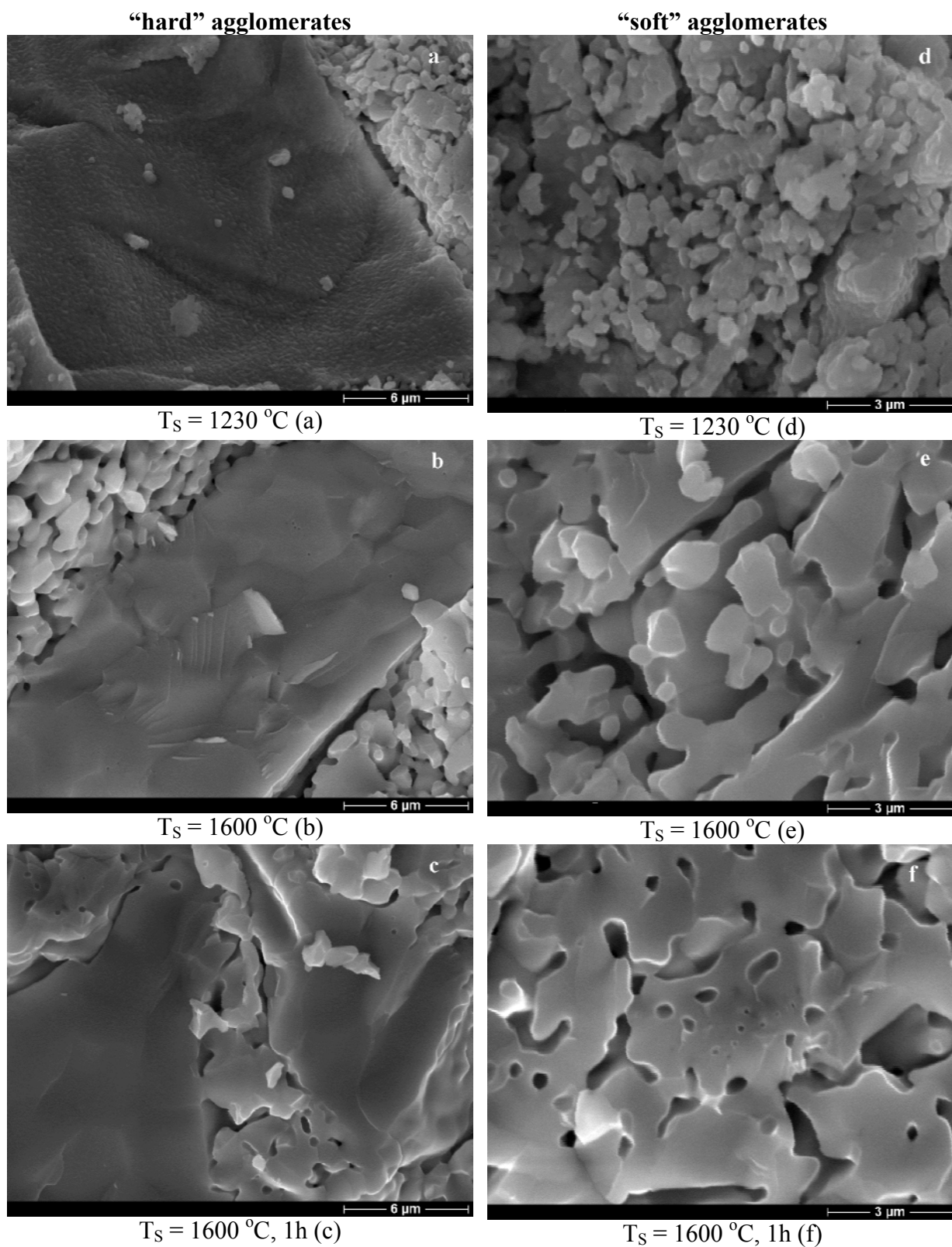
Figure 43. Evolution with the annealing temperature of the relative density ρ (full line) and its derivative $d(\rho)/dT$ (dotted line) of 10-Ce-YSZ pellet, made from ground.

The peculiarities of the morphological structure of pellets after sintering at different temperature were investigated by SEM, which revealed differences in densification of "hard" and "soft" agglomerates (Figure 44). As shown in Figure 44a, the annealing of pellets up to 1230°C is accompanied by a full densification of „hard" agglomerates. They consist of close-packed particles with an average size of 0.3 µm. It seems that the material sintering at low temperatures is determined by the high initial density of "hard" agglomerates, the small crystallite size (L ~ 8 nm at 600°C) and the active surface of initial particles. On contrary, the annealing of soft agglomerates up to 1230 °C, also results in increase of particle size to 0.3 µm, but only in minor increase of the agglomerate density (Figure 44d).

Subsequent heating up to 1600 °C is accompanied by a significant increase of crystallite size up to 2 - 4 µm for both types of agglomerates (Figure 44b,e). Moreover, the soft agglomerates form typical necks. During heating, the different sintering behaviour between the soft and hard agglomerates is responsible for elongated pores formation along the hard agglomerates borders (Figure 44b).

Annealing at 1600°C for one hour is accompanied by densification of material due to the sintering of „soft" agglomerates, which leads to a dense structure with closed submicron pores, Figure 44c,f.

$T_S = 1230\ ^oC$ (a)

$T_S = 1230\ ^oC$ (d)

$T_S = 1600\ ^oC$ (b)

$T_S = 1600\ ^oC$ (e)

$T_S = 1600\ ^oC$, 1h (c)

$T_S = 1600\ ^oC$, 1h (f)

Figure 44. SEM photographs of "hard" (a, b and c) and "soft" (d, e and f) components of a 10-Ce-YSZ pellet after shock sintering at 1230°C, 1600°C and after holding the temperature at 1600°C for one hour.

According to these results and the literature [109], the bend observed in the densification curve (Figure 43) for powder after grinding by attrition can be explained in the following way. At temperature up to 1230 °C the material densification takes place mainly by sintering of „hard" agglomerates and formation of a "rigid" skeletal structure in the material. During following heating, the presence of this rigid framework hampers the sintering of "soft" agglomerates.

Moreover, this densification behaviour correlates with the work of Lange [104] who studied the sinterability of Al_2O_3 agglomerated powders prepared by co-precipitation. The agglomerates are themselves made up of smaller and more densely packed subunits, which are called domains. During heating of these powders to 1000 °C, domains densify, without apparent shrinkage. Subsequent heating to ∼ 1300 °C, interagglomerates pores form dense agglomerates and shrinkage. Interagglomerates pores disappear on further heating to 1600 °C. Some interagglomerates pores remains at 1600 °C resulting in a final density lower than the theoretical one.

Shi et al. [110] studied the sintering behavior of fully agglomerated zirconia compacts. Fully agglomerated superfine powders were prepared by the co-precipitation method. Two sintering stage were identified: densification within agglomerates at temperatures not higher than 1250 °C and the removal of interagglomerate pores at temperatures above 1600 °C. The interagglomerates pores are difficult to remove and sintering between agglomerates even at 1600 °C is still insignificant. Heating the compacts at temperatures above 1600 °C leads only to grain growth and the entrapping of pores in large grains.

7.3.5. Microstructure of the pellets

Our pellets fabricated at optimal pressure were polished and their microstructure analysed by SEM. All pellets made from powders calcined at low temperatures (110-600°C) have the same type of microstructure. As represented in the case of a pellet performed from 350 °C calcined powder (Figure 45), the material has a homogeneous microstructure with uniformly distributed pores. Pores are mainly located at triple grain boundary junctions and inside the grains. These pores are the consequence of the different sintering behaviour between the soft and hard agglomerates, which is responsible of the formation of elongated pores along the hard agglomerates borders (Figure 44b). These pores remains during the sintering stage along the grain boundaries (Figure 45). The pores located inside the grains are representative of a non complete densification of the sample. These pores can be closed only by a volume diffusion process. The grains have various curved grain boundaries, representative of a non-complete sintering. The average grain is ∼ 18 μm and the ratio of the maximum to minimum grain size in the order of 1.6.
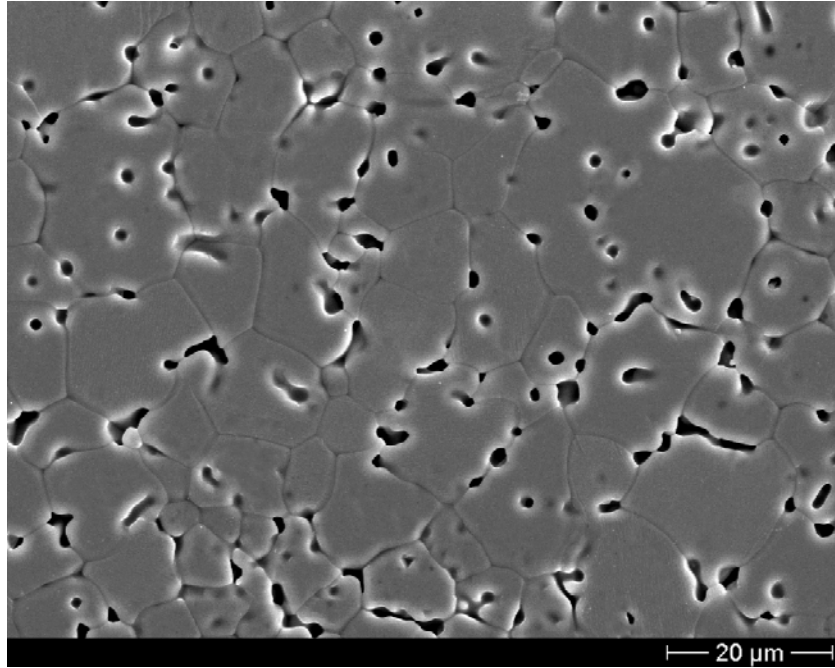
Figure 45. SEM photograph of a 10-Ce-YSZ pellet made from 350°C calcined ground powder.

As seen in Figure 46a, the surface of pellets made from powder calcined at 800°C is composed from very dense regions, separated by extremely porous regions. In fact, the coarse hard agglomerates have very well densified rapidly, giving a dense microstructure (Figure 46b) and forming a rigid framework. In between the small hard and soft agglomerates have sintered, let appear large pores at the boundaries of these coarse agglomerates (Figure 46b). The microstructure of the porous regions is similar to that obtained in the case of powders calcined at lower temperatures.

7.3.6. Comparison with literature

Since more than 40 years, ceramic matrices for encapsulation of radioactive materials are in discussion, specially for actinides. Some methods for the fabrication of advanced ceramics for nuclear applications are proposed in the last 5 years.

Thus, Boucharat et al. [57] prepared $(Zr,Y,Ce)O_{2-x}$, containing 10 wt.% of ceria. In their work $(Zr,Y)O_{2-x}$ porous microspheres produced by sol-gel methods were infiltrated by cerium nitrate solution and then calcined at 850 °C. The spheres were then pressed and sintered at 1680 °C for 6 hours. Pellets were fabricated to a density of 0.92 TD. The pellets had a homogeneous structure, without macro- or microcracks. However, the investigations of the microstructure have shown that the contours of the original spheres in the pellets can be discriminated. In fact, the porosity is mainly located in the peripheral regions surrounding the original sphere. $(Zr,Y,Pu)O_{2-x}$ pellets were prepared by the same method [58], reaching densities between 0.86 and 0.92 TD. The pellets showed the same microstructure.
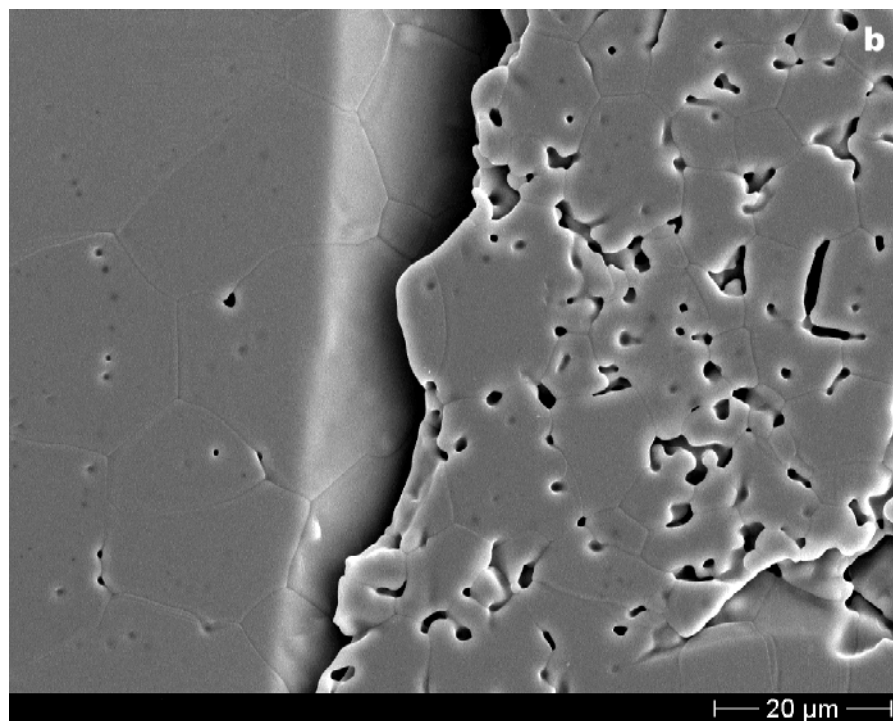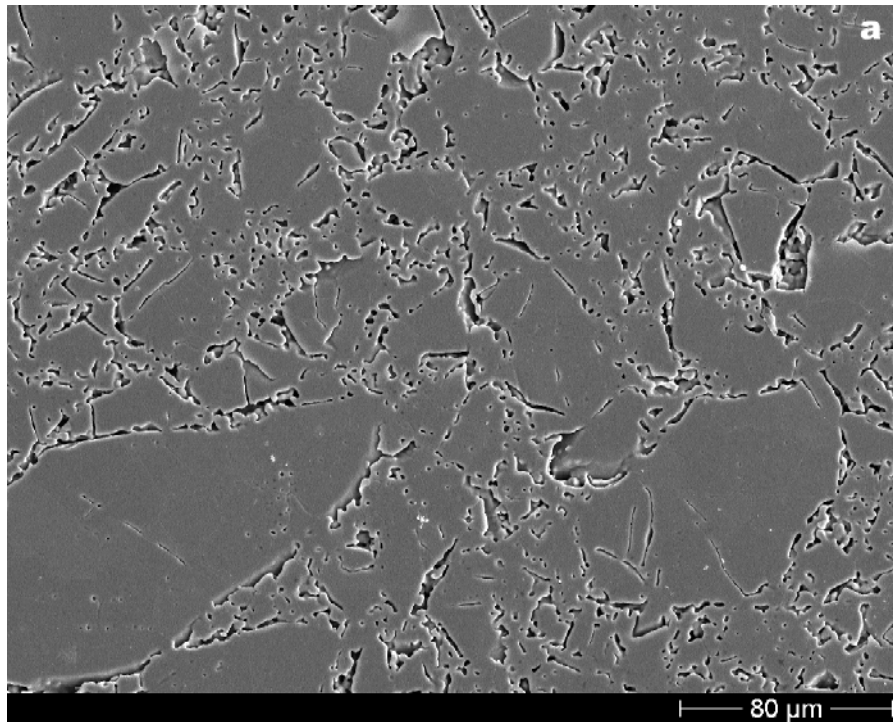
Figure 46. SEM photographs of 10-Ce-YSZ pellets made from 800°C calcined ground powder.

Lee et al. [50], prepared $(Zr,Y,Er,Ce)O_{2-x}$ powder using three different routes:

- dry mixing and milling of the oxide constituents

- co-precipitation of mixed solutions by use of ammonia

- co-precipitation in the form of microspheres by internal gelation

After a calcination step at 800 °C - for the co-precipitated powders, the powders were then milled and compacted and sintered at 1600°C for 5 hours. Pellets exhibit densities between 0.89 and 0.92 TD for mixed powder and co-precipitated respectively. Pellets are homogeneous, with a grain size of 17 μm. The microstructure is similar to that obtained in the case of powder and had a similar microstructure than presented in Figure 45. The pellets had larges pores, located at the triple junction, along the grain boundaries and inside the grains. $(Zr,Y,Er,Pu)O_{2-x}$ ceramics were prepared by dry mixing and milling of the oxide constituents (IMF-ATT process) and by co-precipitation as microspheres obtained by internal gelation (IMF-CO process) [101]. For the IMF-ATT-process the powder constituents were mixed mechanically in a vessel and milled in an attrition mill. The pellets were pressed at 500 MPa and sintered at 1450 °C for 6 h in a CO_2, atmosphere. The final pellet density determined by water immersion was 95 % of theoretical density. For the IMF-CO-process microspheres with the target composition were produced by internal gelation, dried at 200 °C and calcined at 550 °C in an argon atmosphere. The calcined spheres were crushed by an automatic mortar and milled in an attrition mill to a fine powder. Granulation and pelletisation of this material was carried out using the same conditions as in the IMF-ATT-process. The green pellets were sintered at 1750 °C for 6 h in a 8% H_2 / N_2 atmosphere. The pellet density determined by water immersion was 86 % of theoretical density. The mircrostructure of pellets prepared from dried and milled powders showed large pores up to 20 μm and an irregular microstructure [41].

Summary

The impact of the calcination temperature on the compressibility and sintering ability of pellets was investigated in detailed. After the synthesis by co-precipitation and grinding by attrition, the powder consists of "soft" agglomerates and "hard" agglomerates with irregular shapes.

The powders after low-temperature treatment, from 110 °C up to 600 °C, presented the best sinterability. Their small mean crystallite size (L) and high-level of lattice distortions ($<\varepsilon^2>^{0.5}$) determine their high activity during sintering process. However, at low calcination temperatures (110 and 350°C) the powders have a short optimal pressure zone due to the presence of a large quantity of water. After a calcination at 800°C and higher, the recrystallisation process takes place and leads to agglomerates hardening. The powders consist then of a majority of coarse hard agglomerates which lead to low density products.

Dilatometry studies have demonstrated that the hard agglomerates control the sintering. They sinter at low temperatures (from 900 to 1230°C) and then form a "rigid" skeletal structure

which is hampered by the sintering of „soft" agglomerates at higher temperature. This sintering behaviour leads to the formation of pores along the grain boundaries and not fully densified microstructures.

Therefore, to avoid the limitation of the sintering ability of powders by the "hard" agglomerates and to avoid defects in pellets because of the inhomogeneity of powder [111], it seems interesting to eliminate the coarse hard particles. This is proposed to be done by a fractionating method.

7.4. Fractionation of powders: influence on the powders and pellets properties

After grinding by attrition a fractionation step was performed in acetone on 10-Ce-YSZ powders calcined at different temperatures.

The weight fraction of the fine powder strongly depends on the calcination temperature. So, after calcination at 110 °C, the fine powder fraction is 66 % as against 40 % after calcination at 600 °C. However, when the powder is calcined at 800°C, the fine powder fraction drastically decreases to 8 %. This is a consequence of the increase of agglomerates strength during the recrystallisation of material. Therefore, additional fractionating of fine agglomerates has a practical sense only for powders after low-calcination temperatures (from 110 to 600°C).

In order to determine the impact of the fractionation step on the powders behaviour and pellets properties, the powders characteristics, compressibility, sinterability and densification behaviour were studied in details.

7.4.1. Characterisation of the powders

Fine powders were produced by the fractionation method described. The investigation of powder mass distribution by laser granulometry has shown that, after fractionating, the cumulative mass distribution ranges up to 10 µm, and 95 wt.% of the agglomerates have an equivalent diameter of less then 4 µm (Figure 47). The average agglomerate size is equal to 0.9 µm. The agglomerate size distribution has three maximums at around 0.3, at 0.8 and 2.7 µm, which may correspond to different agglomeration levels of the primary particles.

The structure of the powder was also studied by SEM revealing different structure depending on the calcination temperature. Powder calcined at 110 and 350°C consists of hard and soft agglomerates of different sizes while powders calcined at 600°C mainly consists of soft agglomerates. In fact, the hard agglomerate strength increases with the calcination temperature. During "mild" grinding by attrition of powders calcined at 110 and 350°C, the hard agglomerates easily broke down during the grinding step and concentrated in fine powders. On contrary, after calcination at 600°C, because of the highest value of the agglomerates strength and the crystallisation of material, the "soft" agglomerates mainly broke down. And, due to their lower effective density compared to the hard agglomerate, they concentrate in fine part powder fraction.
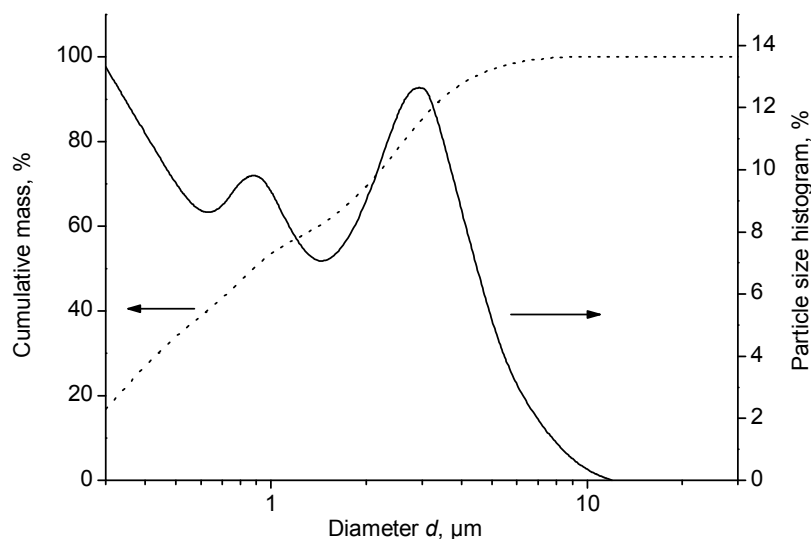
Figure 47. The agglomerate size distribution for 10-Ce-YSZ powder calcined at 600°C, ground and fractionated in acetone.

7.4.2. Compressibility of the powders

The compressibility of fractionated powders was investigated in details, and the relative green density of the pellets was determined as a function of the pressure.

Powder calcined at 110 and 350 °C have the same compressibility behaviour than ground powders (Figure 48a). In the present case, the biggest particles are the hard agglomerates and the value of their agglomerate strength P_Y are 380 MPa in the case of 110°C dried powders to 510 MPa for powders calcined at 350°C. The value of P_Y slightly decreases with the fractionation. In fact, in ground powders, P_Y is the agglomerate strength of the coarse hard agglomerates, while the P_Y defined here represents the agglomerate strength of small hard agglomerates. Like in the case of ground powders, two types of packing occur in the powders. The presence of a large amount of hard agglomerates inhibit the possibility of a homogeneous packing in the complete range of pressure.

On contrary, the 600°C calcined powders exhibit a different behaviour. The relative green density of the pellets linearly increases with the pressure from 0.50 to 0.56 TD (Figure 48b). Contrary to the ground powder, no bend is detected at around 840 MPa, letting suppose that only one type of packing occurs in the material. SEM investigations of fractured green bodies, pressed at 650 and 1020 MPa had shown that in both cases, agglomerates are homogeneously packed (Figure 49). Moreover, it should be noticed that some hard agglomerates remains in the green body.
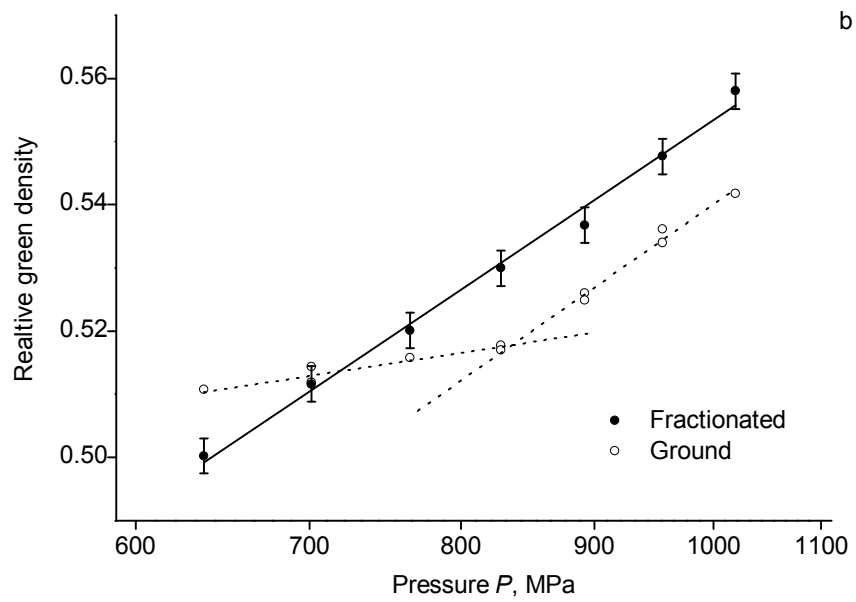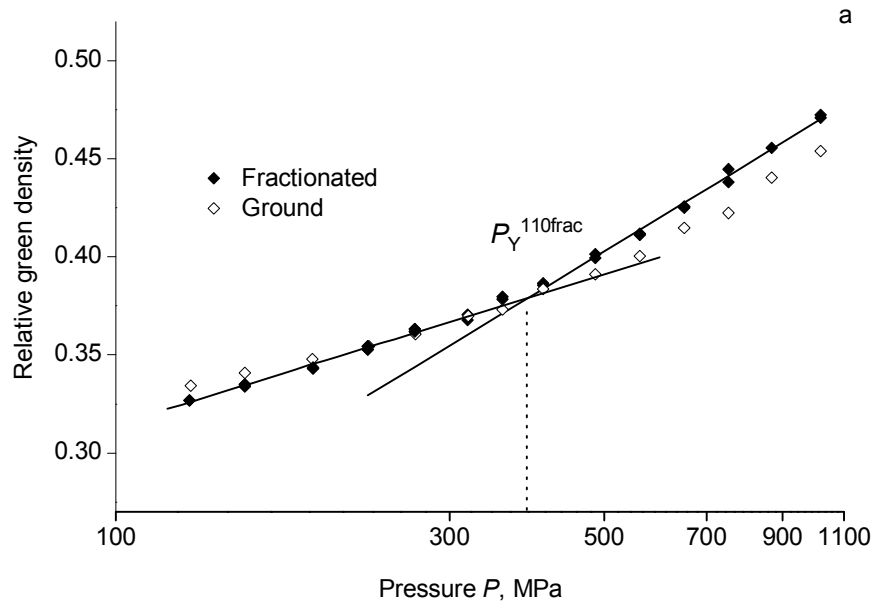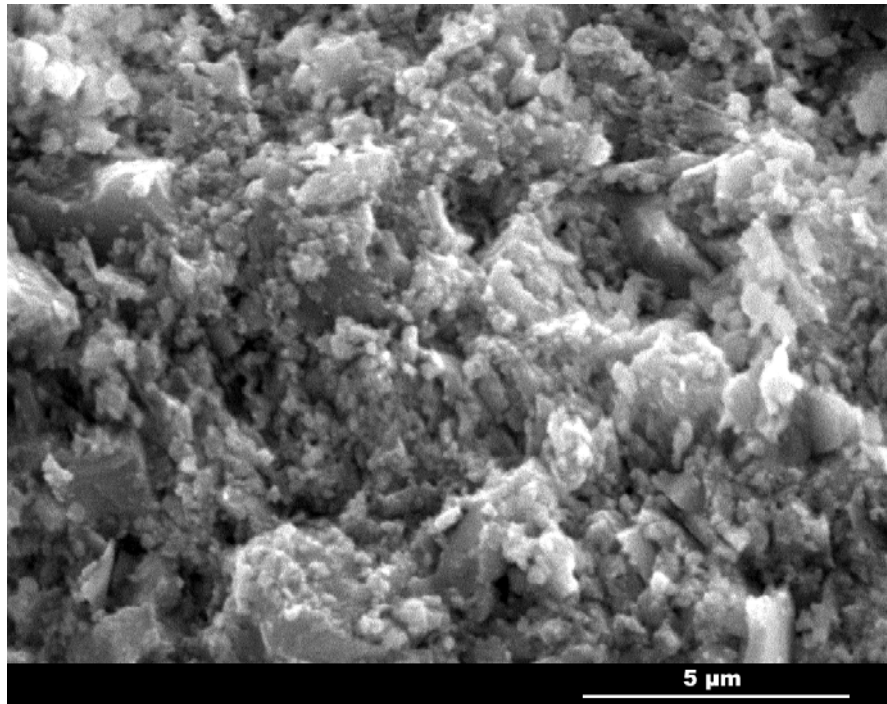
Figure 48. The relative green densities of pellets made from fractionated powders after calcination at 110 (a) and 600°C (b) as a function of the pressure.

Figure 49. SEM photographs of fractured green bodies made from 10-Ce-YSZ fractionated powders after calcination at 600°C.

7.4.3. Sinterability of the pellets

After cold uniaxial compaction, pellets were then sintered at 1600°C for 5 hours. Their relative sintered density were determined as a function of the pressure (Figure 50).

Like in the case of ground powders, pellets prepared from 110 or 350 °C calcined and fractionated powders are sensitive to the under and over pressure. However, the region of the optimal compacting pressure (P_{opt}) is extended and shifted to higher pressure. Thus, for dried powder the optimal pressure region is located between 350 and 550 MPa reaching densities up to 0.950 TD. Powders calcined at 350 °C have an optimal pressure region between 500 and 800 MPa reaching densities up to 0.955 TD. Powders calcined at 600°C have no pressure dependence at high pressure and reach values of 0.960 TD.

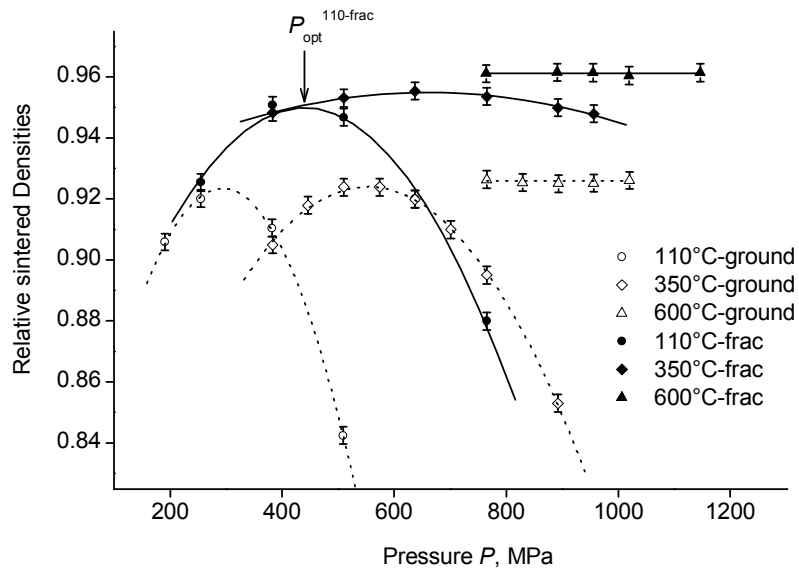For all powders, the fractionation step has allowed an increase of density (Figure 51).

Figure 50. The relative sintered densities of pellets made from ground (open) and fractionated (full) powders as a function of the pressure and the calcination temperature.
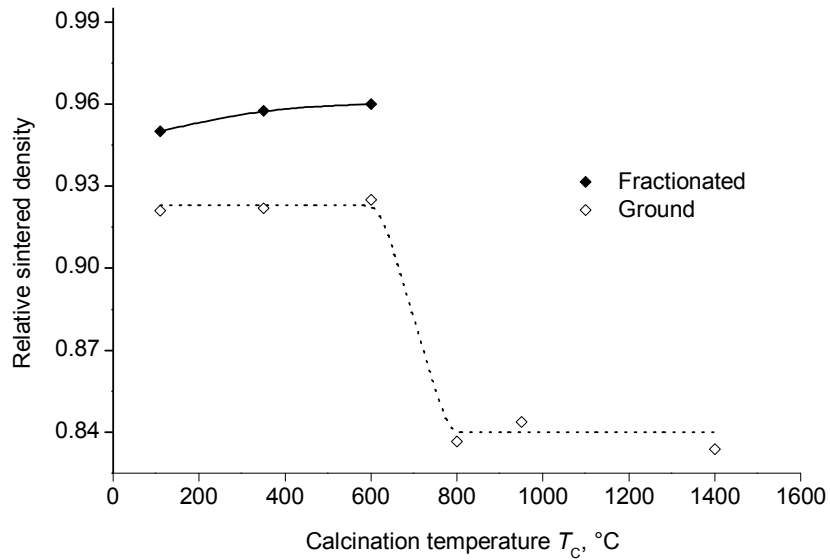

Figure 51. The relative sintered densities of the best pellets made from ground (open) and fractionated (full) powders as a function of the calcination temperature.

7.4.4. Densification behaviour and microstructure of the pellets

The density evolution of pellets made from fractionated powder was also studied by dilatometry. The pellet have different behaviour as a function of their calcination temperature. The relative density and densification rates of 10-Ce-YSZ pellet made from 600°C-calcined powders, as a function of the temperature, are reported in Figure 52. In this case, like in the case of ground powders, the sintering also starts at 900°C and then the density continuously increases between 900 and 1450°C. Only minor decrease of densification rates is observed above 1450°C.
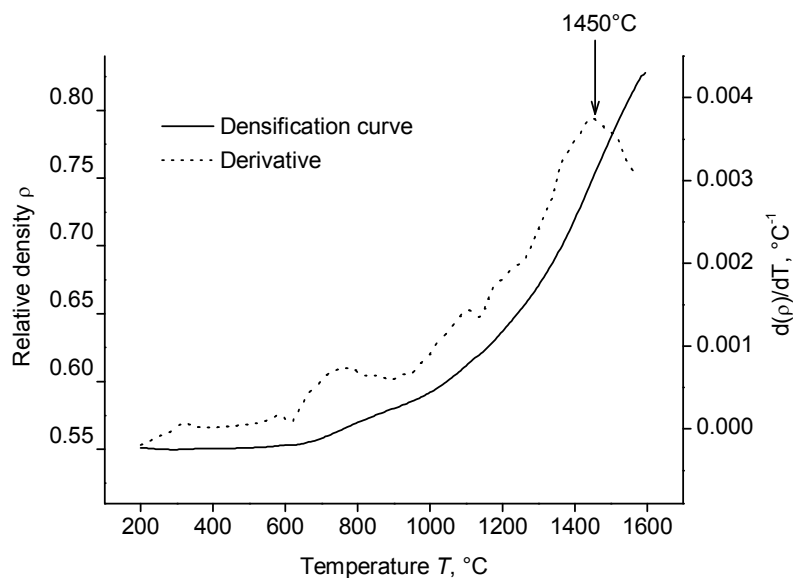
Figure 52. Evolution with the annealing temperature of the relative density ρ (full line) and its derivative $d(\rho)/dT$ (dotted line) of 10-Ce-YSZ pellet, made from 600°C calcined and fractionated powder.

Sintered pellets microstructure was investigated by SEM. As seen on Figure 53a, the pellets have a homogeneous microstructure with well distributed pores over the pellet. Moreover the absence of coarse „hard" agglomerates in the powder after fractionating leads to the absence of large pores in the sintered material (Figure 53b). Therefore, in this case, fine powders and "soft" agglomerates have similar sintering behaviour and the sintered material possesses a dense structure, well-formed grains and boundaries and homogeneously distributed submicron pores, Figure 53b.
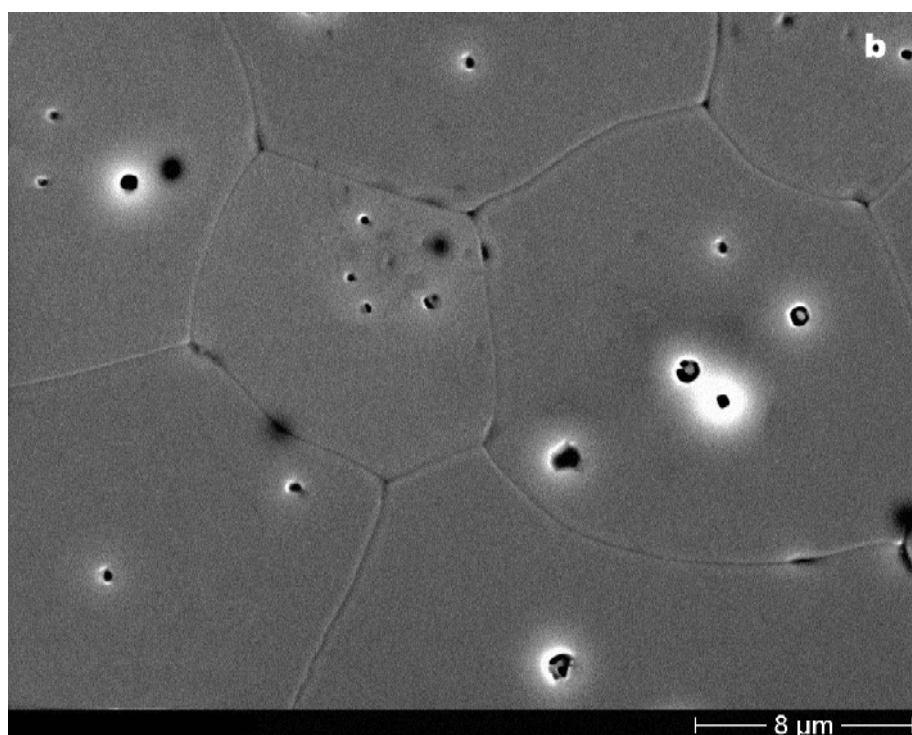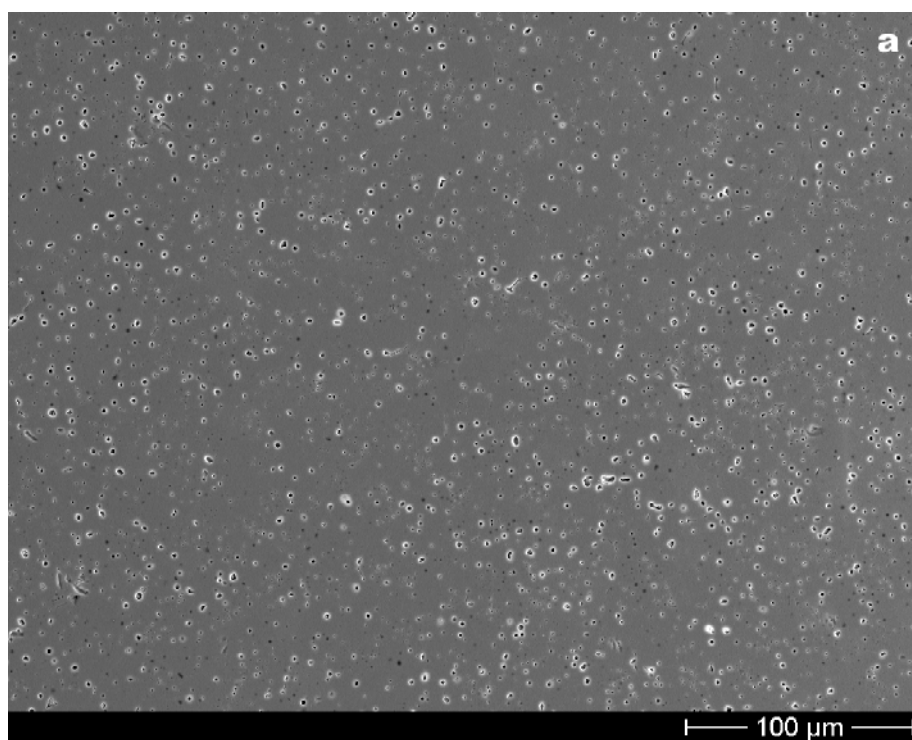
Figure 53. SEM photographs of 10-Ce-YSZ pellets made from ground and fractionated powder, that was calcined at 600°C. Pellets were sintered at 1600°C for 5 hours.

Similar results were presented in the work of Van de Graaf et al [54] and in the work of Shi et al. [112]. Powders consisting of soft agglomerates have a homogeneous sintering and higher densities compared to powders consisting of hard agglomerates. The microstructure of pellets is also characteristic. Pellets prepared from powders containing hard agglomerates show a lower density and very large slit-like voids while pellets prepared from soft agglomerates have a more homogeneous microstructure and sub-micron pores.

The densification behaviour of pellets made from 110-350°C-calcined powders was also studied by dilatometry. As reported in Figure 54, the densification behaviour can be divided in 3 regions as a function of the annealing temperature. In the first region, from 200 to 500°C, the density of pellets increases. This can be associated with the elimination of water from material which is responsible for a strong decrease of the pellets volume. When the temperature increases from 500 to 1000 °C, the pellets show a linear densification behaviour, which is associated with the material crystallisation and subsequent elimination of crystal water followed by a recrystallisation step. At the temperature of 1000 °C, the sintering process starts and the density increases up to 1600°C.

The sintering of material occurs in two steps (Figure 55): from 1000 to 1300°C with a maximum at 1230 °C, what corresponds to the densification of the hard agglomerates, and from 1300 to 1450°C, corresponding to the densification of the soft agglomerates. A minor decrease of densification rates is observed above 1450°C.
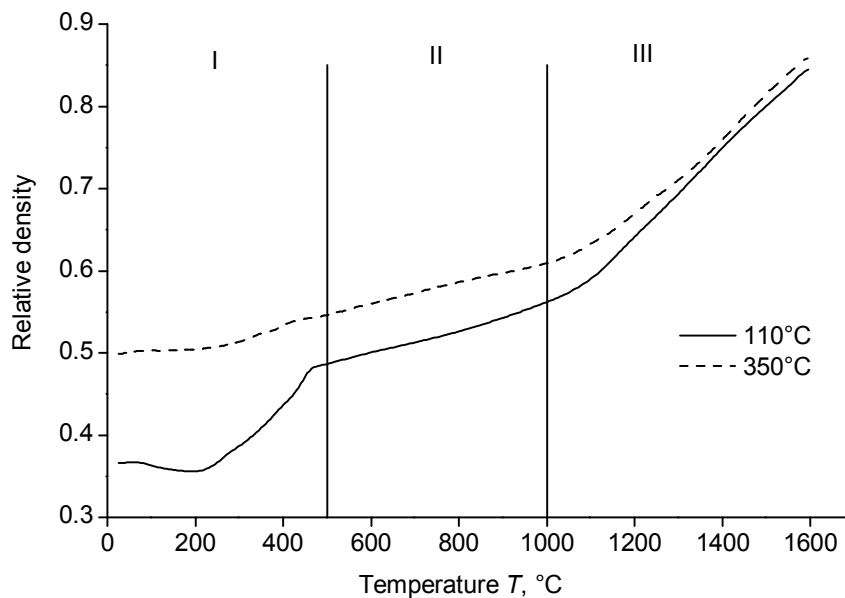

Figure 54. Evolution with the annealing temperature of the relative density ρ of 10-Ce-YSZ pellet, made from 110 and 350°C calcined and fractionated powders.
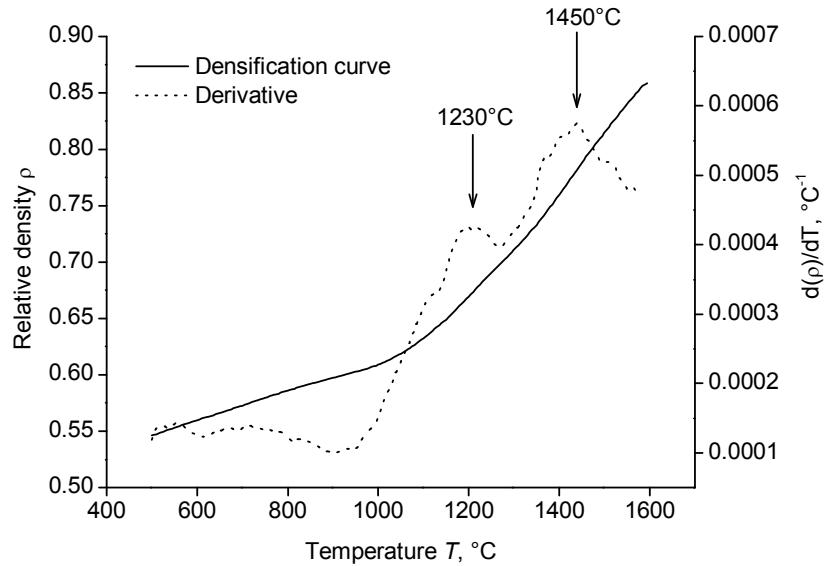
Figure 55. Evolution of the relative density ρ (full line) and its derivative $d(\rho)/dT$ (dotted line) of 10-Ce-YSZ pellet, made from 350°C calcined and fractionated powders in the temperature range from 500 to 1600°C.

The microstructure of pellets was investigated by SEM. As seen in Figure 56 pellets made from dried powders, have an inhomogeneous structure, which is differentiated in porous and high-density regions. The high-density regions are homogeneously shared over the pellet and represent ~ 40 vol. % in the material. They have an irregular elongated shape with almost linear boundaries (Figure 56a). These regions have very well-formed grains, practically without pores. Moreover, an interesting effect was observed: these high-density regions are not delimited by grain boundaries (Figure 56b). The porous regions, are composed from grains with curved boundaries, synonym of a non complete sintering. Moreover, the concentration of large pores inside the grains is relatively high. These pores can be closed only by volume diffusion. Moreover, in those regions, elongated pores are located at the grain boundaries. Pellets made from 350°C-calcined powders have the same microstructure.
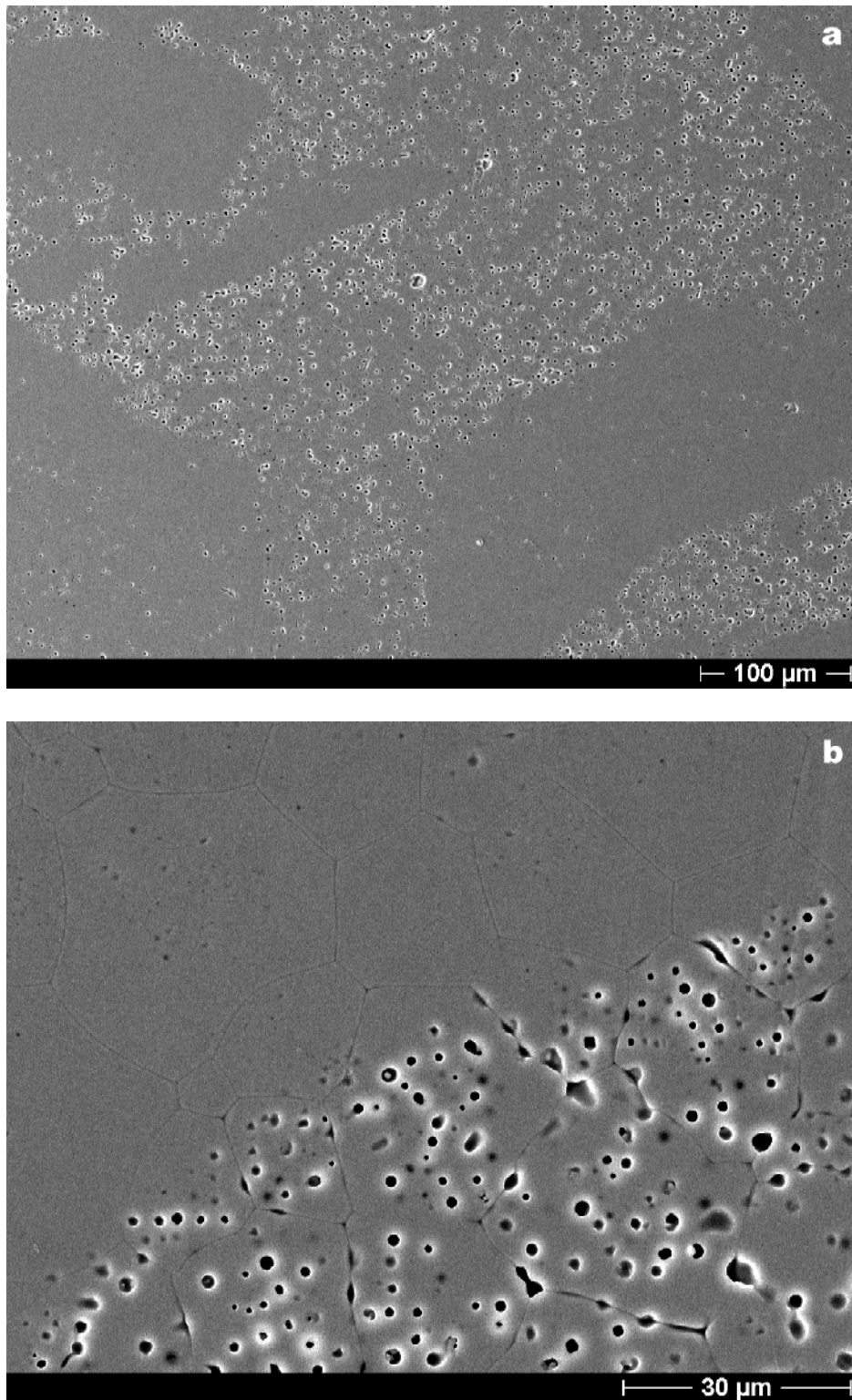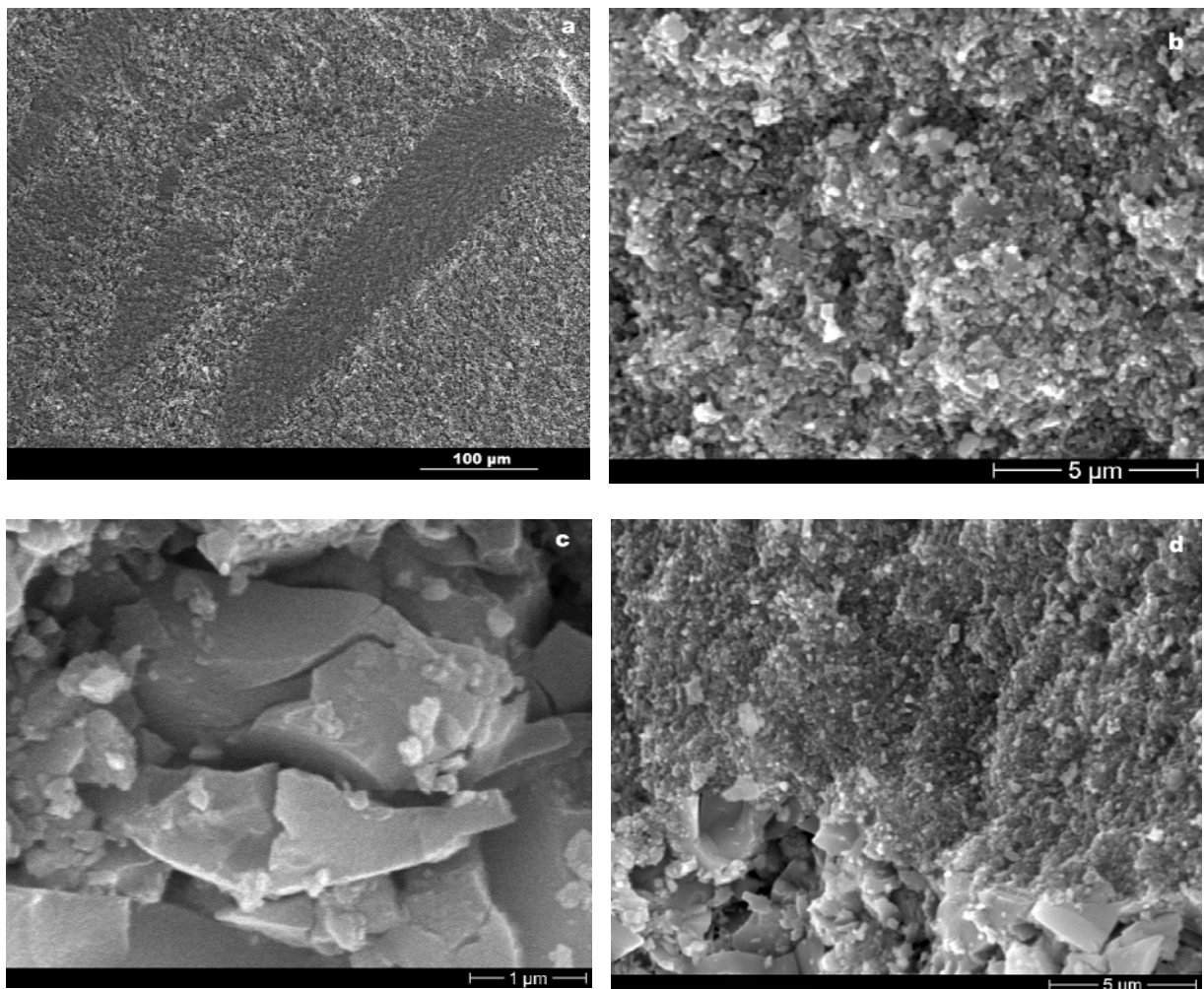
Figure 56. SEM photographs of 10-Ce-YSZ pellet made from dried and fractionated powder.

In order to understand why pellets made from dried fractionated powders have an inhomogeneous microstructure, the green body of pellet was investigated by SEM. After pressing, the pellet already composed from different regions with linear boundaries (Figure 57a). The delimited regions are composed from well packed soft agglomerates with a

size less than 1 μm (Figure 57b). They will densify homogeneously and form the dense regions observed in the sintered body (Figure 56a). The other part of the green body, is mainly composed from hard agglomerates (Figure 57c). The hard agglomerates will rapidly sinter at temperatures lower than 1230°C, forming a rigid skeletal structure. The soft agglomerates will sinter in between this structure, but they are not numerous enough to fill completely the space involving the presence of large pores inside the grains. These pores can be closed only by volume diffusion process. The different sintering behaviour between hard and soft agglomerates will create elongated pores at the grain boundaries. These regions will become porous regions (Figure 56a, b).

The junction between the both regions is made by the soft agglomerates of the both regions (Figure 57d). They will sinter together entrapping the big agglomerates, forming grains. which will grow independently of the pores between the hard agglomerates (Figure 56b).

Figure 57. SEM photographs of fractured green body of 10-Ce-YSZ pellet compacted from dried and fractionated powder.

In fact, after fractionation, the flask containing the solution of fine powder in acetone was placed in an oven at 80 °C for the evaporation of the solvent. During this step, the hard agglomerates additionally form a deposit at the bottom of the flask and the ultra fine powder remains at the surface. During drying, it aggregated and formed a layer at the surface. After the evaporation step, the powder was softly blended and then pressed. However, some non-completely destroyed part of this layer, composed from only well packed soft agglomerates, still remained in the powder and was pressed directly, without having being prematurely broken. Thus, in the case of dried powder, the difference of the densification behaviour between soft and hard agglomerates is at the origin of the non homogeneous microstructure.

The origin of the dense and porous regions comes from the presence of non completely fragmentised regions of soft agglomerates. To improve the packing of material by crashing these regions and dispersing the soft agglomerates between the hard agglomerates, a pressing by repressing can be employed. Thus, 10-Ce-YSZ powder dried at 110°C and fractionated in acetone was pressed by repressing 4 times and sintered at 1600°C for 5 hours. The surface of pellets was investigated by SEM (Figure 58). Only in the case of 4 pressings, the pellet showed a complete homogeneous microstructure, with pores well shared over the surface. However, big pores as well as some micro-cracks , coming from the sintering of the hard agglomerates, are unfortunately still present on the surface.
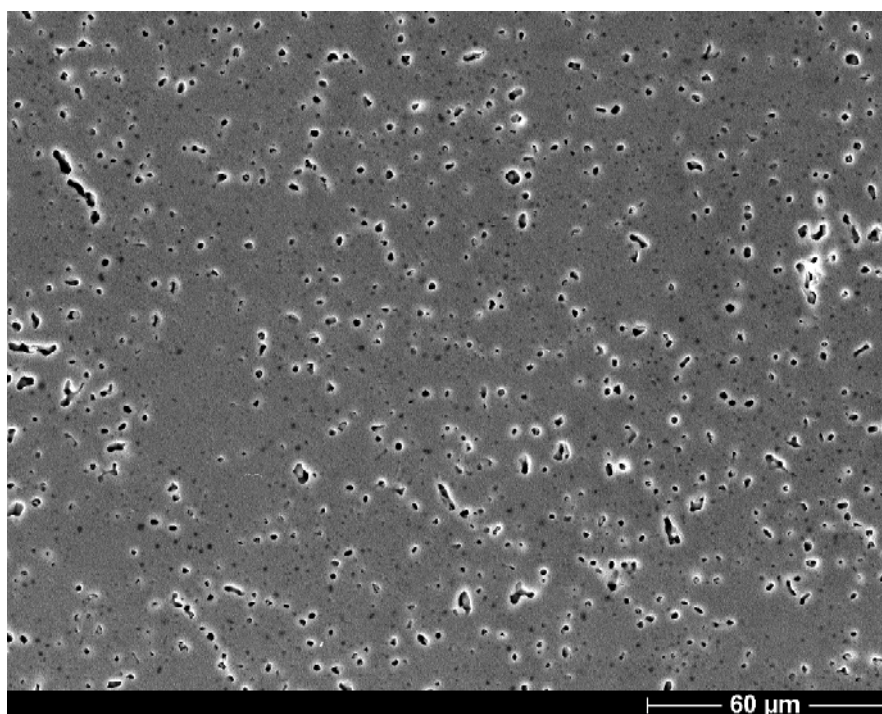
Figure 58. SEM photographs of 1600°C sintered 10-Ce-YSZ pellet, made from dried and fractionated powder, and compacted by a quadruple repressing.

In order to get a homogeneous powder after fractionation, the extra aggregation of fine particles should be avoided. It is suggested to perform the elimination of solvent by rotary evaporator. However, it should be noted, that, even if the green body is homogeneous, the presence of hard agglomerates in the powder would certainly lead to a microstructure similar to that obtained in the case of ground powder but with higher density.

Summary

In order to avoid the presence of coarse hard agglomerates in the powder, a fractionation step was performed after grinding. The fractionated powder contains agglomerates with an equivalent diameter less than 4 µm. However, this action has a practical sense only in the case of powders calcined at temperatures from 110 to 600°C.

The impact of the fractionation step on the sinterability of powders was studied in details. The addition of a fractionation step has allowed to increase the sintered density and to enlarge the optimal compacting pressure zone and shift it to the highest pressures.

In the case of just 110 °C dried or 350°C calcined powders, the powders still consists of soft and hard agglomerates, after fractionation. The obtained microstructure is inhomogeneous, due to an extra-segregation of soft and hard agglomerates during the evaporation of solvent. A homogeneous microstructure can be obtained employing a quadruple repressing method. However, the presence of hard agglomerates in the powder still limit the sinterability and is responsible of the presence of elongated pores along the grain boundaries.

On contrary, powders calcined at 600°C mainly consist of soft agglomerates and sinter homogeneously. Pellet with density of 0.96 TD and homogeneous microstructure are obtained. Thus, it has been decided to study the influence of ceria content on the properties of YSZ matrix on pellets made from 600°C calcined powder that has been fractionated.

7.5. The physico-mechanical properties of Ce-YSZ ceramics

Ce-YSZ powders with ceria concentration from 5 to 50 wt.% were synthesised by co-precipitation method. After a calcination at 600°C followed by a fractionation in acetone, the powders were compacted and sintered at 1600°C for 5 hours.

7.5.1. Compressibility and sinterability of the material

For a fixed applied pressure, the powder compressibility does not depend on the ceria content, because the same methods of powders synthesis and preparation were employed before compaction. The relative green density increases with increasing pressure. At a pressure of 890 MPa, for all ceria concentration the density reach a value of 0.53 of the theoretical density (TD) (Figure 59). This values of green densities is quite low and comparable with literature data for nano-sized ceramic materials [113, 114].
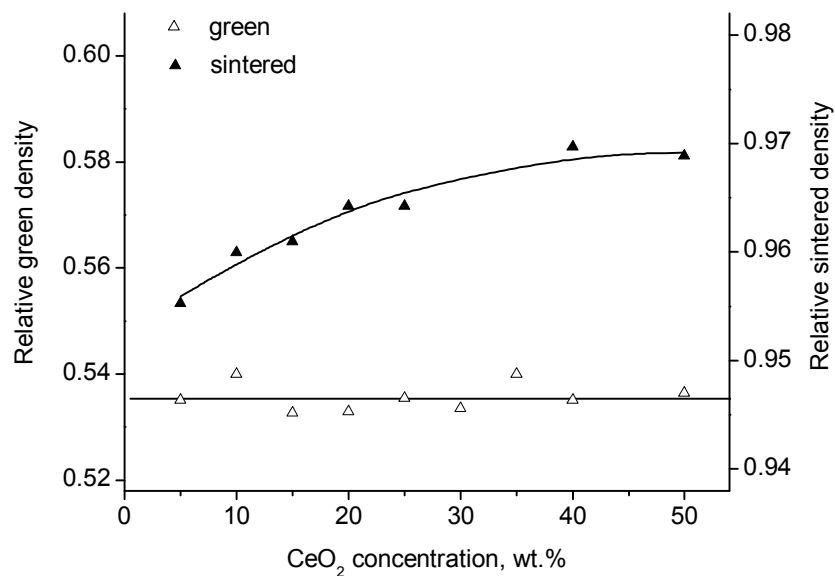
Figure 59. Evolution of the relative green and sintered density of Ce-YSZ pellets made from 600°C calcined and fractionated powder, as a function of ceria.

For all ceria concentrations, the sinterability of powders after calcination at 600 °C is not dependent on pressure at higher pressures, like in the case of 10-Ce-YSZ illustrated on Figure 50. Pressures higher than 750 MPa can therefore be chosen as optimal compacting pressures. However, the density slightly increases with the addition of ceria from 0.955 to 0.969 TD, Figure 59.

The influence of CeO_2 addition on the properties of $(Zr,Y,Ce)O_{2-x}$ pellets was already investigated by Fernandez et al. [56, 58]. $(Zr,Y)O_{2-x}$ microspheres produced by sol-gel methods were infiltrated by cerium nitrate solution and then calcined at 850 °C for 2 hours. The maximal cerium content was 40 wt.%. Compact materials were produced by the cold bi-axial pressing method at 480 MPa and sintered at 1650 °C for 6 hours. Contrary to our results, the addition of cerium in these reported investigations [56, 58] showed a significant decrease of density from 0.92 to 0.87 TD. However, it has been demonstrated in our work, that powders calcined at high calcination temperature should be compacted at high pressure (~ 800MPa) to obtain pellets with good and reliable properties. The low pressure used for the compaction of the kernels may be at the origin of the poor sinterability of pellets.

7.5.2. Microstructure of the pellets

The surface of the pellets pressed at optimal pressure was investigated by SEM.

For all ceria contents, the pellets show a homogeneous structure, well-formed grains and boundaries and uniformly distributed pores (Figure 60a,b).

109

The pellets with high concentration of ceria present larger grains and sharper grain boundaries (Figure 60b). The grains have quite rectilinear boundaries, sometimes hexagonal, characteristics of the cubo-octahedral particles. Pores are mainly located at the triple junction and along the grain boundaries, revealing the presence of remaining hard agglomerates in the powder.
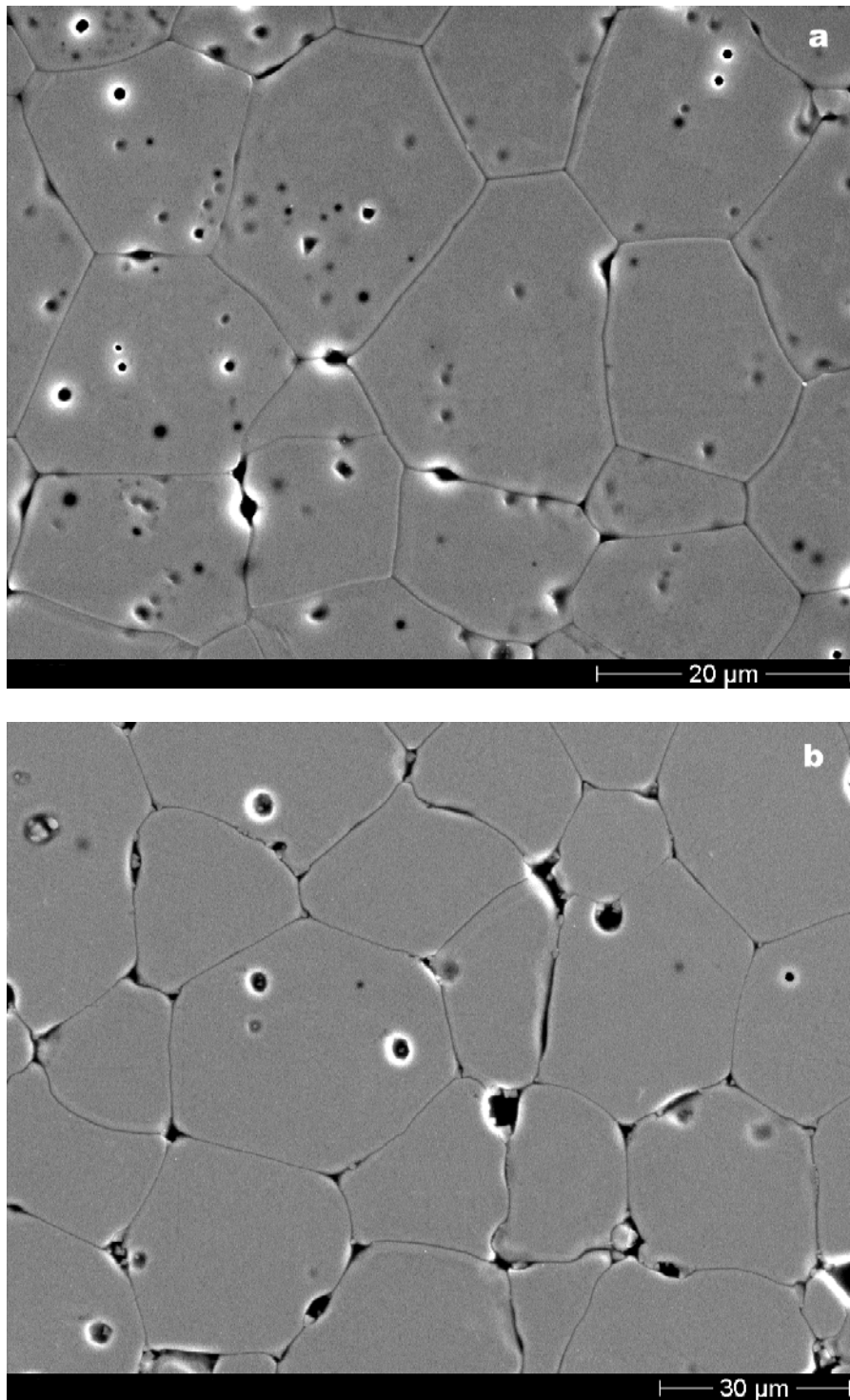
Figure 60. SEM photograph of polished surface of 20-Ce-YSZ (a) and 50-Ce-YSZ (b).

The average grain size of the pellet was determined for pellets fabricated from powder calcined at 600°C. It first slightly increases from 14 to 16 µm when the ceria concentration increases up to 25 wt.% and then strongly increases up to 30 µm when the concentration reach 50 wt.% (Figure 61). The change in behaviour correlated with the fact that the Ce-YSZ system present different behaviour function of the ceria concentration. For concentration less than 25 wt.% the properties of the system are mainly controlled by the YSZ matrix. This border could be shown.
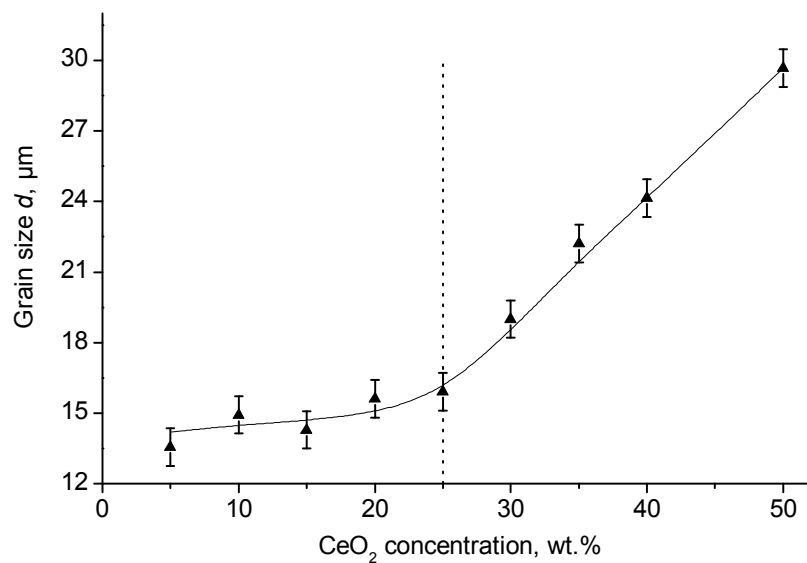
Figure 61. Dependence of the grain size of Ce-YSZ pellets with the ceria content.

7.5.3. Mechanical properties of the pellets

For the best pellets, the influence of ceria concentration on the mechanical properties, such as microhardness (H_V) and fracture toughness (K_{IC}), was investigated.

To determine the optimal load for microhardness measurements, the microhardness of the 10-Ce-YSZ pellet prepared from 600°C calcined powder, was measured as a function of the applied load. The curve, reported on Figure 62, shows a maximum at 2N, the load chosen as optimal for our system.
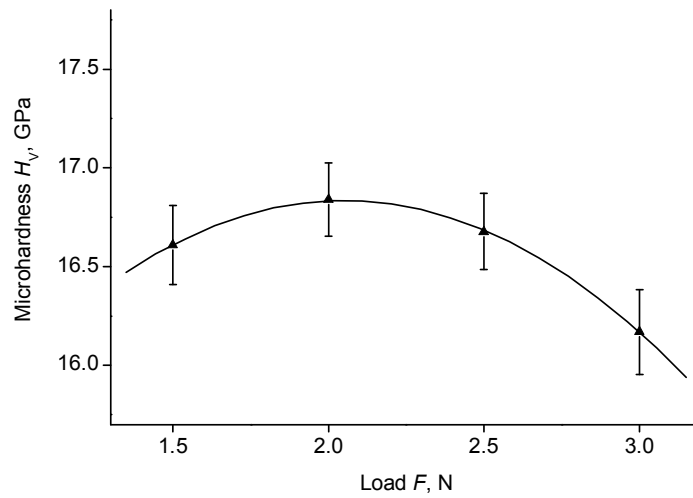
Figure 62. Determination of the microhardness of 10-Ce-YSZ pellet, made from 600°C calcined and fractionated powder, as a function of the applied load.

For each sample, nearly 50 microhardness measurements were performed along a pellet's diameter with a constant interval of $\sim 100\ \mu m$. A typical Vickers indenter photograph is reported on Figure 63. In the concentration range from 5 to 25 wt,%, the value H_V shows no dependence on the addition of ceria and remains constant at 16.65 GPa (Figure 64).
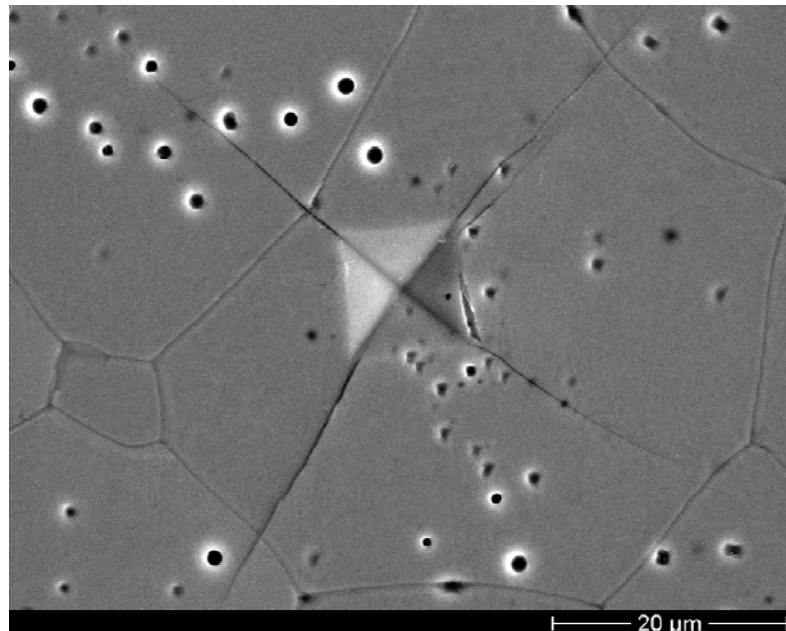
Figure 63. SEM photographs of a Vickers indenter on 40-Ce-YSZ pellet.
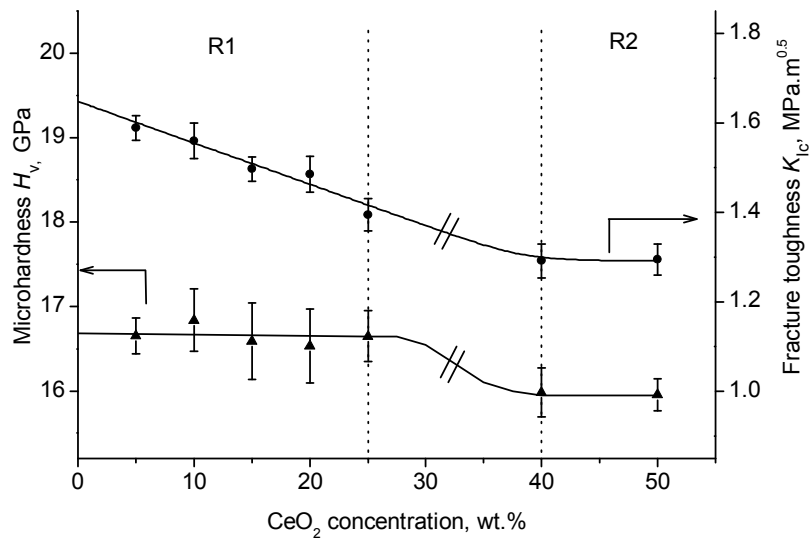
Figure 64. Evolution of the microhardness and the fracture toughness of the Ce-YSZ pellets as a function of the ceria content.

According to the literature data, high-density YSZ ceramics have a microhardness of 17.6 GPa [115]. According to the work of S. Maschio et al. [116], a ceramic of pure CeO_2 with a density of 0.94 TD has a microhardness of 3.9 GPa. Since both systems have a similar crystal structure, it is supposed that the addition of ceria in the YSZ matrix will decrease the mechanical properties of the matrix [116]. However, the addition of ceria leads to an increase of sintered pellet density (Figure 59). Furthermore the microhardness of the material increases with increasing density [85]. So, for ceria content from 5 to 25 wt.%, the negative effect of ceria addition on the microhardness would be compensated here by the positive effect of increasing the pellet density.

For higher concentration ([CeO_2] $\geq$ 40 wt.%), the microhardness decreases up to 15.95 GPa even if the density of pellet increases. This decrease of microhardness can be correlated to the increase of grain size observed in this region [117, 118] With 40 wt.% of ceria, the Ce-YSZ has already changed its behaviour.

The fracture toughness K_{IC} was also estimated for the same pellets. During the microhardness measurement, cracks go over grain boundaries and pores (Figure 63). For ceria content from 5 to 25 wt.%, the fracture toughness (K_{IC}) linearly decreases with the addition of ceria from 1.59 to 1.37 $MPa.m^{0.5}$ (Figure 64). For ceria concentration higher than 40 wt.%, the fracture toughness decreases up to 1.29 $MPa.m^{0.5}$ and remains constant. This effect can be correlated to the microstructure and the decrease of H_V with the increasing of ceria concentration. The border defined at 25 wt.% remains also here.

The extension of our data to the fracture toughness of pure YSZ and pure CeO_2, correlate with the data obtained in the case of YSZ high density ceramics, single crystal, and films [86, 115] and a pellet of 0.94 TD [116] respectively.
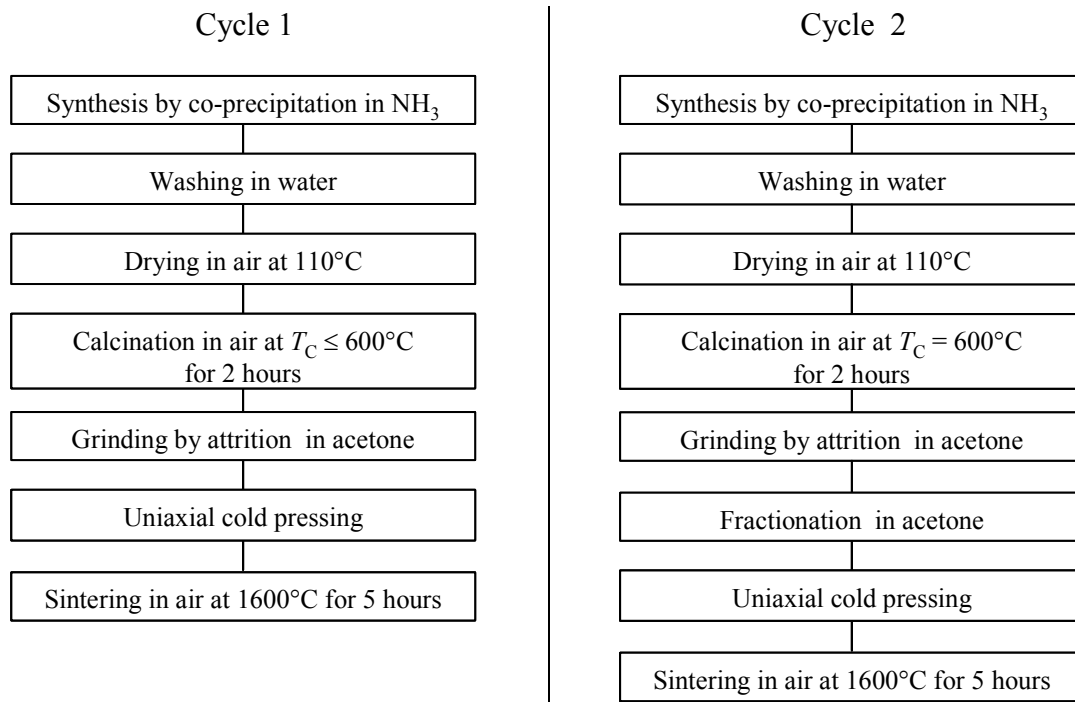
In a previous work, pellets with different ceria contents were prepared from 600°C calcined ground powders [119]. In that case, the density of the pellets increased with increasing ceria concentration from 0.87 up to 0.93 TD, with a stable zone at 0.93 TD in the range from 10 to 20 wt.%. The microhardness of those pellets was determined and was located between 11 and 13 GPa. The data correlate with the data presented in the work of Lee. et al. [120]. The authors prepared $(Zr_{0.68}Y_{0.10}Er_{0.07}Ce_{0.15})O_{1.915}$ pellets by dry powder milling method [50], with densities of 88 and 92 %TD. Both pellets exhibit a microhardness of 6.6 and 7.6 GPa and a fracture toughness of 1.7 and 0.8 $MPa.m^{0.5}$, respectively.

The addition of the fractionation step has increased the density but also improved the quality of the microstructure. Both facts are responsible for the improvement of the mechanical properties.

7.6. Conclusion

YSZ is proposed as inert matrix for the immobilisation of actinides. In order to determine the impact of the tetravalent actinides addition, simulated in this work by ceria, Ce-YSZ system was investigated for a complete range of ceria. This system crystallise at high temperature in a stable solid solution, fcc, fluorite type structure, without apparent segregation of ceria. The system follows the Vegard's law for the complete range of ceria. The Ce-YSZ system can be divided in 2 regions as a function of the ceria concentration: for $[CeO_2]$ from 0 to 25 wt.%, the Ce-YSZ follows the properties of YSZ material. In a second region for $[CeO_2]$ from 40 to 100 wt.%, the Ce-YSZ follows the properties of CeO_2 material. Ce-YSZ pellets with stable and reliable properties were fabricated employing different synthesis routes (Figure 65). Ce-YSZ pellets with densities of ~ 0.92 TD and homogeneous repartition of pores over the surface can be obtained in the case of Cycle 1. In this case, 110 °C dried and 350°C calcined powders are extremely sensitive to under and overpressing. On contrary, when powders were calcined at 600°C, the system has no pressure dependence at high pressure. Unfortunately, the powders contain a lot of hard agglomerates that control the sintering and limit the density, the quality of grain boundaries and so the properties.

The addition of a fractionation step after grinding by attrition (Cycle 2) was envisaged to obtain powders with agglomerates sizes less than 4 μm and free of coarse agglomerates. It enlarges the optimal pressure zone and improves the sinterability of pellets. Thus, Ce-YSZ pellets prepared from powders calcined at 600°C have a good sinterability and reach densities up to 0.97 TD. Contrary to the results found in the literature, ceria addition has a positive impact on the sinterability of pellets. For all ceria content, the microstructure is homogeneous, free of big and larges pores. The pellets have good mechanical properties.

114

Cycle 1

| Synthesis by co-precipitation in NH_3 |
| Washing in water |
| Drying in air at 110°C |
| Calcination in air at $T_C \leq 600$°C for 2 hours |
| Grinding by attrition in acetone |
| Uniaxial cold pressing |
| Sintering in air at 1600°C for 5 hours |

Cycle 2

| Synthesis by co-precipitation in NH_3 |
| Washing in water |
| Drying in air at 110°C |
| Calcination in air at $T_C = 600$°C for 2 hours |
| Grinding by attrition in acetone |
| Fractionation in acetone |
| Uniaxial cold pressing |
| Sintering in air at 1600°C for 5 hours |

Figure 65. Summary of the employed technical cycle for the synthesis of the Ce-YSZ ceramics.

8. Thoria: quasi-inert matrix for the immobilisation of actinides

8.1. Introduction

ThO_2 has also been foreseen as an attractive matrix for the immobilisation of actinides, particularly plutonium. Such as YSZ matrix, the system ThO_2-CeO_2 should be characterised and the possibility of pellets fabrication using simple methods investigated. Thus, ThO_2-CeO_2 powders with different ceria concentrations were synthesised by the co-precipitation method. Thermal and crystallisation behaviour of the powders were first investigated. The fabricated pellets were characterised and their physico-mechanical properties investigated as a function of the cerium concentration.

8.2. Physical properties of ThO_2-CeO_2 powders

8.2.1. Themal behaviour of the powders

After synthesis and drying at 110 °C, the thermal behaviour of powders containing up to 75 % ceria was investigated by TG-DSC in air atmosphere. All powders show similar behaviour. As represented in Figure 66 for the case of 50 % ceria, the thoria-ceria powder shows a two-step mass loss (8.15 %) from 25 to 670 °C. In the temperature range from 25 to 380 °C, the mass loss (5.20 %) is accompanied by a heat consumption corresponding to the elimination of adsorbed and crystal water and impurities. From 390 (T_I) to 680 °C (T_F) a second endothermic effect with a minimum at 495 °C (T_M) and an enthalpy $Q = -65.5$ J/g is observed on the DSC curve. This effect is accompanied by a second significant mass loss (2.95 %). Heating at temperatures higher than 1075 °C (T_S) is necessary to stabilise the mass.

Moorehead and McCartney [121] also studied the thermal decomposition of thorium hydroxide in nitrogen, obtained by precipitation of $Th(NO_3)_4$ with NH_4OH. They also found endothermic peak in the range of 400 to 700 °C associated to a reduction of mass. These endothermic peak are correlated to the decomposition of Thorium hydroxide.
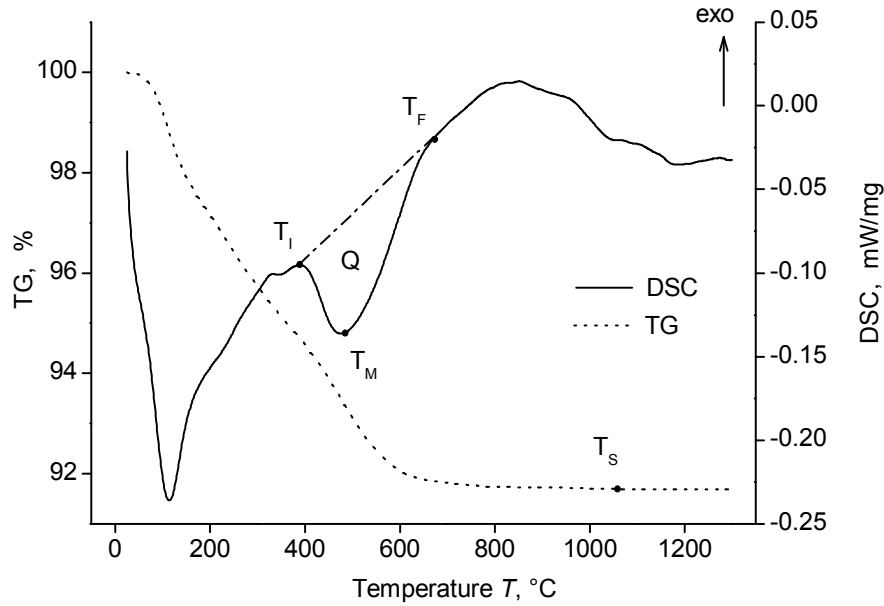
Figure 66. TG and DSC curves of ThO$_2$ -50 CeO$_2$ powder in air atmosphere.

The effect of the addition of ceria is clearly observed on the characteristic parameters (T_I, T_M, T_F, T_S, and Q) of the system (Figure 67). As defined in the case of 50 % ceria (Figure 66), T_I, T_M, and T_F correspond to the temperature of the beginning, the minimum, and the end of the second endothermic peak, respectively. T_S is the temperature of the stabilisation of mass and Q the enthalpy of the second endothermic peak. If T_F remains constant at around 680 °C, T_I and T_M first slightly decrease up to a ceria concentration of 20 % and then decrease tending to the values of pure ceria. Simultaneously, the intensity of the endothermic peak Q also decreases from -13.08 to -79.90 J/g with ceria addition, following the same behaviour as the temperatures T_I and T_M. Moreover, T_S remains constant at 1140 ± 10 °C for ceria concentrations of up to 20 % and then decreases to $1070° \pm 10$ °C for higher ceria contents (Table 11).

Table 11. Characteristics temperatures T_I, T_M, T_F, and T_S and specific heat Q determined from the DSC curves of the ThO$_2$ -CeO$_2$ system.

CeO$_2$, %	T_I, °C	T_M, °C	T_F, °C	Q, J/g	T_S, °C
0	473	584	685	-13.1	1136
5	475	589	671	-11.3	1146
10	463	579	678	-15.9	1137
15	450	569	680	-18.0	1142
20	465	565	679	-19.5	1141
25	432	560	676	-26.5	1076
50	388	495	672	-65.5	1071
75	348	447	678	-79.9	1072
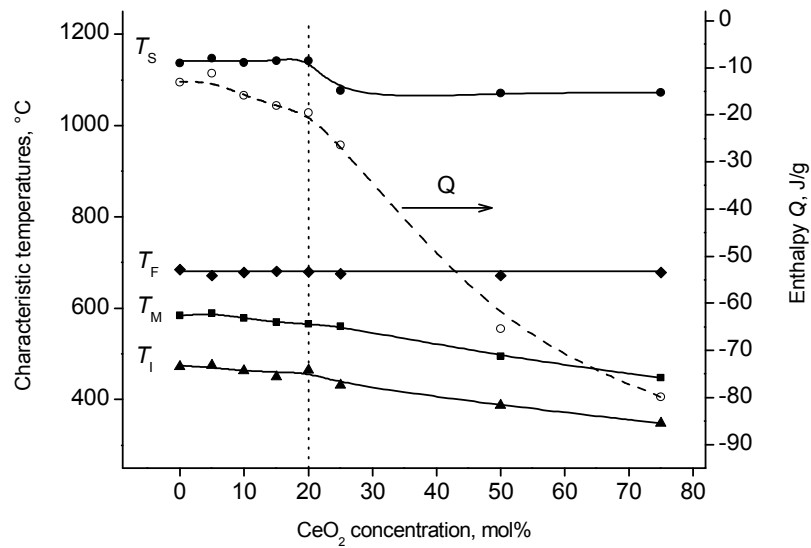
Figure 67. Influence of ceria concentration on the characteristic temperatures T_I, T_M, T_F and T_S and the enthalpy Q.

Thus, the thermal properties of the ThO_2-CeO_2 system can be divided into two regions as a function of ceria concentration: from 0 to 20 % and from 20 to 100 %. In the first region, the investigated properties (T_I, T_M, T_F, T_S, and Q) remain constant and are mainly determined by the properties of the thoria matrix. In the second region, the properties tend to the properties of ceria.

8.2.2. Crystallisation behaviour of the powders

According to the TG-DSC results, the powders containing 0, 10, 25, 50, 75 and 100% of ceria were calcined in the DSC furnace at 200, 300, T_I, T_M, T_F, 1100 and 1600°C, before XRD analysis.

Pure thoria crystallises after drying in a face-centred cubic (fcc) fluorite-type structure (Figure 68a) and its lattice parameter (a, Å) continuously decreases with increasing calcination temperature (Figure 69). A dependence between the lattice parameters and the mass loss, as defined in equation 4, was determined :

$$ML, \% = [TG(T_I)\text{-}TG(T)]/TG(T_I) \tag{23}$$
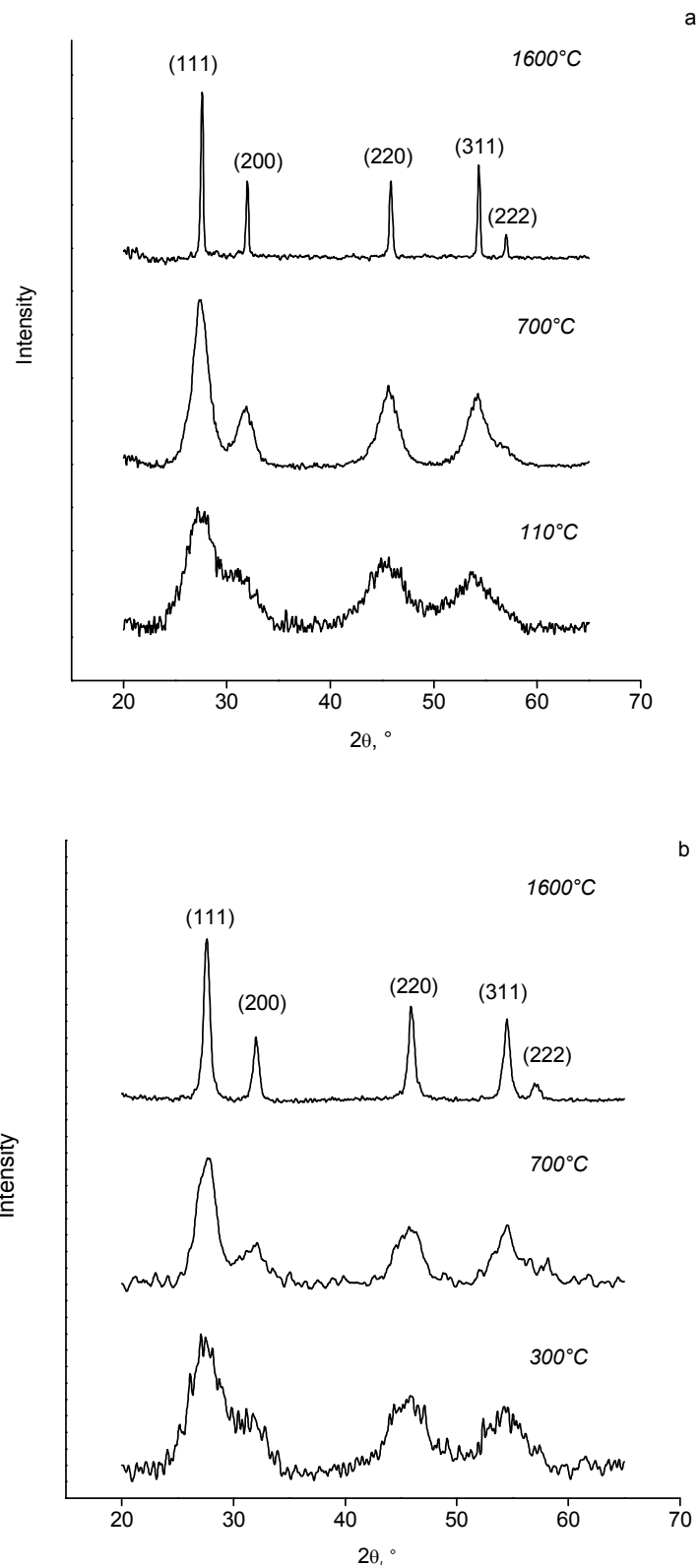
Figure 68. Powder X-Ray diffractograms for pure ThO$_2$ (a) and ThO$_2$ -10 CeO$_2$ (b) after calcination at different temperatures.
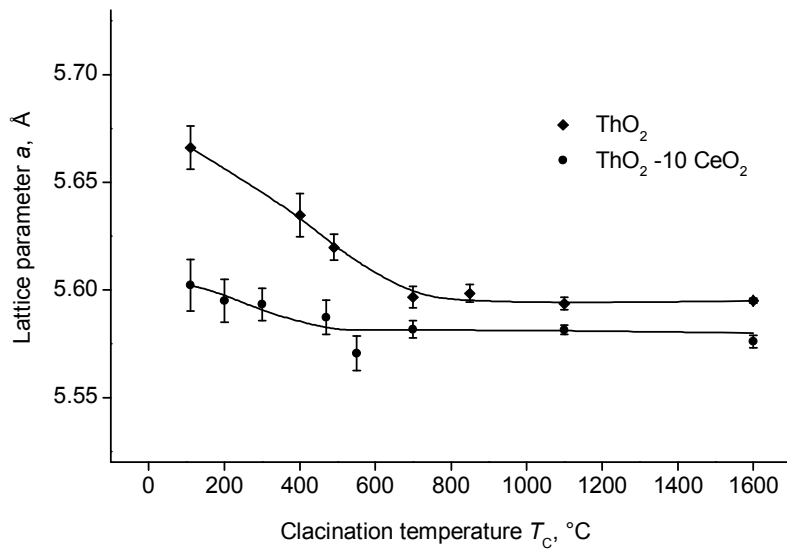
Figure 69. The lattice parameter as a function of the calcination temperature for ThO₂ and ThO₂ - 10 CeO₂ powders.

As shown in Figure 70, the lattice parameter has a linear dependence on the mass loss. The linear correlation confirms that the lattice parameter is determined by the presence of OH groups in the material [102].

Thus, the endothermic peaks observed on the DSC curves at $T_M = 584$ and 341 °C for thoria and ceria are representative of the elimination of the OH groups present in the lattice.
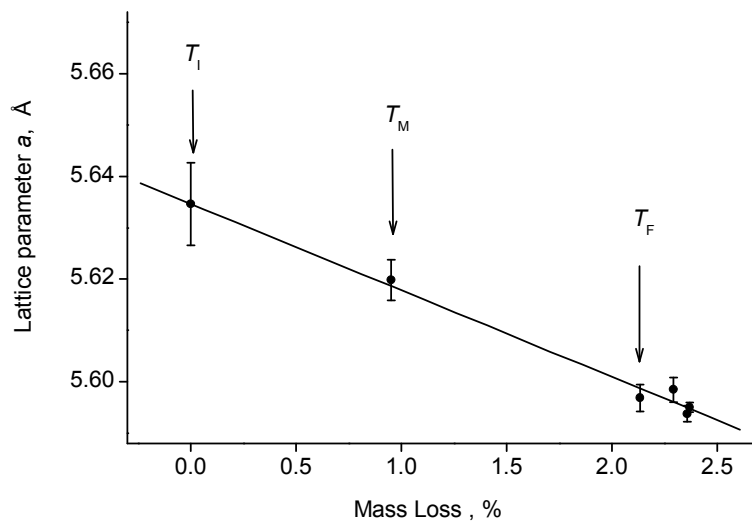
Figure 70. The lattice parameter as a function of mass loss for ThO₂.

The crystallisation of pure ThO_2 was studied in more details. The crystallite size (L) and the lattice distortions ($<\varepsilon^2>^{1/2}$) were determined as a function of the calcination temperature, as well as the relative crystallinity degree.

The crystallite size L has a value of 4 nm after drying (Figure 71). This value is representative of the primary particle size after precipitation. During drying process they aggregate and form agglomerates like presented in Figure 72. Between 490 and 700°C the particle size increases from 4 to 6 nm and remains constant up to 850 °C. Then L strongly increases up to 50 nm at 1600°C. The recrystallisation process starts at 850°C. In parallel, the lattice distortions (Figure 71) first continuously decrease from 1.7 to 1.2 % when the temperature increases up to 490 °C, then steeply decreases to 0.1 % until 850°C and reach a value of 0.01% at 1100°C. Similar results were found in the work of Moorehead et al. [121].
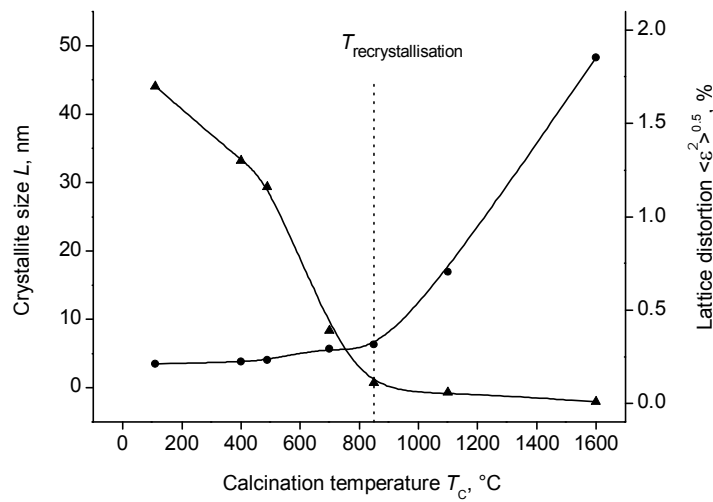
Figure 71. Evolution of the crystallite size _L_ and the lattice distortions $<\varepsilon^2>^{1/2}$ with the calcination temperature of ThO₂ powder.
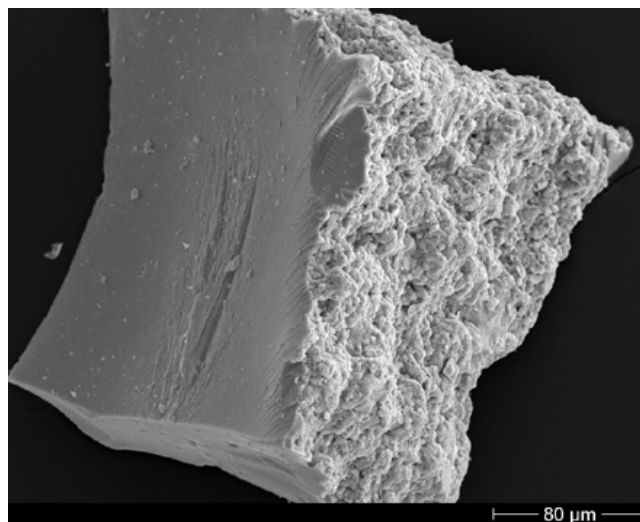
Figure 72. SEM photographs of ThO₂ - 10 CeO₂ powders after drying.

The behaviour of the crystallite size and the lattice distortions are correlated to the behaviour of the crystalline degree. After drying at 110°C, thoria has a crystallisation degree of 6% (Figure 73), which increases up to 8% when the temperature increases to 400°C. By increasing the temperature up to 700°C, it increases further to a value of 14% . The elimination of the OH-groups of the materials are so responsible for the increase of the crystallinity. The crystallinity degree then remains in the same order of magnitude until 850°C and then strongly increases. At 1600°C, thoria is completely crystalline.

The elimination of OH-groups characterised by an endothermic peak on DSC curves is mainly responsible of a decrease of the lattice distortions of the material.
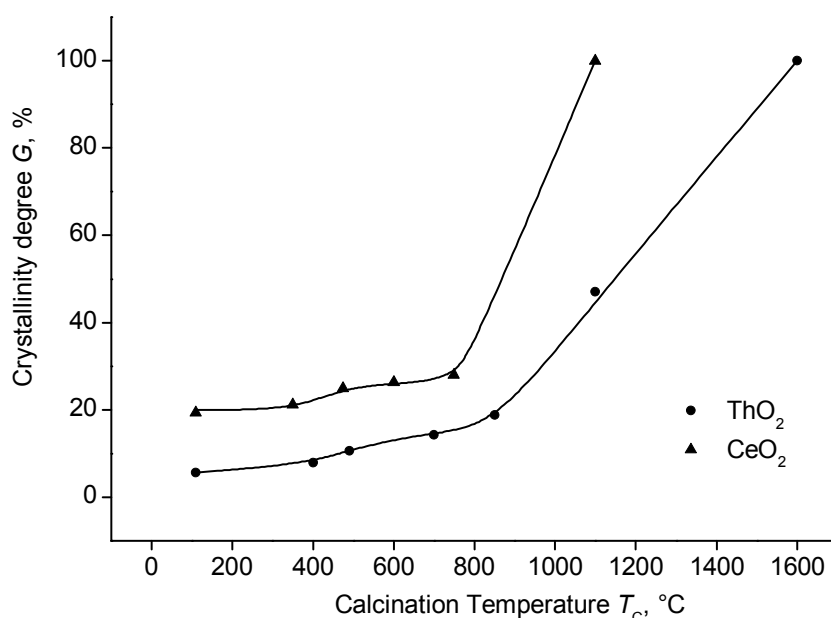
Figure 73. Dependence of the crystallinity degree of ThO$_2$ and CeO$_2$ powders with the calcination temperature.

The crystallisation of pure ceria has been already investigated above (Figure 32, Figure 33) Ceria also crystallise after drying in a fcc fluorite type structure. Its lattice parameter also continuously decreases with the calcination temperature and linearly with the mass loss. Heating between 350 and 475°C is responsible of an increase of crystallinity. The recrystallisation process takes place at 775°C and at 1100°C, ceria is fully crystalline. Moreover, for all calcination temperatures, the level of crystallinity is higher than in the case of ThO$_2$ (Figure 73).

According to XRD, the ThO$_2$-10 CeO$_2$ system crystallises after drying in a (Th,Ce)O$_2$ solid solution, fcc fluorite-type structure (Figure 68b). By increasing the temperature, the lattice

parameter of this system also decreases (Figure 69). However, contrary to pure ThO_2, no linear dependence between the lattice parameter and the mass loss in the temperature range from T_I to 1600°C can be established. The second endothermic peak observed on the DSC curves can be described not only by the elimination of OH groups of the $(Th,Ce)O_2$ system.

After drying and at calcination temperatures lower than T_F, the XRD peaks of the powders containing 25, 50 and 75 % ceria can be decomposed into 2 Gaussians revealing the presence of two separate phases of the same structure, fcc fluorite type, in the powder (Figure 74a). Thus, in the case of 25 %, after drying, the system is mainly composed of pure thoria and of a $(Th,Ce)O_2$ solid solution with a deficiency of thorium. ThO_2-50 CeO_2 and ThO_2-75 CeO_2 powders mainly consist of pure CeO_2 and of a $(Th,Ce)O_2$ solid solution with a deficiency of cerium. All these systems $(ThO_2, CeO_2, (Th,Ce)O_2)$ crystallise in a fcc, fluorite-type structure.

The lattice parameter was thus determined for each concentration as a function of the calcination temperature (Figure 75).

By increasing the calcination temperature up to T_I, the lattice parameter of the different systems decreases. At the calcination temperature T_F, the XRD lines are sufficiently sharp, so that they cannot be clearly described by 2 separated Gaussians. In this case, the average value of the XRD lines was used for the determination of lattice parameter a. And, at T_F, the value a tends to the value of the lattice parameter of a $(Th_{1-x}Ce_x)O_2$ solid solution. Further heating up to T_S (1100°C) results in complete solid solution formation (Figure 74b). The lattice parameter then remains fairly constant with temperature.

These results can be extended to powder with low ceria concentrations. In fact, ThO_2 has a low crystallinity degree after calcination at low temperature and the determination of this additional phase by the XRD method is therefore difficult. Moreover, in the case of 10 % ceria, the clear stoichiometry of the observed XRD phase could not be established. Considering these facts, powders containing up to 25 % ceria were certainly composed of $(Th,Ce)O_2$ solution and a segregation of ThO_2, that could only be clearly detected as a separate phase in the case of 25 % of ceria.

After calcination at 1600°C all powders crystallise in a face-centred cubic solid solution, fluorite type, and their lattice parameters follow the Vegard's law (Figure 76) :

$$a, Å = - 0.00185\ C_{Ce} + 5.59451 \tag{24}$$

These data correlate very well with the data obtained in the literature [122, 123, 124, 125]. The crystal structure of the ThO_2-PuO_2 system after calcination at high temperature was already studied [126, 127]. The system also crystallises in a fcc fluorite structure and follows the Vegard's law.

It is interesting to note, that after sintering the powders show different colours as a function of the ceria addition. Pure thoria is white. By adding ceria, the powder is becoming yellow and change to the pink when the ceria concentration reaches values of 50% and higher.
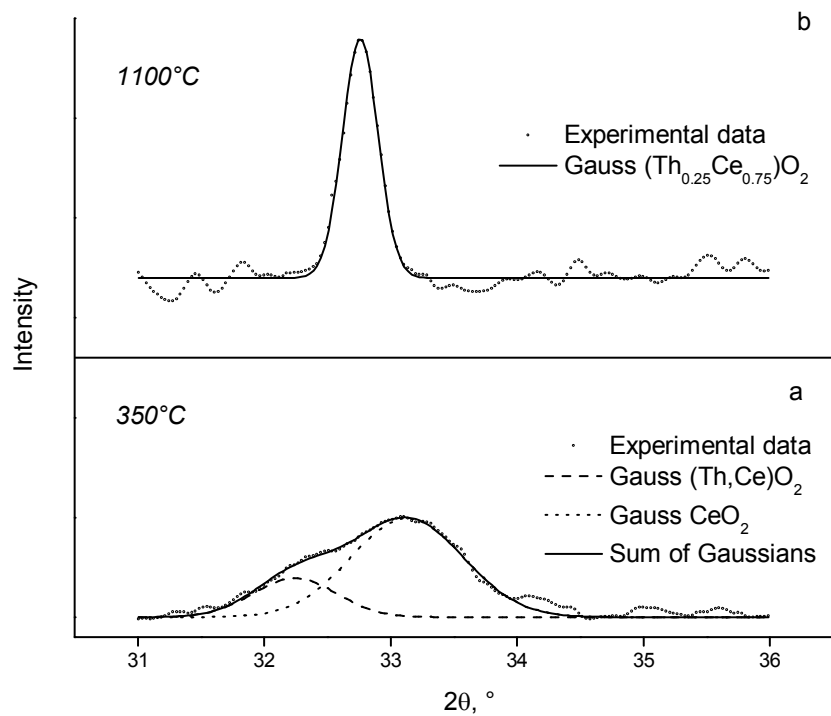
Figure 74. Fragment of XRD diffractograms of ThO_2 -75 CeO_2 powder after calcination at 350 and 1100°C.

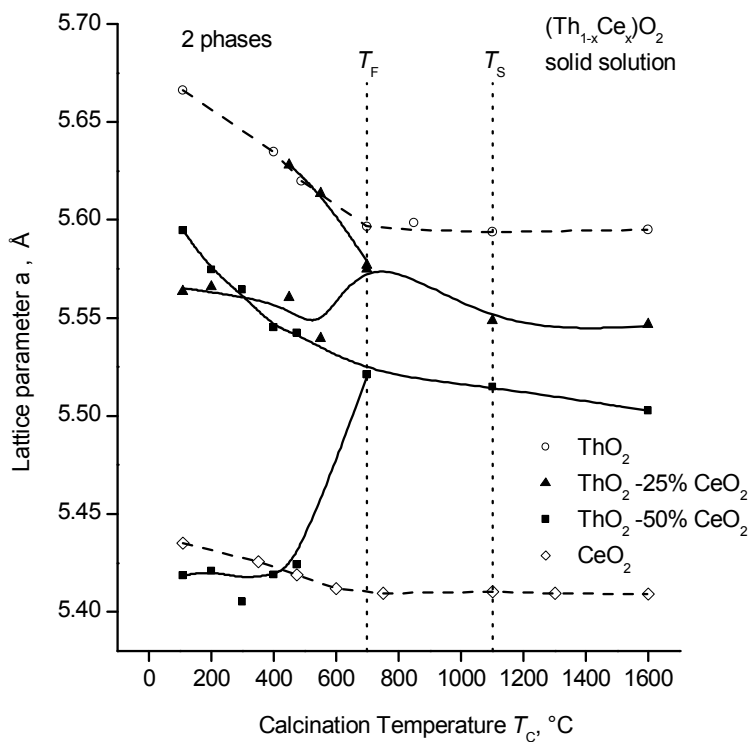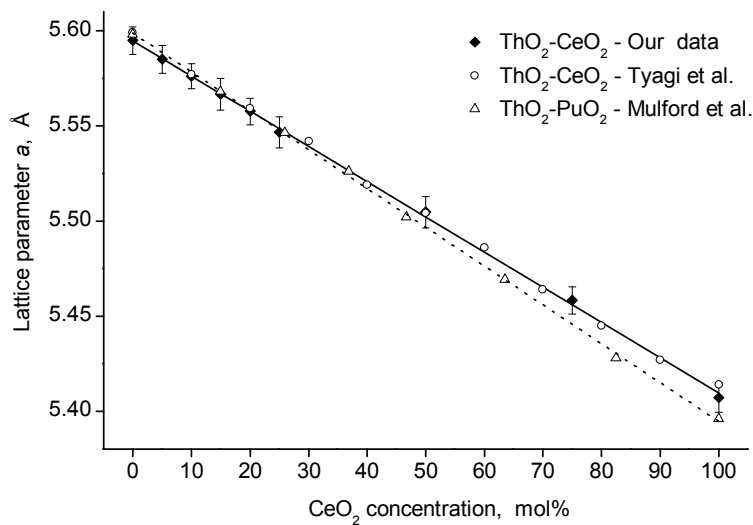**Figure 75. The lattice parameter of ThO_2, CeO_2, ThO_2 -25 CeO_2 and ThO_2 -50 CeO_2 as a function of the calcination temperature.**

Figure 76. The lattice parameter (a) as a function of ceria concentration after the calcination of powders at 1600°C.

It was demonstrated that after drying the powders mainly consists of two separates phases. The solid solution formation occurred mainly between T_F and T_S. The question of the signification of the second endothermic peak observed on the DSC curves remains. The data concerning the endothermic effect were so investigated into more details.

In fact, as described on Figure 77, the endothermic peak can be separated in two Gaussian, characterised by the temperature at the minimum T_{M1} and T_{M2} and by an enthalpy Q_1 and Q_2 respectively. Thus T_{M1} first remains constant at 530 °C up to ceria concentration of 20 % then decrease to 440°C, value at 75%, and tends to the value of pure ceria. T_{M2} also first remains constant at 580 °C, characteristic temperature of thoria, up to 20% of ceria and then slightly decreases up to 530 °C. Moreover, the ratio Q_1/Q corresponds to the proportion of ceria in the ThO_2-CeO_2 system (Table 12).
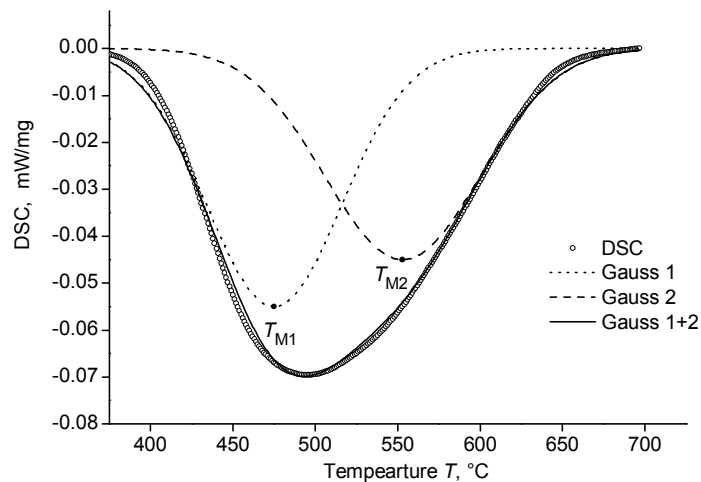
Figure 77. Description by 2 Gaussian of the DSC curve of the ThO_2-50 CeO_2 system in the temperature range from 400 to 700 °C.

126

Table 12. Dependence on the ceria content of the temperatures T_{M1} and T_{M2} and the relative specific heats Q_1/Q and Q_2/Q, characteristic respectively of the two Gaussian composing the endothermic effect observed between 300 and 700°C on the DSC curves of the ThO$_2$-CeO$_2$ system.

CeO$_2$, %	T_{M1}, °C	T_{M2}, °C	Q_1/Q,%	Q_2/Q,%
0	-	584	0	100
5	530	586	7.6	92.4
10	530	581	15.3	84.7
15	528	576	17.6	82.4
20	526	578	23.7	76.3
25	520	574	29.3	70.7
50	473	553	51.6	48.4
75	440	530	54.0	46.0

It has been demonstrated for pure ThO$_2$, that the endothermic peak corresponds to the elimination of OH-groups present in the lattice. Because of the strong decrease of the mass in this region, it can be supposed that the second endothermic effect observed on the DSC curves, also corresponds to the elimination of the OH-groups. However, this process would be decomposed in two steps. In the case of a ceria concentration from 0 to 25 %, the (Th,Ce)O$_2$ system would first released its OH-groups (first Gaussian), followed secondly by thoria (second Gaussian). In the case of higher ceria concentration, CeO$_2$ would first released its OH-groups followed by the (Th,Ce)O$_2$ system.

<u>Summary</u>

The thermal and crystallisation behaviour of the ThO$_2$-CeO$_2$ system was studied for different ceria concentrations. After drying, ThO$_2$ and CeO$_2$ crystallise as one phase oxides in a fcc fluorite-type structure. Both exhibit endothermic behaviour during heating due to the elimination of OH-groups from the lattice.

The ThO$_2$ -x CeO$_2$ mixture also presents an endothermic character, corresponding to an elimination of OH-groups. This elimination is supposed to happen in two steps. In fact, after drying the ThO$_2$-x CeO$_2$ system mainly consists of two fcc phases:

- a (Th,Ce)O$_2$ solid solution and pure ThO$_2$ for ceria contents less than 25 %

- a (Th,Ce)O$_2$ solid solution and pure CeO$_2$ for ceria contents higher than 50 %.

Heating these ThO$_2$ -x CeO$_2$ powders at temperatures between 700°C and 1140°C leads to the formation of a (Th$_{1-x}$Ce$_x$)O$_2$ solid solution, which also crystallises in a fcc fluorite-type structure. At calcination temperature higher than T_S, the system follows the Vegard's law.

According to the behaviour of the material with the addition of ceria, the range of ceria can be already divided in 2 clear regions. From 0 to 20%, the system principally follows the behaviour of ThO$_2$. For higher ceria concentration than 25%, the characteristics data of the system decrease with ceria addition and tend to the properties of ceria.

### 8.3. Physico-mechanical properties of (Th,Ce)O$_2$ ceramics

8.3.1. The compressibility and sinterability of the powders

(Th,Ce)O$_2$ pellets were fabricated with ceria concentrations from 0 to 25 %. After calcination at 400°C for 5 hours, the powders were pressed 2 times at 890 MPa in order to crash the agglomerates and to improve the packing. The third pressing was performed at different pressure between 640 and 890 MPa in order to determine the best compacting pressure. Pellets were then sintered at 1600°C for 5 hours, and their density determined by hydrostatic weighing in water. As seen in the Figure 78, where the relative sintered densities are plotted as a function of the last compacting pressure, the density increases with the pressure. 890 MPa was so selected as the best compacting pressure.
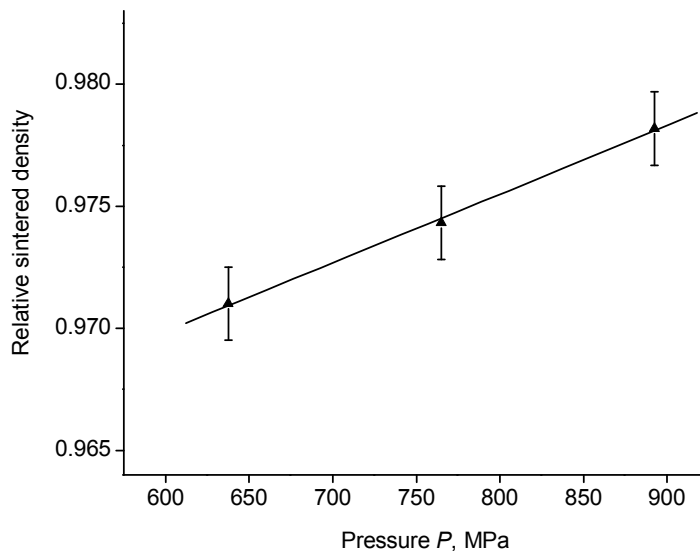
Figure 78. Dependence of sintered densities of pellets on the third compacting pressure for ThO$_2$- 10 CeO$_2$ system.

For the best pellets, the relative density of the pellets was determined as a function of ceria addition (Figure 79). The density of the pellets reaches a value of 0.94 TD for pure thoria and 5 % ceria and then steeply increases up to 0.98 TD for concentrations of 10 to 20 % ceria. In fact, as already demonstrated in [128], the addition of cerium enhances the sinterability of thorium. Similar results were obtained in the case of plutonium [83, 127]. Recently, within the framework of the European thorium cycle project, ThO$_2$ and (Th,Pu)O$_2$ pellets were prepared by the sol-gel route, in order to perform irradiation experiments in the high-flux reactor in Petten [26]. As in our study for CeO$_2$, the pellets containing 11 % plutonium have a higher density (96.5 % of TD) than pure ThO$_2$ (95.3 % of TD) pellets.

128
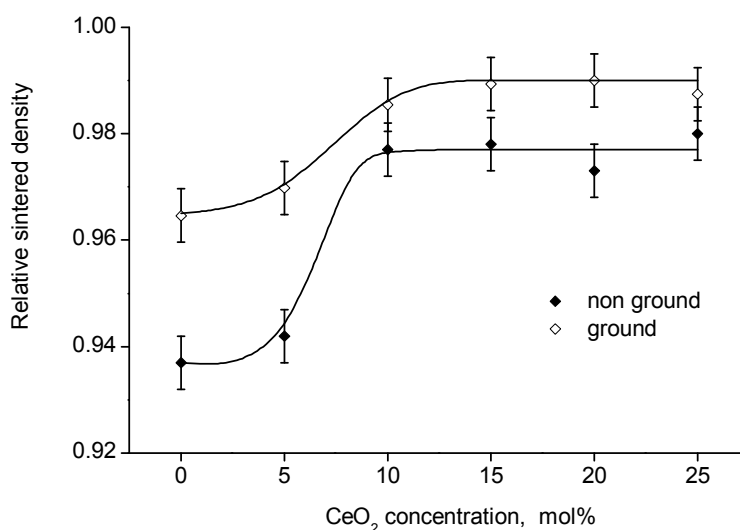
Figure 79. Dependence of relative sintered densities of pellets on ceria content.

After calcination at 400°C for 5 hours, a part of ThO_2-CeO_2 powders were softly ground by attrition in acetone and were pressed into pellets, using a repressing process applying two times a pressure of 890 MPa and one time a pressure of 640 MPa. The effect of ceria addition on the density of pellet is similar. Pellets of pure thoria have density of 0.96 TD which steeply increase up to 0.99 TD when the ceria concentration is 10%, and then remains constant (Figure 79), confirming the role of ceria on the sinterability of (Th,Ce)O_2 pellets.

As this work is devoted to nuclear applications, it has been noted that the process of pellets fabrication should be as simple as possible. The compaction of non-milled powder is representing an interesting way of synthesis, the pellets produced by this method will be so investigated physically and mechanically.

8.3.2. The microstructure of the pellets

After sintering, the pellets were polished, thermally etched at 1500°C for 30 min and their surfaces investigated by SEM. For all ceria contents, the pores are well distributed in the matrix (Figure 80a) and mainly located at the grain boundaries. The pores have an irregular shape and can be very large, reaching a size of up to 10 μm. This effect can be explained by the non-homogeneity of the initial packing. Moreover, the surface is composed of grains (Figure 80b) with well-formed grain boundaries. However, they have an irregular curvature.

In the representative case of 15 % ceria, the grain sizes have a lognormal distribution located between 0 and 8.0 μm (Figure 81) and an average grain size of 2.4 μm.

In the concentration range from 0 to 20 %, the addition of ceria does not change the average grain size of the pellet which remains at ~ 2.4 μm. However, when the concentration increase up to 25 %, the average grain size increases up to 3.4 μm, Figure 82. The border defined in previously at 20 % of ceria concerning the properties of ThO_2-CeO_2 system, clearly appears here.
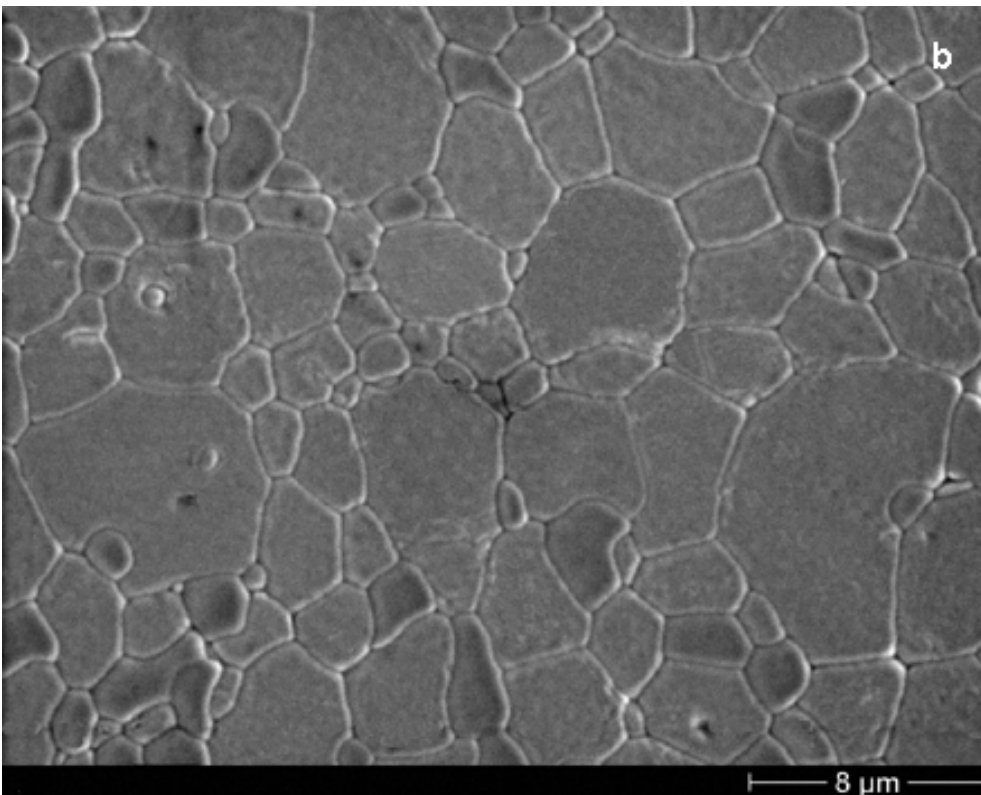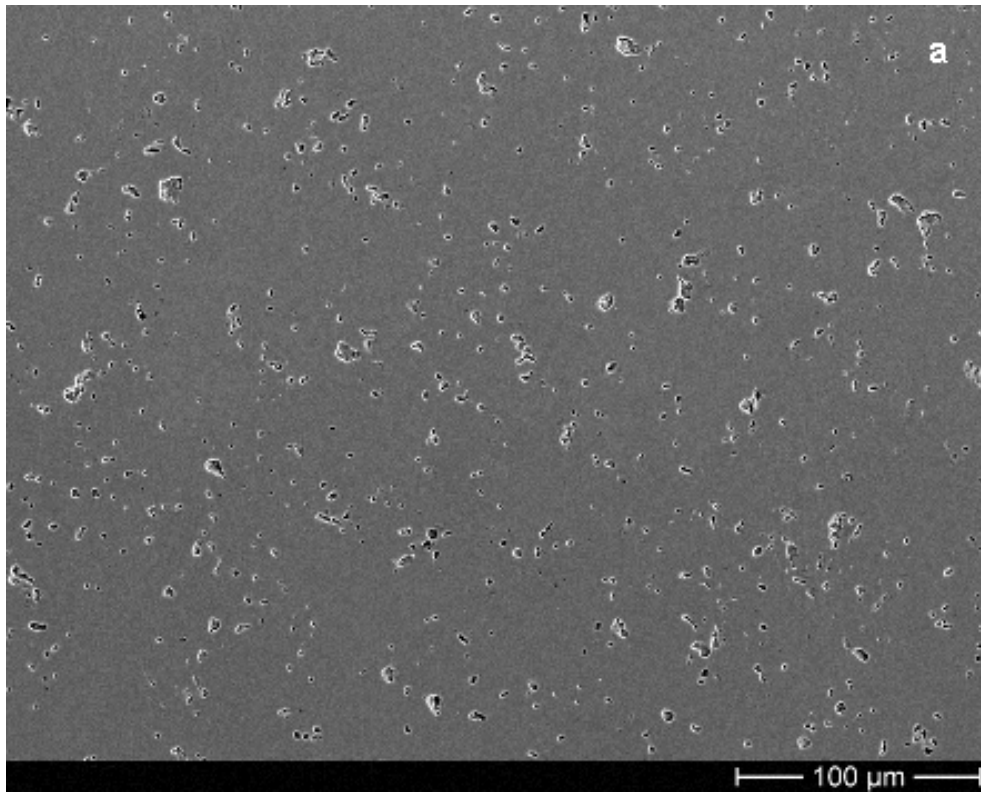
Figure 80. SEM photographs of $(Th_{0.90}Ce_{0.10})O_2$ pellets sintered at 1600°C for 5 hours.
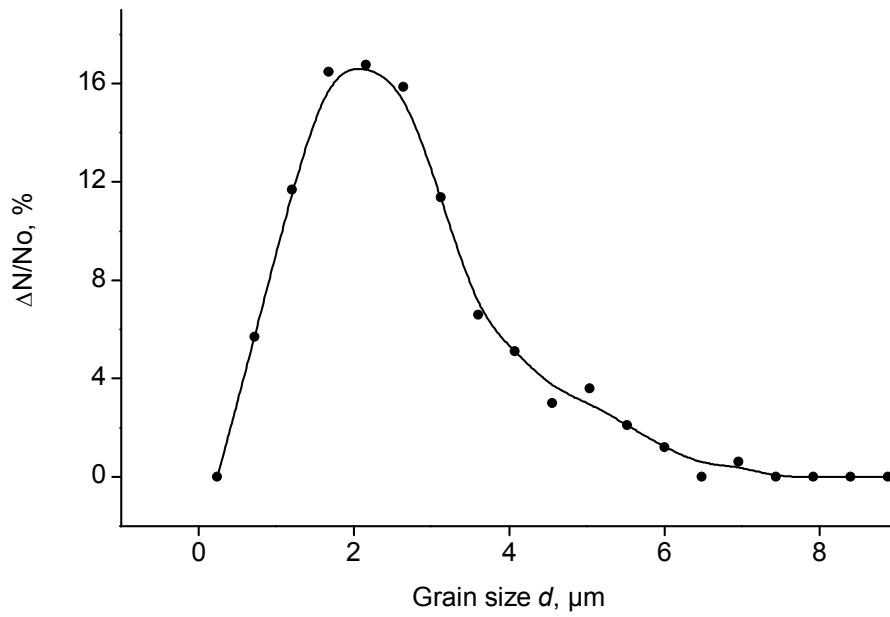
Figure 81. Grain size distribution of the ThO$_2$-15 CeO$_2$ pellet.
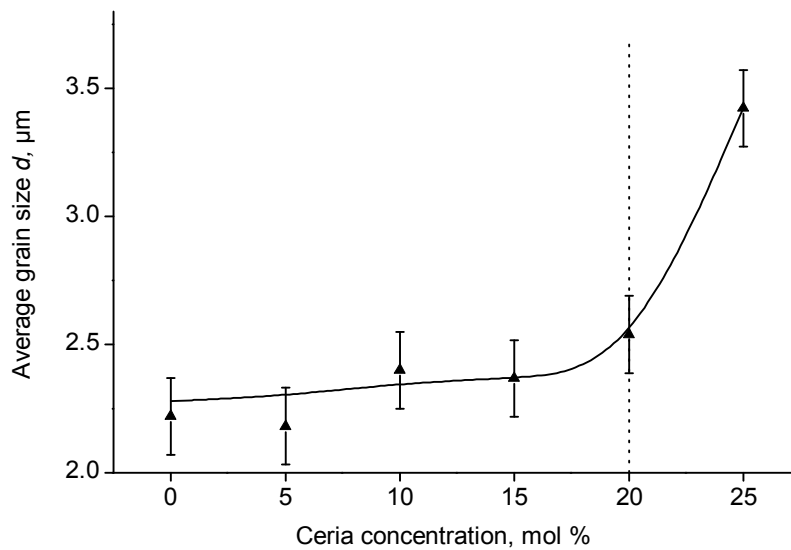
Figure 82. The average grain size of the pellet as a function of the ceria content.

8.3.3. The mechanical properties of the pellets

The dependence of the ceria content on the microhardness H_V and fracture toughness (K_{IC}) of the pellets was investigated applying a Vickers indenter with a load of 4 N. A typical photo of indenter and cracks is represented on Figure 83. The microhardness of the pellets increases with ceria addition from 8.6 to 10.3 GPa (Figure 84), correlating with the evolution of the pellet density (Figure 79). As described in [129], ThO_2 pellets with a density of 95 % have a Vickers hardness of 7 GPa. According to the work of S. Maschio et al. [116] , a ceramic of pure CeO_2 with a density of 0.94 TD has a microhardness of 3.9 GPa. Since both systems have a similar crystal structure, it is supposed that the addition of ceria to the ThO_2 matrix will decrease the mechanical properties of the matrix [116]. Moreover, Basak et al. [130] prepared $(Th_{0.96}Pu_{0.04})O_2$ pellets of 92 % density and measured a Vickers hardness of 3.4 GPa at 150 °C. An extrapolation of the data to room temperature gives a value of 4 GPa. Thus, the addition of Pu is also supposed to decrease the mechanical properties. However, in our case, the addition of ceria leads to an increase of sintered pellet density (Figure 79) and the mechanical properties of the material increase with increasing density [85]. Thus, for ceria contents from 5 to 25 wt%, the high increase in density of the pellets has a good effect on microhardness.

The fracture toughness of the pellets linearly decreases with ceria from 1.20 to 1.05 MPa·m$^{0.5}$ (Figure 84). The data obtained for pure thoria correlates well with the literature [131].
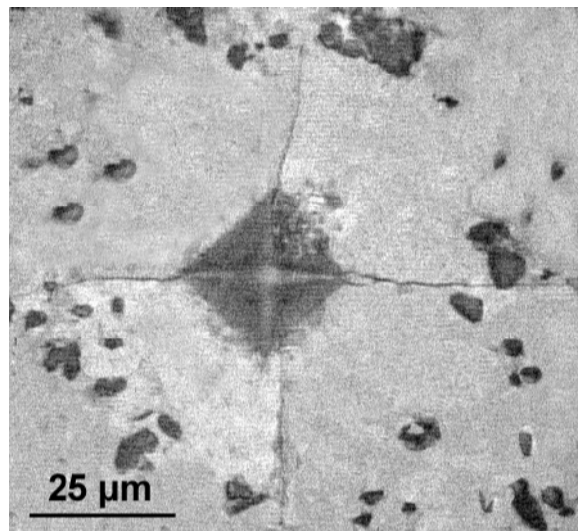
Figure 83. Optical microscope photography of an indenter on ThO$_2$-20 CeO$_2$ pellet.
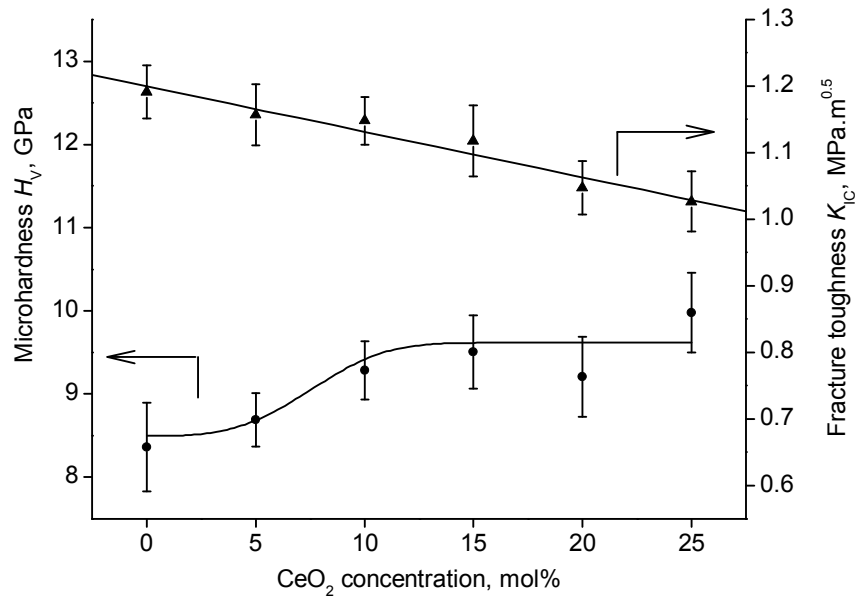
Figure 84. Dependence of the microhardness (H_V) and fracture toughness (K_{IC}) on the ceria concentration.

8.4. Conclusion

Physical properties of the $(Th,Ce)O_2$ powders synthesised by the co-precipitation method with different ceria contents (from 0 up to 100 wt.%) were investigated. After synthesis and drying, the ThO_2 -x CeO_2 powders are composed from 2 phases: a solid solution of $(Th,Ce)O_2$ and pure ThO_2 or pure CeO_2 function of the ceria content. Heating the powder between T_I and T_F , is responsible for an energy consumption associated with a strong decrease of mass, representative of an elimination of OH-groups. By heating up to 1100°C (T_S), the mass of the system is stabilised and both phases crystallise in one face centred cubic, fluorite type solid solution $(Th_{1-X}Ce_X)O_2$. After sintering at high temperature, the ThO_2 - CeO_2 system follows the Vegard's law.

According to the thermal properties of powders, the range of ceria in the ThO_2 - CeO_2 system can be divided in 2 regions. From 0 to 20%, the system principally follows the behaviour of ThO_2.

$(Th,Ce)O_2$ pellets were fabricated from non-ground powders by using a repressing process and reach densities up to 0.98 TD. For all ceria concentrations, the pellets show an homogenous surface, with well distributed pores. The mechanical properties of pellets were investigated and are very sensitive to the density evolution of system.

9. The oxidation state of Ce in the Ce-YSZ and ThO$_2$-CeO$_2$ systems

Cerium has the ability to change its oxidation degree with its environment. The oxidation degree of Ce influencing the properties of the systems, it is important to determine it in our case.

9.1. Oxidation state in aqeous solution, during hydrolysis washing and drying.

According to the electro potential E°(Ce^{4+}/Ce^{3+}) = 1.61 V, only Ce(III) can be stable in distilled water. However, Ce is the only lanthanide with a significant aqueous chemistry in +4 oxidation state. Aqueous "ceric" solutions can be prepared by the oxidation of Ce(III) solutions (cerous solutions) with strong oxidizing agent such as peroxodisulfate S$_2$O$_8^{2-}$ or bismuthate, BiO^{3-}. Complexation and hydrolysis combine to render E°(Ce^{4+}/Ce^{3+}) markedly dependent on anion and acidic concentration. Thus, concerning the hydrolysis, if the pH is increased, hydrolysis of Ce^{3+} to Ce(OH)$_3^+$ occurs followed by polymerisation and finally, as the solution becomes alkaline, by precipitation of yellow gelatinous CeO$_2$.nH$_2$O [132]. This gel is stable under further treatment like hydrothermal treatment for example [70].

Moreover, during washing of the gel after synthesis, if the Ce(III) was not completely oxidized, the oxidation is completed by a reaction with the O$_2$ from the air [89] following the reaction :

4 Ce(OH)$_3$ + O$_2$ + 2H$_2$O -> 4 Ce(OH)$_4$
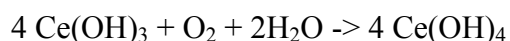
The gradual change in colour solution during further stirring after synthesis from white into brown, yellow and bright yellow is indicating the further oxidation of Ce(III) hydroxide to Ce(IV) [70].

Moreover, according to the solubility product Ks of Ce(OH)$_3$ and Ce(OH)$_4$, respectively 1.5x10^{-20} and 4.0x10^{-51}, it is obvious that the final reaction product should be Ce(IV) hydroxide since the free energy value of Ce(OH)$_4$ is more than Ce(OH)$_3$ [90].

In our case, after a long hydrolysis of Ce^{3+}, ZrO^{2+} , Th^{4+} and Y^{3+}, the obtained yellow Ce-YSZ and ThO$_2$-CeO$_2$ powders are washed in water for 24 hours. According to the DSC spectra powders consists of a majority of Ce(IV). Only for high concentration of ceria, residual Ce(III) was found in the initial powder. However, it oxidizes in Ce(IV) during heating at 350 °C in air atmosphere.

9.2. Oxidation state at high temperature and in final material

At high temperature, the actinides elements, like Plutonium or americium, as well as cerium may change their oxidation state. Moreover, these elements are very sensitive to the atmosphere in which they are sintered. However, if these elements are immobilized in YSZ matrix, the oxidation change can have a big impact on the stability of the material and its crystallography. It is so important to know the oxidation degree of cerium in our materials [97].

9.2.1. TG investigations

10-Ce-YSZ powder were first heated in air until 1300°C then cooled down up to 1000°C, heated again up to 1300°C and cooled down. The mass of the sample remains constant with the variation of temperature. No clear variation of the oxidation state of the cerium in the powder can be detected.

9.2.2. Thermodynamic calculation

CeO_2 is very sensitive to the atmosphere in which it is sintered.

The thermodynamics of oxygen partial pressure are considered. In Figure 85, the oxygen partial pressures of equilibrium between CeO_2 and Ce_2O_3 and between Ce_2O_3 and Ce are plotted as a function of the inverse of temperature. The oxygen partial pressures were calculated based on the free energy of oxide formation ($\Delta G = \Delta H - T \Delta S$) and computed using the program HSC.
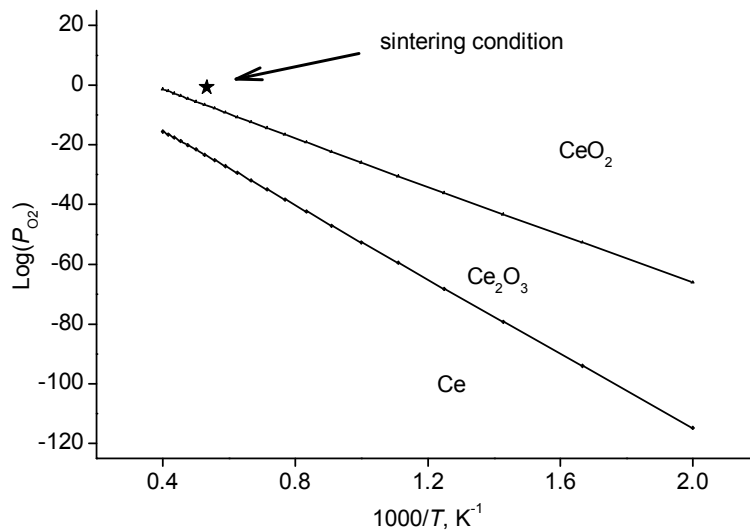
Figure 85. Oxygen partial pressures of equilibrium as a function of the inverse of temperature ; equilibrium between CeO$_2$ and Ce$_2$O$_3$, Ce$_2$O$_3$ and Ce. The star indicates the sintering condition.

The calculations were done as following, supposing that O_2 is a perfect gas and based on the following equations:

$$2 Ce + 1.5 O_2 \rightarrow Ce_2O_3$$

with reaction constant $K = 1/(P_{O2})^{3/2}$ (25)

$$\Delta G_{reaction} = \Delta G_{fCe2O3} - \Delta G_{fCe} \tag{26}$$

$$\Delta G_{reaction} = -RT \, Ln10 \, Log(K) \tag{27}$$

Thus, by combination of those equations :

$$2 \Delta G_{reaction} / 3RT \, Ln10 = Log(P_{O2}) \tag{28}$$

$$Ce_2O_3 + 0.5 O_2 \rightarrow 2 CeO_2$$
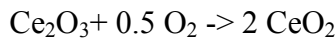
with reaction constant $K = 1/(P_{O2})^{1/2}$ (29)

$$\Delta G_{reaction} = 2\Delta G_{fCeO2} - \Delta G_{fCe2O3e} \text{ and} \tag{30}$$

$$\Delta G_{reaction} = -RT \, Ln10 \, Log(K) \tag{31}$$

Thus, by combination of those equations :

$$2 \Delta G_{reaction} / RT \, Ln10 = Log(P_{O2}) \tag{32}$$

Considering the fact, that the sintering is made at 1600°C in air atmosphere and that the air is composed from 20% of O_2, it can be seen that under this sintering conditions, CeO_2 is stable.

9.2.3. Crystallography

YSZ system crystallises in a stable fluorite type structure, where metal atoms have a coordination number (CN) of 8 and oxygen atoms have a CN of 4. However, the presence of the aliovalent dopant Y in the system will introduce oxygen vacancies V_{02-} which will be located around Zr, due to the smaller size of Zr atom, Table 13 [133]. In this case a proportion of Zr will have a CN of 7.

Table 13. Ionic radii of the elements applied for this study.

Coordination Number	Ionic radii (nm) [134]						
	Ce^{4+}	Ce^{3+}	Y^{3+}	Zr^{4+}	Th^{4+}	Pu^{4+-}	O^{2-}
4	-	-	-	-	-	-	0.138
7	-	-	-	0.078	-	-	-
8	0.097	0.114	0.102	0.084	0.105	0.096	-

Ce is now introduced in the system, forming a stable solid solution. Two cases should be envisaged :

1) If Ce has an oxidation state of IV, then, no extra V_{O2-} will be introduced in the system. Because of the big size of the Ce radii (Table 13), the oxygen vacancies are supposed to be located around Zr.

2) If Ce has an oxidation state of III, then Ce will introduce extra V_{O2-} in the system which will be located around Zr. If the Ce(III) concentration reaches a critique concentration $[Ce]_{Cr}$, then all Zr atoms will be surrounded by an oxygen vacancy and the structure may have some instability. If the concentration of Ce still increases, a second V_{O2-} will surround Zr atoms which will have a CN of 6. If all Zr are surrounded by two V_{O2-} then the structure change from defected fluorite to a pyrochlore [135].

The critical concentration $[Ce]_{Cr}$ was calculated as :

$$[V_{O2-}] = [Ce] + [Y] = [Zr] \text{ with } [Y]/([Zr]+[Y]) = 0.16 \tag{33}$$

So the critical concentration was estimated at 40.47 atom% of Ce.

9.2.4. Ingel &Lewis modelling

According to the Ingel & Lewis model [136], in the case of a fluorite structure, the lattice parameter a can be defined as following:

$$a = 4 \, (r\text{-} + r^+)/\sqrt{3} \tag{34}$$

where r- and r^+ are the ionic radius of the anionic and cationic species respectively. The ionic radius r^+ should be considered as an average of all ionic radii, expressed as :

$$r^+ = \sum_i C_i R_i \tag{35}$$

where C_i is the concentration and R_i the ionic radius of the species I at fixed CN.

The lattice parameter of our Ce-YSZ system were so theorically determined as a function of the Ce concentration in the case of Ce^{3+} and Ce^{4+}. The data were compared with the experimental data obtained for powder after calcination at 1600°C (Figure 86a).

Although the experimental data are slightly lower than the calculated one, they correlate well with the theoretical curve obtained for Ce^{4+}. Moreover, for all ceria content, Ce-YSZ follows the Vegard's law and the lattice parameter determined for CeO_2 experimentally $(5.414 \pm 0.0070 \text{ Å})$ correlates with the theoretical one 5.416 Å and the JCPDS data $(5.4112 \pm 0.0012 \text{ Å})$. So according to this fact, it can be conclude that Ce(IV) is predominant in our powders.

Kinoshita et al. [97] have sintered Ce-YSZ pellets in oxidizing and reducing atmospheres and determined the structure its lattice parameter as a function of the ceria content. A clear difference in the slope have been obtained between samples sintered in oxidizing and

reducing conditions. The lattice parameter in the second case is higher than in the first case, following the Ingel & Lewis model and demonstrating that Ce is found under oxidation state IV if Ce-YSZ was sintered in oxidizing atmosphere, while Ce is Ce(III) in reducing atmospheres. Moreover, it was demonstrated that for concentration of cerium higher than 15 mol%, Ce-YSZ crystallises in a pyrochlore structure, when it was sintered in reducing atmosphere.

Yamashita et al [100] have done the same work on the Pu-YSZ. Similar results were obtained except that the pyrochlore structure was found only for Pu concentration of 39%.
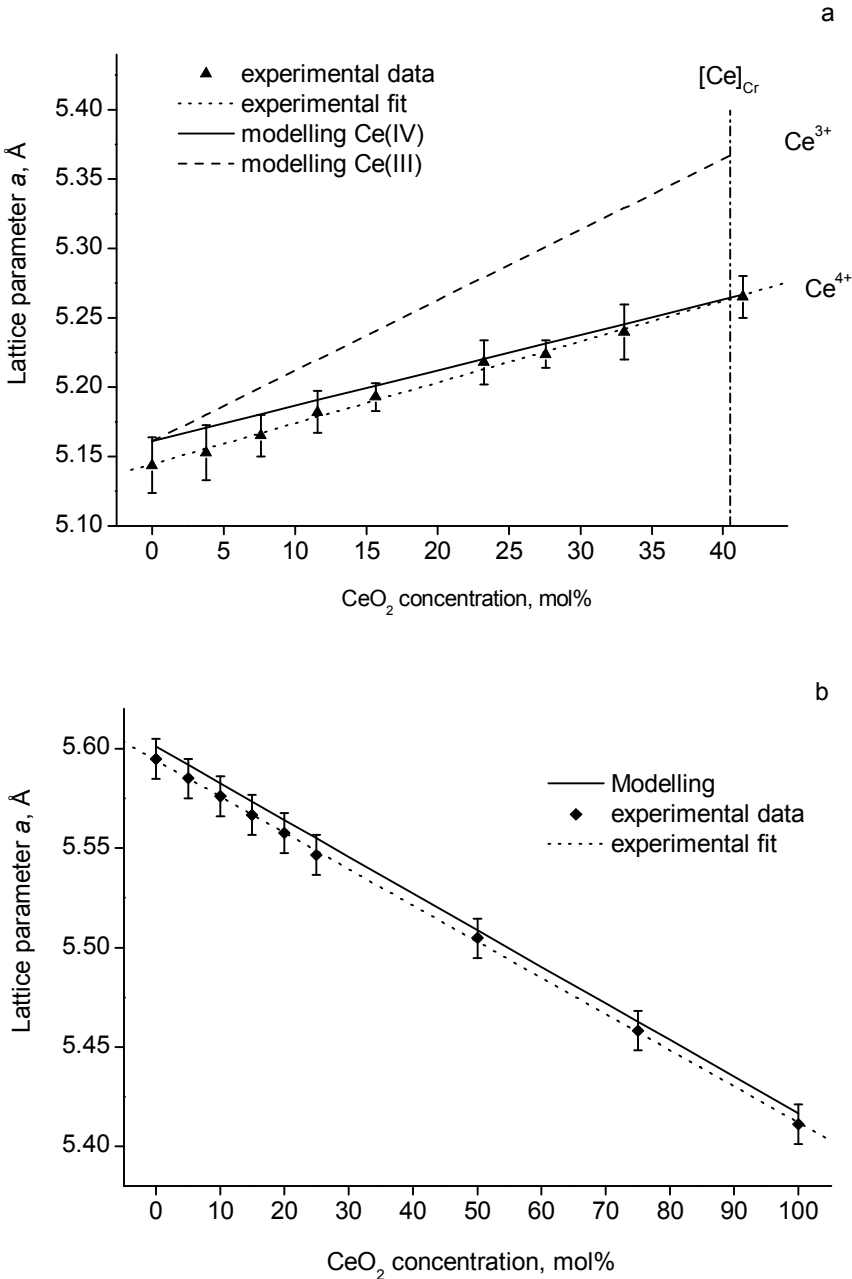
Figure 86. Experimental and theoretical lattice paratemer of the Ce-YSZ fluorite system (a) and the ThO$_2$-xCeO$_2$ system (b) as a function of Ce content and the oxidation degree of Ce. The theoretical curves were calculated based on the Ingel and Lewis model.

The Ingel and Lewis modelling was applied on the (Th,Ce)O_2 system, taking into account that Ce is under the oxidation state +4. As seen on the Figure 86 b, the theoretical values of the lattice parameter correlate at 0.1 % with the experimental data and the values of pure CeO_2, for the complete range of ceria concentration. It can be concluded that Ce(IV) is present in the powder.

The Ingel and Lewis model was extended to the (Th,Pu)O_2 system. The obtained datas correlates at 0.03 % to the data presented in the work of Mulford et al. [126]. The Ingel and Lewis model can so be employed to describe the system.

9.2.5. XPS investigations on 10- and 50-Ce-YSZ pellets.

The nucleus of 10 and 50-Ce-YSZ pellets have been investigated by X-Ray photoelectron spectroscopy.

The investigations reveal that in the case of 50-Ce-YSZ, only Ce(IV) was found in the pellet, confirming the results presented above. Moreover, it should be noted that for this Ce concentration (50 wt.% = 41.4 mol%), Ce(III) is not stable in the fluorite structure.

On contrary, in the case of 10-Ce-YSZ, Ce(III) as well as Ce(IV) were found in the pellet. In fact, at this concentration, Ce(III) and Ce(IV) are stable in a fluorite structure. So in principle, both species can exist. Moreover, the presence of Yttrium in the system involves the introduction of V_{O2-} in the system. For electro-neutrality reasons the V_{O2-} should be connected to a trivalent cation. It is so supposed that, if Ce is the nearest cation, then Ce, being stable under both oxidations degrees can be connected with this oxygen vacancies, being so reduced to the valance III.

10. General conclusion

10.1. Summary

Plutonium and the so-called minor actinides (Am, Cm, Np) are responsible for long-term radiotoxicity. In order to improve long-term safety, specific treatments of these actinides are envisaged. Selective partitioning followed by transmutation (P&T partitioning and transmutation strategy) has been foreseen for the reduction of long-term radiotoxicity. Alternatively, the conditioning of these long-lived actinides (P&C partitioning and conditioning strategy) is also taken into consideration. However, both strategies require the development of advanced ceramics which can immobilise Pu and MA in a matrix. Two inert (quasi-inert) oxide matrices, yttrium fully stabilised zirconia and thoria, have been foreseen as promising candidates.

The first objective of the work was to determine the concentration of tetravalent Pu or MA-oxides, substituted by CeO_2, that can be immobilised in these ceramics without degradation of their chemical and physical properties. Within this framework, $(Zr,Y)O_{2-x}$-CeO_2 and ThO_2-CeO_2 powders with variable ceria contents were synthesised, employing a co-precipitation method of nitrate and chloride solutions by NH_3. The impact of cerium addition on the properties of the matrices was evaluated. The systems were first characterised by studying the thermal and crystallisation behaviour of the powders as a function of ceria concentration. Both systems crystallise at high temperature ($T \geq 1300°C$) in a stable solid solution, fcc, fluorite-type structure without apparent segregation of ceria. Their lattice parameters were determined and follow the Vegard's law. For both systems, a critical concentration C_{Cr}, of 20 mol % ceria has been defined. At concentrations lower than 20 mol. %, the properties of the material are determined by the matrix.

The second objective of the work was to study the possibility to fabricate zirconia- and thoria-based ceramic pellets, with stable and reliable properties by using simple fabrication processes adapted to radioactive materials. Thus, $(Zr,Y,Ce)O_{2-x}$ and $(Th,Ce)O_2$ pellets with different ceria contents were fabricated. The technological routes were completely built up. For each fabrication step, the optimum technological parameters (T_C, P_{opt}, grinding and fractionation conditions etc…) were determined based on the investigation of the powder and pellet properties. Thus, the physical properties, such as compressibility, sinterability, densification behaviour, have been investigated as a function of calcination temperature and ceria concentration.

For both systems, pellets with densities of up to 97 - 98 % of TD, with a good microstructure, homogeneous pore distribution and good mechanical properties could be obtained by using simple fabrication processes, described as follows.

(Zr,Y,Ce)O$_{2-x}$ ceramic synthesis	**(Th,Ce)O$_2$ ceramic synthesis**
Synthesis by co-precipitation by NH$_3$	Synthesis by co-precipitation by NH$_3$
Washing in water	Washing in water
Drying in air at 110°C	Drying in air at 110°C
Calcination in air at 600°C for 2 hours	Calcination in air at 400°C for 5 hours
Grinding by attrition in acetone	Triple Pressing by repressing at 900 MPa
Fractionation in acetone	Sintering in air at 1600°C for 5 hours
Uniaxial cold pressing (P = 900 MPa)	
Sintering in air at 1600°C for 5 hours	
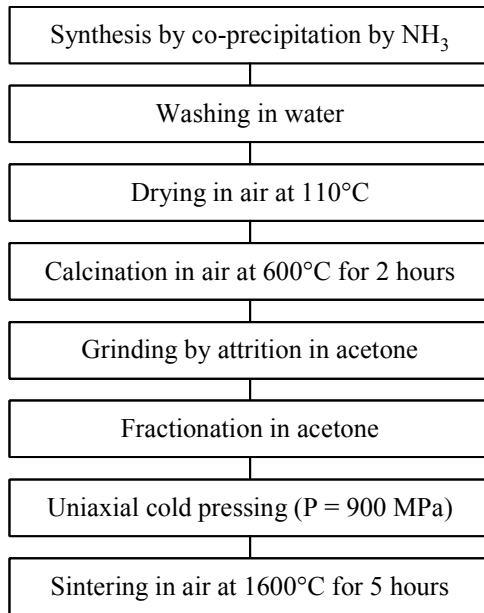
For both systems, the ceria-critical concentration of 20 mol% remains for the pellets. Moreover, the addition of ceria has a positive impact on the sinterability of material, particularly if this concentration is higher than 5 %.

10.2. Outlook

In order to give a reliability for the established pellet synthesis routes, the processes were compared with the industrial process for UO$_2$-PuO$_2$ Mixed oxide (MOX) fuel preparation.

As described in the first part of the work, the MOX technology employed the classical powder blending dried route, unfortunately accompagnied by dust formation. On contrary, in the present work, zirconia based ceramics are prepared by mild and wet methods. Thorium based ceramics, were even prepared without grinding nor milling , the pressing by repressing replacing the milling step. The application of these technological routes to Pu management seems to be technologically applicable [41].

However, some questions still remains :

- Is it possible to employ these processes in a case of americium/curium management ?
- Is there a possible application of the fractionation step to an industrial scale ?
- Is it possible to apply the pressing by repressing to an industrial scale ?
- Is the fuel perfectly homogeneous at the nanoscopic scale ?
- Is it possible to eliminate the dust formation for the complete ceramic production cycle ?
- Is the co-precipitation method interesting for further application ?

10.2.1. The americium/curium- management

Americium and Curium are responsible of a stronger heat and neutron release than in the case of Pu [137], requiring only remote handling fabrication procedure.

In this case, for the zirconia process, the choice of acetone as solvent to perform a grinding and fractionation, may be a problem because of its low boiling point and its inflammable properties. The choice of another solvent with higher boiling point, an adapted viscosity and polarity and resistant to the radiolysis is suitable. Theoretical studies have been orientated to cyclohexanone, free of OH-groups, with a boiling point of 155.6 °C [138] and a viscosity of 1.321 mPa.s at 50°C[139]. However, it is known that the viscosity decreases with the temperature, and, the control of the viscosity is necessary for a selective fractionation. So thermostated installations are necessary, whatever the solvent is.

In the case of the thoria process, the pressing by repressing may be responsible for extra-dust formation. It is so foreseen to apply this process only to plutonium.

10.2.2. Technical application of the fractionation step

10.2.2.1. Schematic design of an eventual application and technology

The fractionation step was performed in the case of Zirconia-based ceramics synthesis in order to obtain homogeneous powders before compaction and sintering. The same solvent was used for grinding and fractionation. After fractionation, coarse agglomerates remaining in the non fractionated powder (rest), can be fragmentized by further grinding. Thus grinding and fractionation steps may be considered as a closed system. Technological application may be envisaged in this point of view. Two schemes have been drawn on Figure 87 and Figure 88, as a possible applications.

In a first system (Figure 87), after drying at 110°C, the powder is transferred in the grinding installation with acetone. After grinding, the mixture containing acetone and the ground powder is transferred in the fractionation installation. The mixture is ultrasonically or mechanically shacked and after decantation, the fractionated part is collected in a flask. A laser granulometry control can be performed before collecting the fractionated agglomerates. The collector is heated at 80 °C allowing the evaporation of acetone which is condensed and recycled. The coarse agglomerates which were not collected after fractionation should be transferred back to the grinding installation. After having being dried at 80 °C the small agglomerates free of acetone are collected and dried in an oven at 110°C before pelletization.

Another more compact system can be used (Figure 88): grinding and fractionation can be performed alternatively in the same installation. After grinding, the mixture is leaved for decantation and after a granulometry control the fractionated part is collected. Acetone can be recycled. Grinding and fractionation are made alternatively.
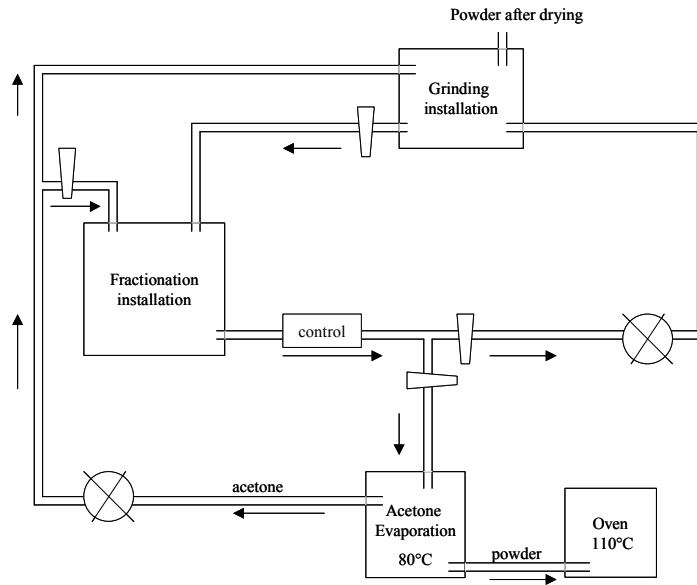
Figure 87. Schematic design of a grinding and fractionation installation.
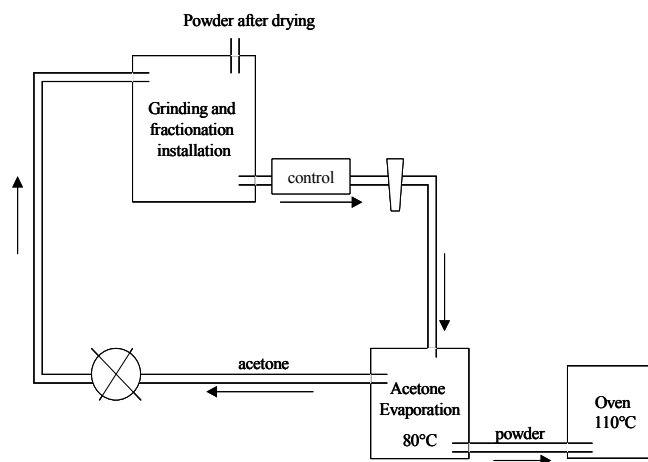
Figure 88. Schematic design of a grinding and fractionation installation.

The technique is already developed in industry to perform the separation of material as a function of its size. It is named Field Flow Fractionation technique or FFF technique [140].

Field-flow fractionation (FFF) is the most versatile separation technique of all macro molecular and particle separation methodologies in terms of separation range, selectivity and resolution. The separation occurs by differential retention in a stream of liquid flowing through a thin, empty channel. The separated components are eluted one at a time into the detector.

FFF is an elution technique and requires a field or gradient. Different kind of fields have been applied to FFF : sedimentation, thermal, electrical or gravitational. In gravitational FFF the field is just the earth's gravity, and the technology is able to fractionate particles in the supermicron range depending on their size. The most employed in ceramic industry is the sedimentation FFF [141]. In this case the channel is spooled inside a centrifuge bowl. The

144

spinning of the channel generates differential acceleration forces at right angles to flow. The retention time depends on particles' dimension and density [142]. Sample size typically spans the colloidal range, from 30 nm to 1 μm and more. A representation of a FFF installation is represented on Figure 89.
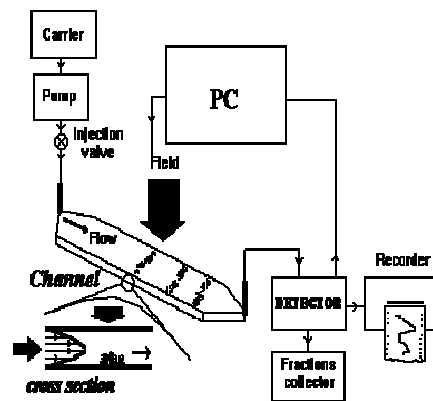
Figure 89. Schematic design of a FFF installation [140].

10.2.2.2. Scientific reliability of an industrial application of the fractionation process

The fractionation step was added in the pellet synthesis route in order to use powders free of coarse agglomerates. However, the sinterability of materials is not dependant only on the agglomerates size but mainly on agglomerates nature (hard/soft). Hard agglomerates are responsible of coarsening, limiting the sinterability of the powder and responsible of defects in the microstructure. In order to get homogeneous material, it is better to use only soft agglomerates [53, 54, 105, 143].

However, the fractionation step, technologically applicable at temperatures lower than 600°C, allow a separation between soft and hard agglomerates only in the specific case of powders calcined at 600°C. The coarse agglomerates (mainly hard) remaining after fractionation are needed to be treated. Considering the system {grinding, fractionation} as a closed system, these hard agglomerates can be broken in fine powder by grinding and extracted by fractionation. However, the fractionated powder will be enriched in hard agglomerates, that are responsible of coarsening and so limit the sinterability of pellets and so their properties [104, 145].

In the presented work, pellets were prepared from powders containing a majority of soft agglomerates. These pellets have a homogeneous microstructure, well-formed grains and sub-micron pores, densities of 96-97 % of TD and a microhardness of 16.5 GPa. In a previous work [119], pellets have been prepared by ground powders only, containing hard and soft, little and coarse agglomerates. These pellets had a density of 92-93 % of TD and a microhardness of 11-13 GPa. Nevertheless, the pellets had a homogeneous microstructure. The grains are well formed surrounded by large elongated pores and intern porosity.

145

If now pellets are prepared from fine powders enriched by little hard agglomerates, their properties are supposed to be located between the properties of pellets prepared from ground powders and pellets prepared from fractionated powders [112]. The limits of the co-precipitation method have been defined.

10.2.2.3. Alternative to the fractionation process

To avoid the problem of coarsening, it would be interesting to have powders consisting of a majority of soft agglomerates.

In fact, after synthesis, the powder consists of hydroxide particles, which will agglomerates during drying and form hard and soft agglomerates. The origin of the hard agglomerates comes from the formation of oxo-bridges between particles during drying by interaction of the OH-groups. To avoid the formation of the oxo-bridges, the OH-groups of the hydrolysed species can be replaced by R-O groups, or water can be eliminated from the system before drying. This may be possible by treating the powder in alcohol or a mixture actone/toluene/acetone [112, 147 - 152].

A first test has been performed on 10-Ce-YSZ powder. The powder was washed 5 times by acetone, then calcined at 350°C, pressed and sintered at 1600°C for 5 hours. A density of 0.94 TD was obtained. These results are promising. However, the problem of compatibility of the solvent with radioactive material (radiolysis, heat decay, inflammable properties etc…) remains.

10.2.3. Pressing by repressing

Some industries have developed processes where a compaction of powder followed by a granulation is necessary. So such automatic systems are already developed [153]. The products are generally made by first compacting the original material then crushing and screening it to recover the fraction having the desired mesh size. For example, fertilizers are compacted and granulated to prevent them from caking in bags or containers. Many pharmaceutical products, such as aspirin and antibiotics, are compacted in roll type machines and then granulated to produce free flowing, granular material from which tablets are made.

This technology may be adapted in our system which requires this type of method.

10.2.4. Nanoscopic homogeneity

The inhomogeneity of fuel at the nanocopic scale may be releveant on a concentration profile of Pu and or MA. However, for the transmutation point of view, these concentrations will cause locally higher burn up and so fission and activation products release that may be problematic for the fuel [154]. The need of homogeneity of the fuel at the microscopic scale has so to be considered.

Conradson et al. [155] performed XAFS experiments of Er-Y-(U-Ce)-Zr oxides prepared by co-precipitation of nitrate solution by ammonia. In this work also ceria was used as substituted of plutonium. The authors demonstrated that some of the metals ions are not randomly, isomorphically substituted into the lattice but instead have tendencies to form nanometer-scale clusters and networks.

Similar results may be expected in the industrial case of our produced $(Zr,Y,Ce)O_{2-x}$ fuel.

10.2.5. Elimination of dust formation

After sintering, it is necessary to sort the pellets function of their properties and to polish the selected one [10], whatever the synthesis route is, sol-gel or co-precipitation or dried milling. The problem of dust formation remains. As in the case for the actual MOX-fabrication, the polishing will cause dust formation, that should be treated and the non suitable pellets have to be entsorgt. This problem should be taken into consideration in a pellet production cycle.

The elimination of the dust problem in a ceramic cycle may be possible by avoiding the pelletization step. In fact, by using a sol-gel method, micro-spheres can be produced and can be used as particles fuel, as in the coated particles HTR-fuel. This idea of "Sphere-pack" has been demonstrated as valid in the case of High Temperatures Reactors fuel system.

This principle can be also adapted to a conditioning system. The principle of a multi-barrier coating can be also applied to these micro-spheres.

10.2.6. Appreciation on the co-precipitation method

The main advantage of the co-precipitation method are its simplicity, efficiency and the homogeneity of the final material.

However, the co-precipitation is responsible of agglomerates formation which limit the sintering ability of the material and so the properties of final compounds.

However, if agglomeration is a drawback for a pelletization, it can be turned at its advantage in a frame of a VIPACK technology. In fact, instead of producing microspheres, large particles can be also used as fuel and packed by a vibration process. After precipitation and drying, the powders consist in larges agglomerates, that can be sintered and maybe used as fuel directly without pelletization.

11. Acknowledgements

This work was published in the following journals

1- A.A. Bukaemskiy, D. Barrier and G. Modolo, Physical properties of 8 mol% Ceria doped yttria stabilised zirconia powder and ceramic and their behaviour during annealing and sintering , In Press, Corrected Proof, accepted the 4th February 2005, available online 16 March 2005, Journal of the European Ceramic Society

2- D. Barrier, A.A. Bukaemskiy, and G. Modolo, Thoria, Inert matrix for the immobilization of Plutonium - Proceeding of EMRS Spring meeting 2005, to be published in Journal of Nuclear Materials

3- D. Barrier, G. Modolo and A.A. Bukaemskiy, Influence of ceria addition on the thermal and crystallisation behaviour of yttrium-stabilised zirconia. Submitted to Thermochimica acta

This work was presented in the following conferences

1- ICEM 03: Oral presentation and article
D. Barrier, A.A. Bukaemskiy, K.S. Soe, M.M. Titov, G. Modolo, Fixation of actinides in Zirconium based ceramics, Proceedings of the 9th International Conference on Radioactive Waste Management and Environmental Remediation September 21 - 25, 2003, Examination School, Oxford, England

2- International Workshop on P&T and ADS Development 2003: Poster and article
D. Barrier, A.A. Bukaemskiy, K.S. Soe, G. Modolo, Yttrium Stabilised Zirconium Ceramic as host phase for actinide immobilisation, Proc. of the International Workshop on P&T and ADS Development 2003 (October 6-8 2003) Mol, Belgium

3- <u>Jahresstagung Kerntechnik 2004</u>: Oral presentation and compact

D. Barrier, A.A. Bukaemskiy, G. Modolo, R. Odoj, Immobilisation of actinides in ceramics for transmutation, Jahresstagung Kerntechnik 2004- 25-27 Mai 2004 - CDD Stadthalle Düsseldorf - Kerntechnische Gesellschaft e.V. - Deutsches Atomforum e.V.

4- <u>NRC6</u>: Poster and compact

D. Barrier, A. A. Bukaemskiy, G. Modolo, R. Odoj, Fabrication and characterization of inert matrix and thoria fuel for actinides transmutation, Extended Abstracts of Paper presented at the Sixth International Conference on Nuclear and radiochemistry (NRC-6), 29 August to 3 September 2004, Aachen, Germany.

5- <u>HGF Doktorantenseminar 2005</u>: Oral presentation and compact

D. Barrier, Fabrication of ceramics targets containing actinides for transmuation, Proceeding of the first HGF Doktoranten seminar, Forschungszentrum Karlsruhe GmbH - FTU, 09-11 März 2005, Karlsruhe, Germany.

6- <u>Symposium N ERMS Spring meeting 2005</u>: Oral presentation and article

D. Barrier, A.A. Bukaemskiy, G. Modolo, Thoria, Inert matrix for the immobilization of Plutonium, Symposium N (Nuclear Material) of the European Materials Research Society (ERMS) Spring meeting, Strasbourg, France, 31 May - 03 June, 2005

7- <u>ICEM 05</u>: Oral presentation and article

D. Barrier, A.A. Bukaemskiy, G. Modolo, Immobilisation of Plutonium in Thoria based ceramics, Proceeding of the 10th International Conference on Environmental Remediation and Radioactive Waste Management September 4 - 8, 2005, Scottish Exhibition & Conference Centre, Glasgow, Scotland

8- <u>Gesellschaft Deutscher Chemiker eV (GDCh) - Jahrestagung 2005</u>: Oral presentation

D. Barrier, A.A. Bukaemskiy, G. Modolo, R. Odoj, Yttrium stabilized Zirconia and Thoria: Inert Matrix for the immobilisation of actinides. GDCh-Jahrestagung 2005, Düsseldorf, 11 - 14 September 2005

12. References

1   World Nuclear association - Information and issues briefs – Sustainable energy –2005, www.world-nuclear.org

2   World Nuclear association - Information and issues briefs –Nuclear Power in the World Today – 2005, www.world-nuclear.org

3   Lefevre, J., Energie nucleaire, Cycle du combustible nucléaire, Les déchets radioactifs, ENSCP, 2001, personnal communication

4   Uranium information center, Melbourne, Australia, www.uic.com.au

5   World Nuclear association - Information and issues briefs –Nuclear Power Reactor – 2004, www.world-nuclear.org/

6   www.nucleartourist.com/type/pwr.htm

7   Morvan, P., Nucléaire, Les chemins de l'uranium,Paris, ellipses, 2004

8   Gras, J.M., EDF R&D, Confinement des déchets radioactifs, ENSCP, 2001, personnal communication

9   Vergnes, J., Mouney, H., Le devenir des déchets nucléaires : une voie de recherche l'incinération-transmutation, Proc of the « Energie et environnement », Semaine ParisTech, ENSTA, nov 2001.

10   Areva-Melox, le combustible MOX – L'usine MELOX- documentation

11   Edwards, J, Chilton, G.R., Stanbridge, J.R., Baxter, W., The conversion of plutonium into thermal reactor MOX fuel in the UK, Proc 3rd Int. Conf. Nuclear Fuel reprocessing and Waste management, RECORD'91, Sendai, Japan, Apr 1991, volI, 207-212

12   Vernaz, E., Glass packaged guaranted for millions years, les clefs du CEA, n°46, 2001, 81-84

13   Phlippen, P.-W., Reduction Requirements for Actinides with Special Regard to the Isolation Time at Final Disposal, Proc. Technical Committee Meeting on Advanced Fuels with Reduced Actinide Generation, Vienna, Nov. 21-23, 1995, IAEA-TECDOC-916, Vienna 1996, 71-82

14   Modolo, G., Odoj, R., Actinide separation, a contribution to safe disposal, Proc. of the DisTec 2000 International Conference on Radioactive Waste Disposal, Berlin, Germany, September 4-6, 2000, 520-525

15   Phlippen, P.-W., Lypsch, F., Lizana, P., Rütten, H.-J., Gefährdungspotential radioaktiver Abfälle. Auswirkungen der Entwicklung der ICRP-Richtlinien auf die Bewertung, atomwirtschaft 40, 1995,6, 384-389

16   IAEA-TECDOC, Implications of partitioning and transmutation in radioactive waste management, 2001

17   Madic,C., Testard, F., Hudson, M.J., Liljenzin, J.-O, Christuansen, B., Ferrando, M., Facchini, A., Geist, A., Modolo, G., Gonzales.Espartero, A., De Mendoza, J., Partnew New solvent extraction processes for minor actinides, Final report, CEA, June 2004, 82-89

18   Nuclear Energy agency – Organisation for Econimic Co-operation and Development, Actinide and Fission product Partitioning and Transmutation, OECD, 1999

19   Salvatores, M., La transmutation, ENSCP, 2001, personnal communication

20   Nuclear Energy agency – Organisation for Econimic Co-operation and Development, Accelerator-driven Systems (ADS) and Fast Reactors (FR) in Advanced Nuclear Fuel cycles, OECD, 2002

21   Akie, H., Muromura, T., Takano, H., Matsuura, A new fuel material for once-through weapons plutonium burning, S. Nucl. Technol. 107 (1994) 182.

22   C. Degueldre, U. Kasemeyer, F. Botta, G. Ledergerber, Plutonium incineration in LWRs by a once through cycle with a rock-like fuel, Mater. Res. Soc. Proc., 412 (15), 1996

23   Burghartz, M., Matzke, H., Léger, C., Vambenepe, G., Rome., M., Inert matrices for the transmutation of actinides: fabrication, thermal properties and radiation stability of ceramic materials J. Alloys Compounds 271–273 (1998), 544

24   Porta, J., Baldi, S., Guigon, B., Some neutronic properties of inert matrix in order to define a 100% IMF core, Proceedings of the ARWIF'98, OECD-NEA workshop, PSI-Villigen, October 1998

25   Degueldre, C., Paratte, J.M., Concepts for an inert matrix fuel, an overview, J. Nucl. Mat., 274 (1999) 1-6

26   Schram, R. P. C., Kuijper, J. C., Sommer, D., Somers, J., Phlippen, P., Bodewig, T., Worral, A., Struzik, C., Raison, Ph., The thorium cycle, Proc. of the International Workshop on P&T and ADS Development 2003 (October 6-8, 2003) Mol, Belgium

27   Lombardi, C., Mazzola, A., Padovani, E., Ricotti, M.E., Neutronic analysis of U-free inert matrix and thoria fuels for plutonium disposition in pressurised water reactors, J. Nucl. Mat. 274 (1999) 181-188

28   Lombardi, C., Luzzi, L., Padovani, E., Vettraino, F., Progress in Nuclear Energy, Vol. 38, No 3-4, (2001) 395-398

29   Pereira, C., Leite, E.M., Non-proliferating reprocessed nuclear fuels in pressurised water reactors:fuel cycle options, Ann. Nucl. En., 25-12 (1998) 937-962

30   Rütten, H.J., Haas, K.A., Research on the incineration of plutonum in a modular HTR using thorium-based fuel, Nucl. Eng. and Des., 195 (2000) 353-360

31   Vapirev, E.I., Dimitrov, V.I., Jordanov, T.J., Christoskov, I.D., Conversion of high enriched uranium in thorium-232-based oxide fuel for light and heavy water reactors: MOX-T fuel, Nucl. Eng. and Des., 167 (1996) 105-112

32   Pereira, C., Leite, E.M., Non-proliferating reprocessed nuclear fuels in pressurisd water reactors:fuel cycle options, Ann. Nucl. En., 25-12 (1998) 937-962

33   Galperin, A., Utilization of light water reactors for plutonium incineration, Ann. Nucl. En., 22-8 (1995) 507-511

34   Kugeler, K., Phlippen, P.W., Odoj, R., Rütten, H.J., Neuhaus,I., Stand und zeitlicher Horizont verschiedener Transmutationsverfahren, Proc of Optionen bei der Verwertung und Entsorgung von Plutonium, Juelich, Germany, Januar 13-14, 2000.

35   Pillon, S., Somers, J., Grandjean, S., Lacquement, J., Aspects of fabrication of curium-based fuels and targets, J. Nucl. Mater. 320 (2003) 36-43

36   Konings, R. J. M., Advanced fuel cycles for accelerator-driven systems: fuel fabrication and reprocessing, EU report 19928, (2001)

37   Lutze, W., Ewing, R.C., (Eds.), Radioactive Waste Forms for the future, North-Holland, New York, 1988

38   Caurant, D., Verres et nouvelles matrices de confinement des déchets nucléaires de haute activité, ENSCP, 2001, personnal communication

39   Matzke, H., Rondinella, V. V. and Wiss, T., Materials research on inert matrices: a screening study. J. Nucl. Mater., 274 (1999) 47-53.

40   Pillon, S., Status of the European FUTURE programme, Proc. of the International Workshop on P&T and ADS Development 2003 (October 6-8, 2003) Mol, Belgium

41   Ledergerber, G., Degueldre, C., Heimgartner, P., Pouchon, M. A. and Kasemeyer, U., Inert matrix for the utilisation of plutonium. Progress in Nuclear Energy, 38 (3-4) (2001) 301-308.

42   Sickafus, K. E., Matzke, H., Hartmann, H., Yasuda, K., Valdez, J. A., Chodak III, P., Nastasi, M. and Verrall, R. A., Radiation damage effects in zirconia. J. Nucl. Mater., 274 (1999) 66-77

43   Gong, W. L., Lutze, W. and Ewing, R. C., Zirconia ceramics for excess weapons plutonium waste. J. Nucl. Mater., 227 (2000) 239-249.

44   Pouchon, M.A., Döbeli, M., Delgueldre, C., Burghartz, M., Behavior of cesium implanted in zirconia based inert matrix fuel, J. Nucl. Mat. 274 (1999) 61-65

45   Delgueldre, C., Pouchon, M.A., Döbeli, M., Sickafus, K., Hojou, K., Ledergerber, G., Abolhassani-Dadras, S., Behaviour of implanted xenon in yttria stabilised zirconia as inert matrix of nuclear fuel, J. Nucl. Mat. 289 (2001) 115-121

46   Piconi, C., Maccauro, G., Review – Zirconia as a ceramic biomaterial, Biomater., 20 (1999) 1-5

47   Pouchon, M.A., Contribution to the study of a zirconia based nuclear fuel for plutonium use in light water reactor. PhD thesis University of Geneva (2000)

48   Pouchon, M.A., Nakamura, M., Hellwig, Ch., ingold, F., Delguedre, C., Cermet sphere-pac concept for inert matrix fuel, J. Nucl. Mat. 319 (2003) 37-43

49   Ledergerber, G., Ingold, F., Stratton, R.W., Prunier, C., Warin, D., Bauer, M., Preparation of transuranium fuel and target materials for the transmutation of actinides by gel coconversion, Nucl. Tech. 114 (1996) 194-204

50   Lee, Y. W., Kim, H. S., Kim, S. H., Joung, C. Y., Na, S. H., Ledergerber. G., Heimgartner, P., Pouchon, M., Burghartz, M., Preparation of simulated inert matrix fuel with different powders by dry milling method, J. Nucl. Mat., 274 (1999) 7-14

51   Richter, K., Fernandez, A., Somers, J., Infiltration of highly radioactive materials: a novel approach to the fabrication of targets for the transmutation and incineration of actinides, J. Nucl. Mat., 249 (1997) 121-127

52   Haas, D., Somers, J., Charollais, F., Innovative fabrication of fuels and targets for Pu recycling and minor actinide transmutation, ATW-INT Z Kernenrg. 44-12 (1999) 709-714

53   Maschio, S., Bacchiorrini, A., Lucchini, E., Sintering behaviour of mechanically alloyed and coprecipitated 12Ce-PSZ powders. J. Mater. Sci., 1998, 33, 3437-3441.

54   Van de Graaf, M.A.C.G., Keizer, K., Burggraaf, J. A., Influence of agglomerate structures in ultra-fine sunstituted zirconia powders on compaction and sintering behaviour. Sci. Ceram., 10 (1979) , 83-92.

55   Fernandez, A., Richter, K., Somers, J., Fabrication of transmutation and incineration targets by infiltration of porous pellets by radioactive solutions, J. Alloys Comp. 271 (1998) 616-619

56   Fernandez, A., Haas, D., Konings R.J.M., Somers, J., Fuel/target concepts for transmutation of actinides, In Proceedings of the NEA P&T Exchange Meeting 2000, Madrid, 2000.

57   Boucharat, N., Fernandez, A., Somers, J., Konings, R. J. M., Haas. D., Fabrication of zirconia-based targets for transmutation. Progress in Nuclear Energy, 38 (3-4) (2001) 255-258.

58   Fernandez, A., Haas, D., Konings, R.J.M., Somers, J., Transmutation of actinides, J.Am.Cer.Soc., 85(3) (2002) 694-696

59   Pinheiro, R.B., Lameiras, F.S., Peehs, M., Maly, V., Thorium utilisation in PWRs, Final Report (1979-1988), KFA Jül-Spez 488, (1988) 149-152

60   Brambilla, G., Gerontopulos,P., Neri,D., The SNAM process for the preparation of ceramic nuclear fuel microspheres: laboratory studies, En. Nucl. 17 (1970) 217-225

61   Chandramouli, V., Anthonysamy, S., Vasudeva Rao, P. R., Divakar, R., Sundararaman, D., PVA aided microwave synthesis: A novel route for the production of nanocrystalline thoria powder J. Nucl. Mat. 231 (1996) 213-220

62   Hubert, S., Barthelet, K., Fourest, B., Lagarde, G., Dacheux, N., Baglan, N., Influence of the precursor and the calcination temperature on the dissolution of thorium dioxide, J. Nucl. Mat. 297 (2001) 206-213

63   Kutty, T. R. G., Hegde, P. V., Banerjee, J., Khan, K. B., Sengupta, A. K., Jain, G. C., Majumdar, S. and Kamath, H. S., Densification behaviour of ThO_2-PuO_2 pellets with varying PuO_2 content using dilatometry , J. Nucl. Mat. 312 (2003) 224-235

64   Basak, U., Sengupta, A.K., Ganguly, C., Hot hardness and thermal conductivity of ThO_2-PuO_2 and ThO_2-UO_2 sintered pellets, J. Mat. Sci. Let. 8(4) (1989) 449-450

65   Taylor, P., Hocking, W.H., Johnson, L.H., McEachern, R.J., Sunder, S., A comparison of $(Th,Pu)O_2$ and UO_2 fuels as waste forms for direct disposal, Nucl. Tech. 116 (1996) 222-230

66   Fernandez A, Konings RJM, Somers J, Haas, D., Fabrication of CERamic-CERamic composites pellets for the transmutation of actinides, J. Mater. Sci. Letters 22 (2003) 119-121

67   Fernandez A, Konings RJM, Somers J, Design and fabrication of specific ceramic-metallic fuels and targets», J. Nucl. Mat. 319 (2003) 44-50.

68   Kuramoto, K., Mitamura, H., Banba, T. and Muraoka, S., Development of ceramic waste forms for actinide-rich waste. Progress in Nuclear Energy, 32 (3-4) (1998) 509-516.

69   Baes, C.F., Mesmer, R.E., The hydrolysis of cations, Wiley-Interscience, New-York, 1976, 129.

70   Ahniyaz A., Fujiwara, T., Fujino, T., Yoshimura, M., Low-Temperature direct synthesis of CeO_2-ZrO_2 Solid solution Nanoparticles by a hydrothermal method, J. Nanosci. Nanotech. 4 (2004) 233-238

71   Cholure d'ammonium, Fiche de données de sécurité PROLABO selon la Directive Européenne 91/155/CEE - www.ac-nancy-metz.fr/enseign/physique

72   Nitrate d'ammonium, Fiche de données de sécurité PROLABO selon la Directive Européenne 91/155/CEE - www.ac-nancy-metz.fr/enseign/physique

73   Brusset, I., Leveau, F., Spinat, P., Trani, A., Verollet, J., Le nitrate d'ammonium, Description, production, utilisations et précautions d'usage, Institut National Polytechnique de Toulouse, 2002

74   Dr. A.A. Bukaemskiy, private communication

75   Kouzov, P.A., Basis for analysis of industrial dust and ground materials dispersion, Khimia, Leningrad, 1974, 280.

76   www.ac-nancy-metz.fr/enseign/physique/chim/FDS/

77   Winston, C., Analytical chemistry by open learning: X-Ray methods. Wiley, New York 1985, 131-135

78   Winston, C., analytical chemistry by open learning: X-Ray methods. Wiley, New York 1985, 365

79   Winterer, M., Nanocrystalline Ceramics: Synthesis and Structure, Springer, 2002, 21-23.

80   Williamson, G. K., Hall, W. H., X-ray line broadening field aluminium and wolfram. Acta Metallurgica, 1 (1953) 22-31.

81   Klug, H. P., Alexander, L.E., X-ray diffraction procedures for polycrystalline and amorphous materials. Wiley, New York, 1954.

82   Yahiro, H. , Egushi K., Arai, H., Electrical properties and reducibilities of ceria-rare earth oxide systems and their application to solid oxide fuel cell, Solid state Ionics, 36 (1989) 71-75

83   Kutty, T. R. G., Hedge, P. V., Khan, K. B., Basak, U., Pillai, S. N., Sengupta, A. K., Jain, G. C., Majumdar, S., Kamath & H. S., Purushotham, D. S. C., Densification behaviour of UO_2 in six different atmospheres. J. Nucl. Mater., 305 (2002) 159-168.

84   Munz, T.Fett, Ceramics: mechanical properties, failure bahaviour, materials selection, Springer, Berlin Heidelberg, 1999, 31-37

85   Rice R. W., Porosity of Ceramics, Marcel Dekker, Inc., Berlin Heidelberg, 1998, 276-314

86   Ingel, R.P., Lewis, D., Bender, B.A., Rice, R.W., Physical, microstructural and thermomechanical properties of ZrO_2 Single crystals, Advances in ceramics 12 (1984) 408-414

87   Molycorp, Inc., Cerium, a guide to its role in chemical technology, Moutain Pass CA USA, 1992, 12.

88   Belle, J., Berman, R.M., Thorium dioxide: Properties and Nuclear applications, Government Printing Office, Washington, D.C., 1984, 320

89   Tadokoro, S.K., Mucillo, E.N.S., Physical characteristics and sintering behaviour of ultrafine zirconia-ceria powders, J. Eur. Cer. Soc. 22 (2002) 1723-1728

90   Li, Y.X., Zhou, X.Z., Wang, Y., You, X.Z., Preparation of nano-sized CeO_2 by mechanochemical reaction of cerium carbonate with sodium hydroxide, Materials letters 58 (2003) 245-248

91   Bjerrrum, Schwarzenbach, Sillen, Stability Constants of Metal Complexes, Part II, Chemical Society, London 1958

92   Aronne, A., Marotta, A., Pernice, P. & Catauro, M., Sol-gel processing and crystallisation of yttria-doped zirconia, Thermochimica acta, 275 (1996) 75-82

93   Rutman, D.S., Toropov, Yu.S., Pliner, S.Yu et al., Refractory material from zirconium dioxide, M.: Metallurgy, 1985, 137

94   Ingo, G. M., Righini, G., Scoppio, L., Chemical aspects in thermal treatment of ZrO_2-CeO_2-Y_2O_3 alloy, Applied Surface Science, 55-4 (1992) 257-267.

95   Andrevskaya, E.R., Red'ko, V.P., Lopato, L.M. Interaction of cerium oxide with hafnium, zirconium, and yttrium oxides at 1500°C. Powder Metallurgy and metal ceramics, 40(7-8) (2001) 405-413.

96   Hinatsu, Y., Muromura, T., Phase relations in the systems ZrO_2-Y_2O_3-Nd_2O_3 and ZrO_2-Y_2O_3-CeO_2. Mat. Res. Bull., 21 (1986) 1343-1349

97   Kinoshita, H., Kuramoto, K., Mazayoshi, U., Yanagi, T., Yamanaka, S., Mitamura, H. & Banba, T., Phase stability of Yttria-Stabilized Zirconia with Dissolved Cerium and Neptunium Oxides Under Oxidizing and Reducing Atmorspheres. J. Am. Ceram. Soc., 83-2 (2000) 391-96.

98   JCPDS, International Centre for Diffraction Date, 30-1468.

99   JCPDS, International Centre for Diffraction Date, 34-0394.

100   Yamishita, T., Kuramoto, K., Nakada, M., Yamazaki, S., Sato, T., Matsui, T., Phase relations between a fluorite and a pyrochlore structure in the system of actinides and zirconium oxides, J. Nucl. Sci. Tech., 3 (2002) 585-591

101   Burghartz, M., Ledergerber, G., Ingold, F., Heimgartner, P., Delguedre, C., X-ray diffraction analysis and data interpretation of stabilized zirconia iner matrix fuel doped with plutonium, Progress in Nuclear Energy, 38 (3-4) 2001 247-250

102   Dzisko, V.A., Basis of catalysts preparation methods, Nauka, Novosiborsk, 1983, 263.

103   Dodd, A.C. & McCornick, P.G., Synthesis and processing of Ultrafine Mg-PSZ Powder, Journal of Metastable and Nanocrystalline Materials, 312-314 (1999) 221-226.

104   Lange, F.F., Sinterability of agglomerated powders, J. Am. Cer. Soc., 67 (1984) 83-89

105   Tadokoro, S.K., Muccillo, E.N.S., Physical characteristics and sintering behaviour of ultrafine zirconia-ceria powders, J. Eur. Cer. Soc. 22 (2002) 1723-1728

106   Van de Graaf, M.A.C.G., Ter Maat, J.H.H., Burggraaf, A., J. Mater. Sci., 20 (1985) 1407-1414

107   Groot Zevert, W.F.M., Winnubst, A.J.A., Theunissen, A.J.A., Burggraaf, A.J., Powder preparation and compaction behaviour of fine-grained Y-TZP, J. Mat. Sci, 25 (1990) 3449-3455.

108   Lin, J.D., Duh, J.G., Chiou, B.S., The influence of washing and calcination condition on urea-derived ceria-yttria-doped tetragonal zirconia powders, Mater. Chem. Phys. 68 (2001) 42-55

109   Dynys, F. W. & Halloran, J. W., Influence of Aggregates on Sintering, J. Am. Cer. Soc., 67-9 (1984) 596-601.

110   Shi, J.L., Gao, J.H., Yen, T.S., Sintering behaviour of fully agglomerated zirconia compacts, J. Am. Cer. Soc., 74 (1991) 994-997

111   Evans, A. G., Considerations of Inhomogeneity Effects in Sintering, J. Am. Cer. Soc., 61(1-2) (1978) 1-5.

112   Shi, J.L., Gao, Z.X., Lin, Z.X., Yan, D.S., Effects of agglomerates in ZrO_2 powder compacts on microstructural development, J. Mater. Sci. 28 (1993) 342-348

113   Gao, L., Li, W., Wang, H. Z., Zhou, J. X., Chao, Z. J. and Zai, Q. Z., Fabrication of nano Y-TZP materials by superhigh pressure compaction. J. Eur. Ceram. Soc., 21 (2001) 135-138.

114   Ferkel, H. and Hellmig, R. J., Effect of nanopowder deagglomeration on the densities of nanocrystalline ceramic green bodies and their sintering behaviour. NanoStructured Mat., 11 (5) (1999) 617-622.

115   Abraham, I., Gritzner, G., Powder Preparation, Mechanical and Electrical Properties of Cubic Zirconia Ceramics, J. Eur. Cer. Soc. 16 (1996) 71-77.

116   Maschio, S., Sbaizero, O., Meriani, S., Mechanical properties in the Ceria-Zirconia System, J. Eur. Cer. Soc., 9 (1992) 127-132

117   Furukawa, M., Horita, Z., Nemoto, M., Valiev, R.Z., Langdon, T.G., Microhardness measurements and the Hall-Petch relationship in an Al-Mg alloy with submicrometer grain size, Acta. Mater., 44 (1996) 4616-4629

118   Volpp, T., Göring, E., Kuschke, W.M., Arzt, E., Grain size determination and limits to Hall-Petch behavior in nanocrystalline NiAl powders, Nanostructured Materials, 8 (1997) 855-865

119   Barrier, D., Bukaemskiy, A. A., Soe, K. S. & Modolo, G., Yttrium stabilized zirconium ceramic as host phase for actinides immobilization. In Proceedings of Proceedings of the 9th International Conference on Radioactive Waste Management and Environmental Remediation 2003, Examination School, Oxford, England, SCK•CEN Club House, Belgium, 2003.

120   Lee, Y. W., Kim, H. S., Kim, S. H., Joung, C. Y., Lee, S. C., Na, S. H., Heimgartner, P. and Ledergerber. G., Measurement of the mechanical properties of thermally-shocked zirconia-based simulated inert matrix fuel. Progress in Nuclear Energy, 38 (3-4) (2001) 231-236.

121   Moorehead, D.R., McCartney, E.R., The formation of thoria by decomposition of nitrate, oxalate and hydroxide, J. Aus. Cer. Soc., 12 (1976) 27-33

122   Pepin, J.G., McCarthy, G.J., Phase relations in crystalline ceramic nuclear waste forms: The system UO_{2+x}-CeO_2-ZrO_2-ThO_2 at 1200°C in air, J. Am. Cer. Soc. 64-9 (1981) 511-516

123   Peterson, S., Curtis C.E., Thorium Ceramics Data Manual ORNL-4503, Vol.i (1970), 41

124   Tyagi, A.K., Ambekar, B.R., Mathews, M.D., J. Alloys and Compounds 337 (2002) 277-281

125   Gmelin Handbuch, Thorium, System-Nr 44, Ergänzungsband Teil C2 (1976) 78-81

126   Mulford, R.N.R., Ellinger, F.H., ThO_2-PuO_2 and CeO_2-PuO_2 solid solutions, J. Phys. Chem. , 62-11 (1958)-1466-1467

158

127   Freshley, M.D., Mattys, H.M., Irradiation of (Th,Pu)O$_2$, thorium fuel cycle, U.S. Atomic Energy Commission, Oak Ridge, Tenn., February 1968, 463-473

128   Pinheiro, R.B., Lameiras, F.S., Peehs, M., Maly, V., Thorium utilisation in PWRs, Final Report (1979-1988), KFA Jül-Spez 488, 1988, 152

129   Peterson, S., Curtis C.E., Thorium Ceramics Data Manual ORNL-4503, Vol.i (1970), 20

130   Basak, U., Sengupta, A.K., Ganguly, C., Hot hardness and thermal conductivity of ThO$_2$-PuO$_2$ and ThO$_2$-UO$_2$ sintered pellets, J. Mat. Sci. Let. 8(4) (1989) 449-450

131   Belle, J., Berman, R.M., Thorium dioxide: Properties and Nuclear applications, Government Printing Office, Washington, D.C., 1984, 344

132   Greenwood, N.N., Earnshaw, A., Chemistry of the elements, Pergamon Press Ltd., 1984, 1444

133   Catlow, C.R.A., Chadwick, A.V., Greaves, G.N., Moroney, L.M., EXAFS Study of Yttria-Stabilised Zirconia, J. Am. Cer. Soc. 69 (1986) 272-77

134   Dean, J.A., Lange's Handbook of Chemistry, 14th edition, McGraw-Hill, New-York, 1992, 4.13-4.17

135   Wang, J., Otobe, H., Nakamura, A., Takedo, M., Correlation of crystal structures with electric field gradients in the fluorite and pyrochlore-type compounds in the Gd$_2$O$_3$-ZrO$_2$ system, J. Sol. State. Chem. 176 (2003) 105-110

136   Ingel, R.P., Lewis III, D., Lattice parameter and density for Y$_2$O$_3$-Stabilized ZrO$_2$, J. Am. Cer. Soc., 6-4 (1986) 225-32

137   Pillon, S., Somers, J., Grandjean, S., Lacquement, J., Aspects of fabrication of curium-based fuels and targets, J. Nucl. Mater. 320 (2003) 36-43

138   Handbook of Chemistry and Physics, edn 74th. Edited by Lide DR. CRC; 1993, p.6-60

139   Handbook of Chemistry and Physics, edn 74th. Edited by Lide DR. CRC; 1993, p.6-95

140   www.geocities.com/CapeCanaveral/1475/fff.html

141   J. C. Giddings, M. N. Myers, M.H. Moon, B. N. Barman, ACS Symp. Ser., 472 (1991) 198

142   J.C. Giddings, F.J.F. Yang, M.N. Myers, Anal. Chem., 46 (1974) 1917

143   Muccillo, E.N.S., Avila, D.M., Synthesis and characterisation of submicron zirconia-12 mol% ceria ceramics, Cer. Int. 25 (1999) 345-351

144   Van de Graaf, M.A.C.G., Keizer, K., Burggraaf, A.J., Influence of agglomerate structures in ultra-fine substituted zirconia powders on compaction and sintering behaviour, Sci. Ceram., 10 (1979) 83-92

145   Shi, J.L., Gao, J.H., Yen, T.S., Sintering behaviour of fully agglomerated zirconia compacts, J. Am. Cer. Soc., 74 (1991) 994-997

146   Shi, J.L., Gao, Z.X., Lin, Z.X., Yan, D.S., Effects of agglomerates in ZrO_2 powder compacts on microstructural development, J. Mater. Sci. 28 (1993) 342-348

147   Hare'l, G., Ravi, B.G., Chaim, R., Effects of solvent and agitation on microstructural characteristics of sol-gel derived nanocrystalline Y-TZP powders, Mat. Lett. 39 (1999) 63-68

148   Avila, D.M., Muccilo, E.N.S., Effects of synthesis parameter on electrical conductivity and microstructural development on fine zirconia powders, J. Mater. Sci. Lett 16 (1997) 685-688

149   Qiu, H., Gao, L., Feng, C., Guo, J., Yan, D., Preparation and characterisation of nanoscale Y-TZP powder by heterogeneous azeotropic distillation, J. Mater. Sci., 30 (1995) 5508-5513

150   Shan, H., Zhang, Z., Preparation of nanometre-sized ZrO_2/Al_2O_3 Powders by heterogeneous azeotropique distillation, J. Eur. Cer. Soc. 17 (1997) 713-717

151   Okubo, T., Nagamoto, H., Low-temperature preparation of nanostructured zirconia and YSZ by sol-gel processing, J. Mater. Sci., 30 (1995) 749-757

152   Kalieszewki, M.S., Heurer, A.H., alcohol interaction with zirconia powders, J. Am. Cer. Soc., 73 (1990) 1504-1509

153   www.komarek.com/process

154   Taylor, P., Hocking, W.H., Johnson, L.H., McEachern, R.J., Sunder, S., A comparison of $(Th,Pu)O_2$ and UO_2 fuels as waste forms for direct disposal, Nucl. Tech. 116 (1996) 222-230

155   Conradson, S.D., Delguedre, C.A., Espinosa-Faller, F.J., Foltyn, S.R., Sickafus, K.E., Valdez, J.A., Villella, P.M., Complex behaviour in quaternary zirconias for inert matrix fuel: What do these materials look like at the nenometer scale ?, Prog. Nucl. En., 38-3-4 (2001) 221-230

156   Greenwood, N.N., Earnshaw, A., Chemistry of the elements, Pergamon Press Ltd., 1984, 1444

160

Figure and Table index

Curriculum Vitae

Diane BARRIER
Institut für Sicherheitsforschung und Reaktortechnik
Forschungszentrum Juelich GmbH
52425 Juelich
Germany
Tel : +49.2461.612752
Fax : +49.2461.612450
d.barrier@fz-juelich.de

Generalist chemist engineer graduated from ParisTech

EDUCATION

2002-2005	PhD Student at the **Rheinisch-Westfälische Technische Hochschule Aachen (RWTH-Aachen)** - Germany *"Doktor der Ingenieurwissenschaften" examination passed with distinction (Auszeichnung)*
1999 - 2002	Student at the **École Nationale Supérieure de Chimie de Paris (ENSCP)-ParisTech** - France *Master of science and chemical engineering degree (Engineer E.N.S.C.P.)*
1997 – 1999	**PCSI and PC*** at the Lycée Victor Hugo in Caen (Calvados) -France University-level preparation for the nation-wide competitive entrance exams to the "Grandes Écoles"
June 97	**Baccalauréat** (French secondary school examination), in sciences, with honours in Saint-Lô (Manche) - France

WORK EXPERIENCE

2002 – 2005	PhD work– **Forschungszentrum Juelich GmbH – Germany** *Characterisation and fabrication of zirconia and thoria based ceramics for nuclear applications*
2002 – 5 months	Diploma work – **Forschungszentrum Juelich GmbH – Germany** *Immobilisation of minor actinides in ceramics for a transmutation or a final disposal*
2001 – 3 months	Engineer internship – **Rhodia – Research centre in Aubervilliers (near Paris)-France** *Polymers adsorption on hydrophobic and low-energy surfaces (water-based painting for plastic)*
Summer 2000	Technician training period - **Laiteries (dairy) H. Triballat in Rians - France**

LANGUAGES

French: Mother tongue
German: Fluent
English: Fluent